Effects of High Magnetic Fields on a Charge-Density-Wave System

D. Andres

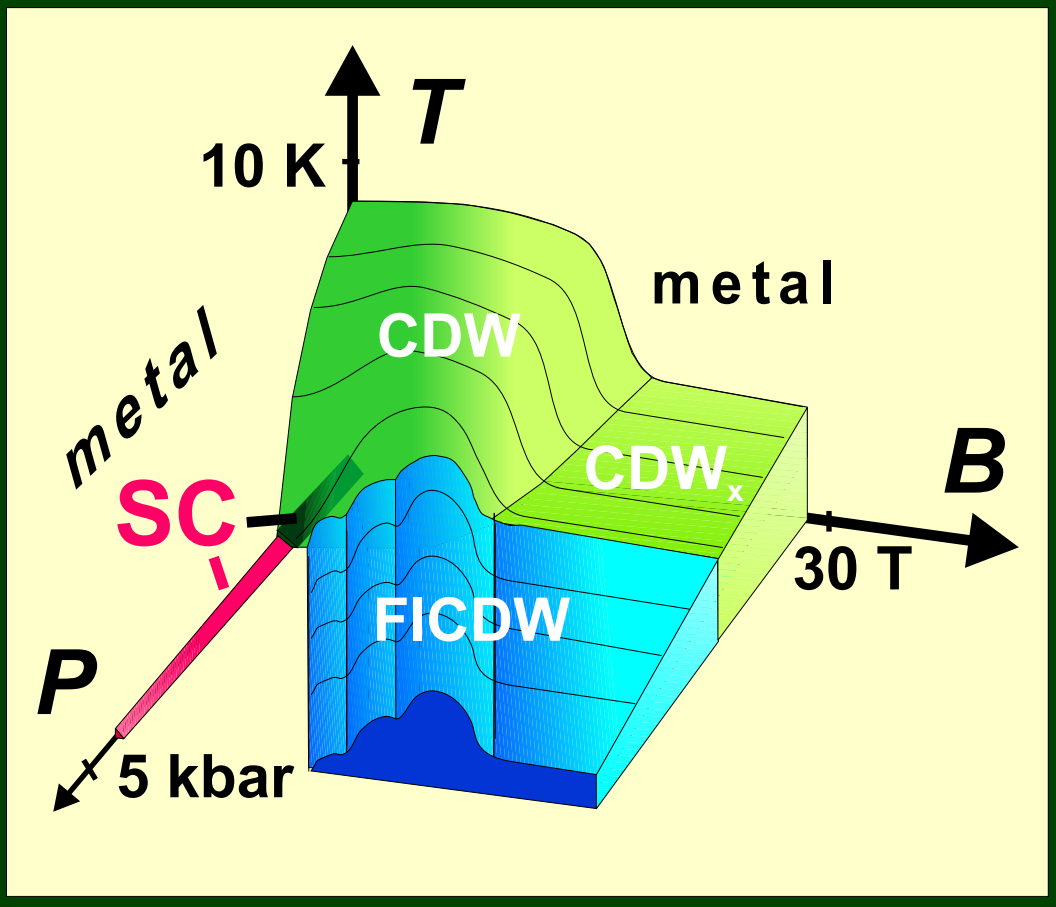

Lehrstuhl E23 für Technische Physik
Walther-Meißner-Institut für Tieftemperaturforschung
der Bayerischen Akademie der Wissenschaften

Effects of High Magnetic Fields and Hydrostatic Pressure on the Low-Temperature Density-Wave State of the Organic Metal α-(BEDT-TTF)$_2$KHg(SCN)$_4$

Dieter Andres

Vollständiger Abdruck der von der Fakultät für Physik der Technischen Universität München zur Erlangung des akademischen Grades eines

Doktors der Naturwissenschaften

genehmigten Dissertation.

Vorsitzender	Univ.-Prof. Dr. M. Kleber
Prüfer der Dissertation	
	1. Univ.-Prof. Dr. R. Gross
	2. Univ.-Prof. Dr. G. Abstreiter

Die Dissertation wurde am 25.11.2004 bei der Technischen Universität München eingereicht und durch die Fakultät für Physik am 20.04.2005 angenommen.

Contents

Chapter 1

Introduction

Over the last few decades the studies of crystalline conducting materials based on complex organic molecules have become a subject of intense interest in solid state physics. Initially, this interest was to a great extent driven by a theoretical work by Little published in 1964 [1]. He proposed conducting polymers, embedded in a highly polarizable medium, to provide a pairing mechanism for electrons, that may stabilize a superconducting state even above room temperature. Although this proposal up to now could not be realized, the synthesis of various organic charge transfer salts opened a door to a new fascinating field in solid state physics exhibiting manifold reasons for a broad interest [2].

Generally, the organic molecules arrange themselves in stacks, forming conducting layers which are separated by insulating, mostly inorganic counterion layers. In Fig. 1.1 examples of the most prominent organic molecules are depicted. Due to the charge transfer between these planes, a strong coupling is provided, resulting in stable crystalline materials. The layered character of the structure together with various kinds of arrangements of the molecules within the conducting planes give rise to very anisotropic, low-dimensional electron systems. This in turn causes a variety of interesting properties.

On the one hand, low dimensional conducting systems are known to be unstable with respect to the formation of various kinds of ordered ground states [2]. In the field of organic metals virtually all possible ground states of a conducting system, known up to date, were shown to exist. Moreover, it is known that, besides the strong dependence of the electronic states on slight changes of the chemical com-

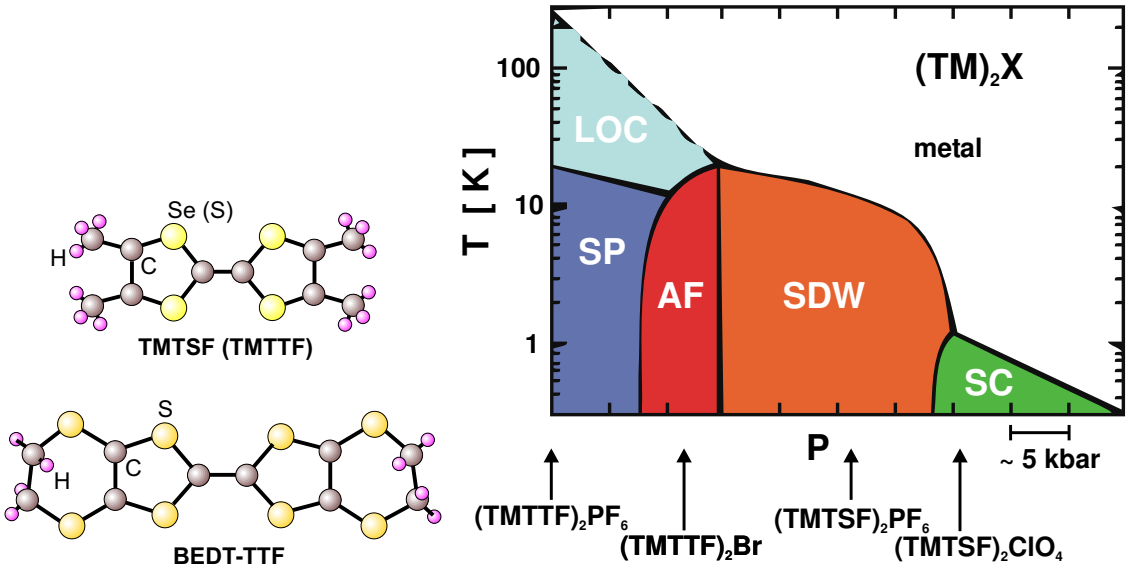

Figure 1.1: Left: Organic molecules, on which the most prominent organic metals are based: tetramethyl-tetraselenafulvalene (TMTSF),tetramethyl-tetrathiafulvalene (TMTTF) and bis(ethylenedithio)-tetrathiafulvalene (BEDT-TTF or ET). Right: Unified phase diagram of the organic compounds $(TMTTF)_2X$ and $(TMTSF)_2X$, where X stands for different anions. The arrows mark the ambient pressure positions of the compounds written below. A variety of ground states were shown to exist: charge ordered insulator (LOC), spin-Peierls-state (SP), antiferromagnetic insulator (AF), spin-density wave state (SDW), and a superconducting state (SC).(From [8], [4])

positions, phase transitions may be caused by the alteration of external parameters like temperature, magnetic field or a rather small pressure. A remarkable example of a pressure-temperature (P-T) phase diagram of some compounds based on the molecules TMTTF and TMTSF is depicted in Fig. 1.1. The application of hydrostatic pressure or the substitution of a different anion[1] is beautifully shown to create a variety of different ground states [3, 4]. These systems therefore offer an experimental and theoretical playground in studying already known as well as new phenomena in fundamental solid state physics. Among the latter there are, for instance, magnetic field-induced spin density wave (FISDW) transitions [5, 2] or, currently under investigation, magnetic field-induced superconductivity [6, 7].

Another remarkable property of these low dimensional systems is the fact that the Fermi surface in most cases turns out to be extremely simple [2, 9]. The latter often reveals itself by slightly warped open sheets and/or cylinders respectively

[1] since the substitution of different anions in many cases has been observed to be equivalent to applying pressure, the former is also often called "chemical pressure".

corresponding to a quasi-one-dimensional (Q1D) or a quasi-two-dimensional (Q2D) conductivity of the charge carriers. This, in most cases, offers an easy experimental access for studying the electronic properties. For example, the measurement of quantum oscillations has turned out to be an extremely powerful tool to determine the Fermi surface geometry [9]. On the other hand, this simplicity of the Fermi surface makes organic metals very nice model objects for theoretical investigations.

During the last decade the family of organic charge transfer salts α-(BEDT-TTF)$_2$MHg(SCN)$_4$ (M=K,Tl,Rb) attracted attention due to several low temperature anomalies found in magnetic field [10, 9]. While a density wave formation could be figured out to occur below $\approx$ 10 K [11], there has been a long debate about its real nature. No direct evidence for either a charge density or a spin density modulation could be found. A recently proposed B-T phase diagram [12], however, strongly favors a charge density wave (CDW) ground state in this organic system.

The most remarkable property of this CDW state would be the extremely low transition temperature and the correspondingly small energy gap. This allows available static magnetic fields to strongly influence the CDW or, in other words, to investigate the CDW state in an extremely wide range of its magnetic field-temperature (B-T) phase diagram. In particular, the first example of a modulated CDW-SDW hybrid state is most probably found to exist at low temperatures in magnetic fields above the paramagnetically limited "conventional" CDW state [12]. This state is an analogue to the theoretically proposed Fulde-Ferell-Larkin-Ovchinikov state predicted for low-dimensional superconductors [13, 14].

Besides this, measurements under hydrostatic pressure have shown that with application of only a few kbar the density wave state likely becomes suppressed [15,16]. Pressure, therefore, can be used as a parameter to alter the electronic properties of the system. Since these changes will very likely affect the density wave gap, one can expect strong changes in the magnetic field effects. In addition, the resulting modulation of the B-T phase diagram might further clarify the real nature of the density wave state. The starting point of the present work, therefore, was the investigation of the B-T phase diagrams at different hydrostatic pressures.

Within this work the electronic properties of the organic metal α-(BEDT-TTF)$_2$-KHg(SCN)$_4$ were studied by means of resistance measurements under hydrostatic pressure and additionally by combined resistance/magnetic-torque measurements at ambient pressure. High magnetic fields up to 17 T were provided at the Walther-Meissner-Institute and up to 30 T at the High Magnetic Field Laboratory in Greno-

ble.

The results have indeed given further strong arguments for a CDW to exist at low temperatures. It is shown that orbital effects appear in this low dimensional electron system in strong magnetic fields. These effects are for the first time observed in a CDW system and give rise to several new phenomena. In particular, a series of magnetic-field-induced CDW transitions has been observed for the first time.

Moreover, the presence of an additional, superconducting state under pressure is demonstrated within this system.

Chapter 2

Theoretical Background

In this chapter we give a short introduction into the physics which is necessary for the understanding of the present work. Since a complete theoretical description of the different topics is beyond the scope of this thesis, the physics will be explained in a rather qualitative manner.

2.1 Charge- and Spin-Density Waves (CDW, SDW)

2.1.1 Density Wave Instability in Low-Dimensional Electron Systems

A characteristic property of Q1D electron systems is their low-temperature instability against a formation of either a charge- or a spin-density wave (CDW, SDW) with a wave number $q = 2k_F$; where k_F is the Fermi wave vector. This will be shortly explained for the case of a CDW.

We assume a system of free (conduction) electrons to be exposed to an external time-independent potential:

$$V(\vec{r}) = \int V(\vec{q}) e^{i\vec{q}\vec{r}} d\vec{q}. \tag{2.1}$$

If this potential is not too strong, one can expect the change in the charge density $\delta\varphi(q)$ to be proportional to the amplitude $V(\vec{q})$:

$$\delta\varphi(\vec{q}) = \chi(\vec{q})V(\vec{q}). \tag{2.2}$$

Here, the response function $\chi(q)$, also known as the Lindhard function [17], can be derived from the perturbation theory [18] and, in d dimensions, is given by [19]:

$$\chi(\vec{q}) = \int \frac{d\vec{k}}{(2\pi)^d} \frac{f_k - f_{k+q}}{\epsilon_k - \epsilon_{k+q}}, \tag{2.3}$$

with $\epsilon_k = \epsilon(k)$ being the electron dispersion relation and $f_k = f(\epsilon_k)$ the Fermi-Dirac distribution function. For a one-dimensional (1D) electron system, with a linearized dispersion around the Fermi level, Eq. (2.3) at zero temperature can then be evaluated near $q = 2k_F$ as:

$$\chi(q) = \frac{-e^2}{\pi\hbar v_F} \ln\left|\frac{q+2k_F}{q-2k_F}\right| = -e^2 n(\epsilon_F) \ln\left|\frac{q+2k_F}{q-2k_F}\right|, \tag{2.4}$$

with e being the electron charge, v_F the Fermi velocity and $n(\epsilon_F)$ the carrier density at the Fermi level. Obviously the response of a 1D electron system to an external potential diverges on approaching the wave number $2k_F$. This, in turn, suggests by self-consistency that a 1D electron gas itself becomes unstable against the formation of a CDW with the wave number $2k_F$; i.e. the perturbation potential is effectively produced by the redistribution of the 1D carriers. This new periodic potential appearing in the system can be shown to create energy gaps exactly at $\pm k_F$ [19]. The energy of the electrons sitting near k_F therefore decreases and the 1D system eventually becomes insulating.

Looking back at Eq. (2.3) one understands the absence of such a divergence at $2k_F$ for a free electron gas in the two-dimensional (2D) and three-dimensional (3D) cases that is shown in Fig. 2.1 [20]. The divergence is caused by the presence of electrons and holes on opposite sides of the Fermi surface, separated in k-space by the same density wave vector. It now becomes evident that the response will only diverge if many electron-hole pairs may be created. The bigger the part of the Fermi surface is that "nests" another part by shifting it with the wave vector of the density wave, the stronger the response will be; and with it the energy gain of the system by forming a density wave. Therefore the density wave vector is often called *nesting vector* and we will adopt this designation below. On incorporating a finite temperature into Eq. (2.3) the response of the system will become weaker and a mean-field transition temperature, below which the density wave stabilizes,

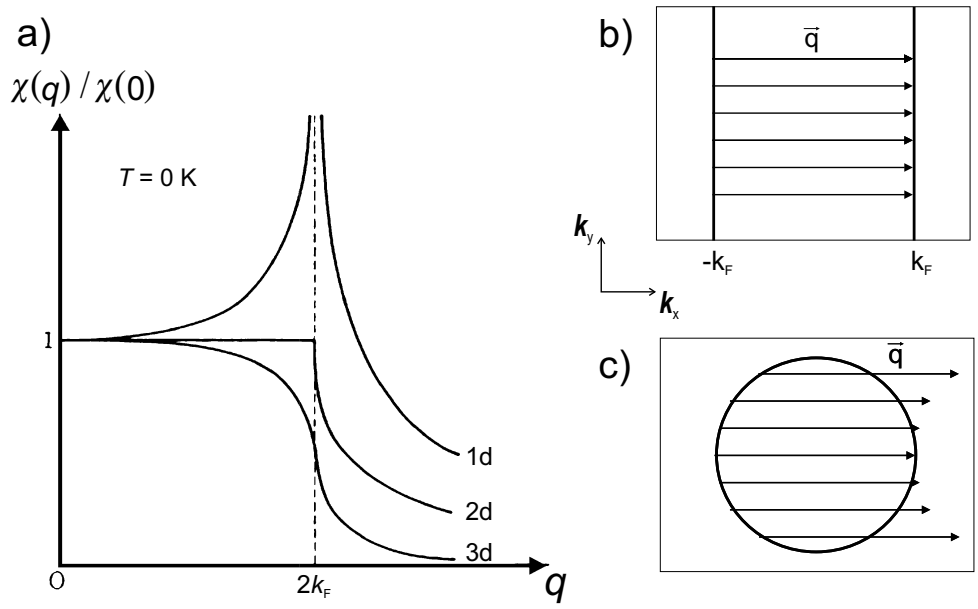

Figure 2.1: a) response function of a free electron gas in an external periodic field $V(\mathbf{q})$ for different dimensions. b) The Fermi surface of a 1D electron gas consists of sheets at $k_x = \pm k_F$ which can be perfectly nested on each other. c) In a 2D electron system the closed Fermi surface cannot be nested by a single wave vector. Only few electron-hole pairs can be created.

can be evaluated [19]. Additionally, since conduction electrons are coupled to the underlying lattice, a density modulation of the carriers causes a static modulation of the lattice that costs elastic energy and also has to be taken into account on evaluating the transition temperature [21].

Up to now, we have only dealt with a purely 1D electron system. As a matter of fact, due to the reduction in phase space, such an electron system is known to be unstable against fluctuations. The latter lead to the absence of any long range order at a finite temperature; for $T \neq 0$ K only short range correlations may develop [19]. One should, therefore, consider *quasi*-1D (Q1D) electron systems, in which the electrons have a finite probability to hop from one chain to the neighboring ones. In the tight-binding approximation, the dispersion relation for the electrons on conducting chains is determined by the energy transfer integrals along and perpendicular to the chains:

$$\epsilon(k) = -2t_{\parallel}\cos(k_{\parallel}a) - 2t_{\perp}\cos(k_{\perp}c) - \epsilon_F, \tag{2.5}$$

assuming the chains to run along the crystallographic **a** direction within a conducting **a-c** plane and ϵ_F being the Fermi energy. The consideration is restricted here to two

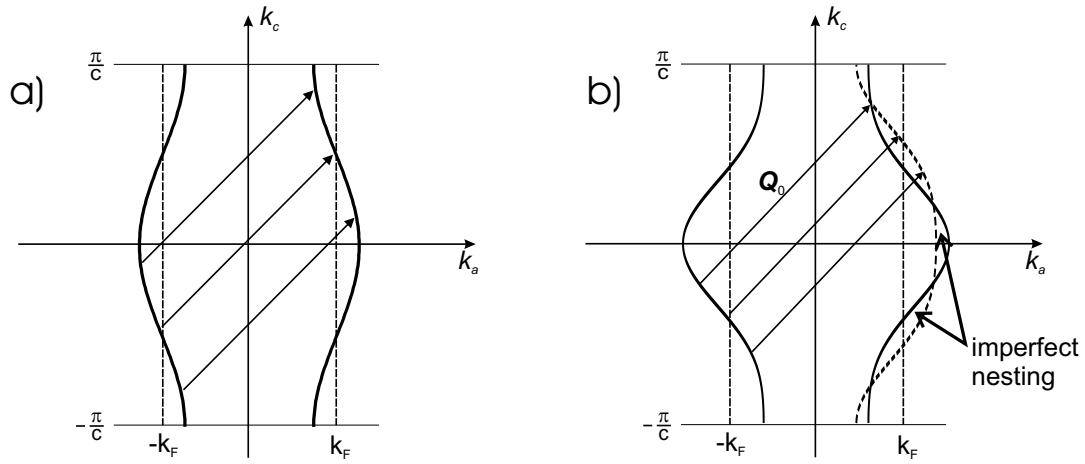

Figure 2.2: On incorporating a finite second order effective transfer integral in the linearized dispersion relation (2.6), the sheets of the Fermi surface change from perfect (a) to imperfect nesting conditions (b).

dimensions, assuming the dispersion in the third dimension to be negligibly small. For a strongly anisotropic electron system, i. e. $t_{\parallel} >> t_{\perp}$, the Fermi surface is in the first approximation defined by:

$$\epsilon_F(k) = \hbar v_F(\mid k_a \mid -k_F) - 2t_c \cos(k_c c). \tag{2.6}$$

This "Q1D" Fermi surface is plotted in Fig. 2.2a. The arrows indicate that these open sheets can also be perfectly nested on each other, however, with a nesting vector that is now tilted within the **a-c** plane and is given by:

$$\vec{Q} = 2k_F\vec{e}_a + \frac{\pi}{c}\vec{e}_c,^{1} \tag{2.7}$$

where $\vec{e}_{a,c}$ are the unit vectors. Q1D electron systems are thus still unstable against the formation of a density wave. Eq. (2.6) is, however, a strong simplification on describing real CDW compounds. On incorporating higher order terms of the interchain transfer the perfect nesting condition will actually not be fulfilled. This is sketched in Fig. 2.2b where a finite second order term has been added to the dispersion relation in Eq. (2.6):

$$\epsilon_F(k) = \hbar v_F(\mid k_a \mid -k_F) - 2t_c \cos(k_c c) - 2t'_c \cos(2k_c c) \tag{2.8}$$

As one sees in Fig. 2.2b the Fermi surface becomes more corrugated and the sheets can no longer be perfectly nested by a single wave vector. This means that for most

[1] correspondingly a weak dispersion perpendicular to the conducting plane (say **b**-direction) would add an additional term $(\pi/b)\vec{e}_b$

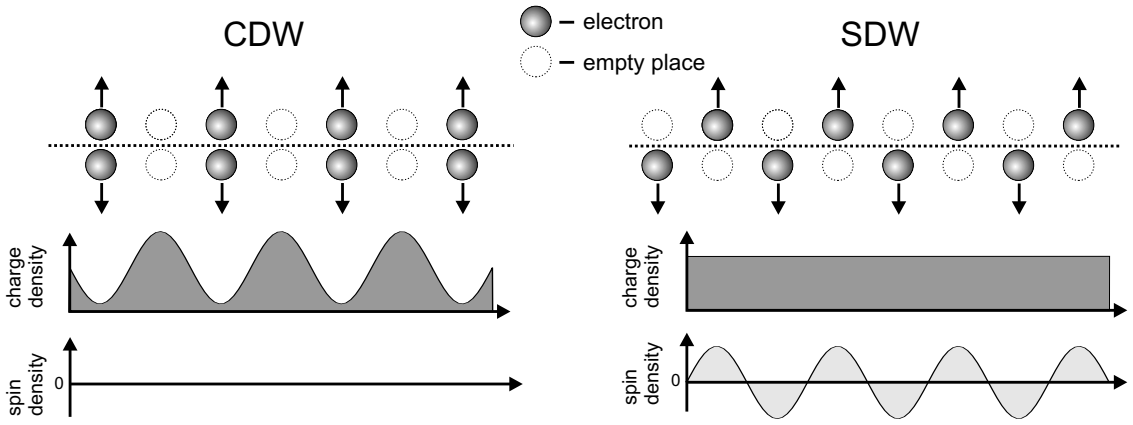

Figure 2.3: Qualitative arrangement of electrons in the CDW (left) and SDW states (right) in real space. Arrows show the direction of the spin. Below the resulting charge and spin density modulations are shown for both cases.

regions on the Fermi surface the nesting becomes "imperfect". The effective energy gap therefore decreases and so does the transition temperature T_c of the CDW state. The density wave is then completely suppressed, i.e. $T_c = 0$ K, as soon as free carriers appear on the Fermi surface [2]. To describe Q1D density wave systems most theoretical investigations therefore consider the energy dispersion near the Fermi level given by Eq. (2.8), where t'_c can be regarded as an effective next-nearest-neighbor transfer integral that introduces the imperfect nesting of the system.

2.1.2 Competition between Different Ground States

So far all considerations were made for a CDW system. Besides the charge, electrons also possess a magnetic spin. Similarly to the charge modulation it can be shown that by self-consistency the electrons may form a redistribution of the spin density, basically due to their Coulomb repulsion [19]. One may regard the spin modulation as a superposition of two CDWs, corresponding to different spin directions, which are in anti-phase with each other. As a result one obtains a spatially modulated spin density while the net charge density appears to be unaffected and remains constant in space. Fig. 2.3 sketches, in a simplified manner, the real space spin and charge density modulation for both SDW and CDW. A difference between the CDW and SDW states lies in the total spin of the electron-hole excitations causing

the diverging response.[2] In the former electrons and holes at $\pm k_F$ with opposite spin directions interact with one another whereas in the SDW they have the same spin direction [22]. As we shall see this has distinct consequences on applying an external magnetic field to both systems. Besides the possibility of electron-hole interaction (also known as Peierls channel) with excitations of finite momentum $2k_F$ there exists another competing mechanism of electron-electron pairing (the so-called Cooper channel) with the total momentum equal to zero. These can be either the superconducting singlet or triplet states. Which of these states eventually appears at low temperatures depends on the strengths of electron-phonon and electron-electron interactions. Theoretically this is considered in a strongly interacting electron gas model by comparing the response functions for the different states [23, 24]. We shall not go here into details of this so-called g-ology model. In a qualitative consideration one may say that [25]: if the electrostatic Coulomb repulsion dominates, there will be preferably a SDW or a superconducting (spin-triplet) state. If, however, the electrons mainly interact via phonons there will be an attracting force. In such a case either a CDW or a superconducting (spin-singlet) state will form.

2.1.3 Density Waves in an External Magnetic Field

The present work is mostly focused on the influence of a magnetic field on (Q1D) density wave systems. Here, we introduce the two basic effects, which are supposed to occur.

Pauli Paramagnetic Effect

The main difference between SDW and CDW systems lies in the total spin of the interacting electron-hole excitations. As one may immediately expect, an external magnetic field, acting on the spins of the carriers, can have drastic consequences on the stability of a density wave state. A simple consideration via the linearized 1D dispersion relation is sketched in Figs. 2.4 and 2.5. In a magnetic field the conduction band splits up into two sub-bands for electrons with opposite spins due to

[2] Note that density waves are actually not two-particle condensates. The annihilation of electrons at $-k_F$ and the creation of electrons at $+k_F$ and vice versa, leading to the diverging response function, are theoretically considered as electron-hole excitations.

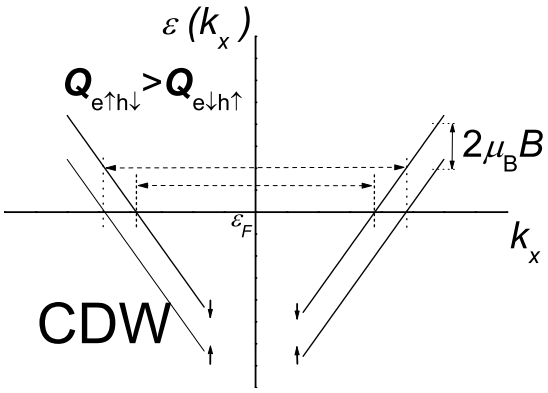

Figure 2.4: Due to the Zeeman splitting between different spin bands, the latter cannot be perfectly nested by a single wave vector in a CDW system.

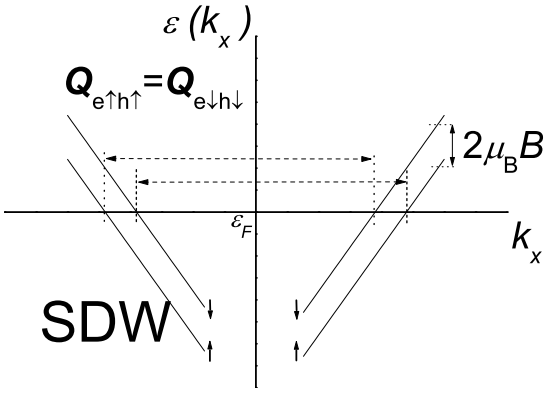

Figure 2.5: Due to the different pairing in SDW systems the nesting vector is unaffected. Therefore, the SDW does not become suppressed in magnetic field.

the Zeeman (or Pauli) effect. The energy difference between the bands is given by $\Delta\epsilon = g\mu_B B$, with μ_B being the Bohr magneton and $g \approx 2$. It then follows that in a CDW system electrons with spin in field direction (say spin up ($\uparrow$)) will have a Fermi wave vector k_F that is bigger than the one of spin down ($\downarrow$) electrons. Correspondingly, to become perfectly nested ($\uparrow$)-electrons would need a bigger nesting vector than the one at zero-field, while ($\downarrow$)-electrons would need a smaller one [13]. This means that since the system prefers to keep only one nesting vector [14], a magnetic field makes the CDW system energetically less favorable. This in turn causes the transition temperature T_c to decrease [26]. Since the Zeeman splitting normally is independent on the magnetic field direction this Pauli paramagnetic effect is isotropic.

For a CDW system, which is perfectly nested at zero field (CDW_0), it has been theoretically predicted that the nesting vector keeps the zero-field value Q_0 throughout the entire magnetic field range [14]. At high fields, when the Zeeman energy splitting approaches the value of the zero-temperature energy gap of the density wave, i.e. $\mu_B B \sim \Delta$, the CDW_0 state eventually becomes completely suppressed [26]. As for singlet superconductors, the CDW_0 is thus paramagnetic limited, Fig. 2.7. In fields above this limit and at low enough temperatures ($T < 0.56T_c(B = 0\ \mathrm{T})$) there is then a modulated CDW state, the so-called CDW_x state, expected [27,26,28,13,14], see Fig. 2.7. This state has a nesting vector, which is shifted along the conducting chain ("x"-) direction in order to gap at least one of the spin subbands. The transition from the normal metallic state to both CDW states is of second order, while the transition between the CDW_0 and CDW_x state is proposed to be of first or-

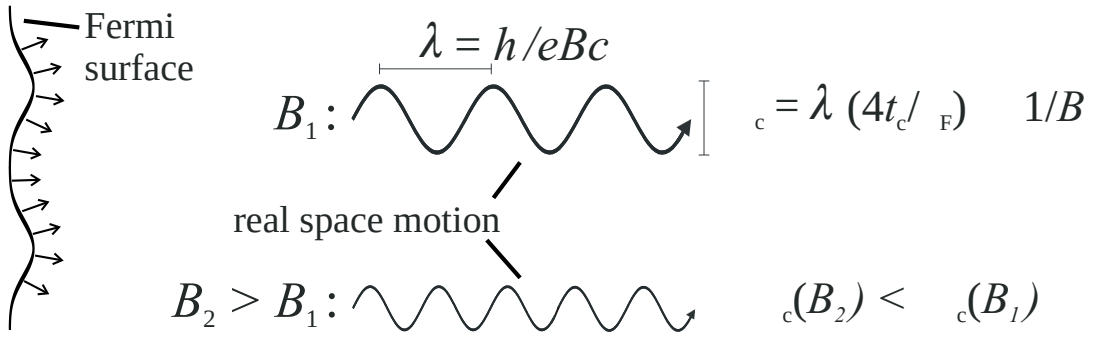

Figure 2.6: In a magnetic field, applied perpendicular to the conducting plane, the electrons travel along the open Fermi surface. In real space there will be a corresponding oscillating motion along the conducting chain direction. With increasing the field strength this oscillation becomes more restricted to the chain.

der [27, 26, 28, 13, 29]. Since the transition temperature of CDW systems is typically $\sim 10^2$ K, and correspondingly $\Delta(T = 0 \text{ K}) \geqslant 10$ meV, available static magnetic fields by far do not reach the critical field values at which the CDW_0 state becomes suppressed and the CDW_x stabilized.

In contrast to the CDW, a SDW is not affected by the splitting of the energy bands since the interacting electrons and holes have the same spin direction. As shown in Fig. 2.5 the best nesting vector remains unaffected in magnetic field.

As we will see next, the behaviour of T_c in an imperfectly nested system is more complicated due to the additional orbital effect of magnetic field in Q1D electron systems.

Orbital Effect

We again assume a Q1D electron system with a conducting **a-c** plane and a negligible dispersion in the third direction, Eq. (2.8). If an external field is applied perpendicular to the plane, the conduction electrons experience the Lorentz force and move along the open sheets on the Fermi surface. Since the electron velocity is always directed perpendicular to the Fermi surface there will thus be an oscillatory motion in real space, see (Fig. 2.6). On enhancing the magnetic field this oscillation will become more restricted to the conducting chain, $\Delta_c \propto 1/B$. This effective one-dimensionalization of the electron motion is interpreted as being the reason for a sta-

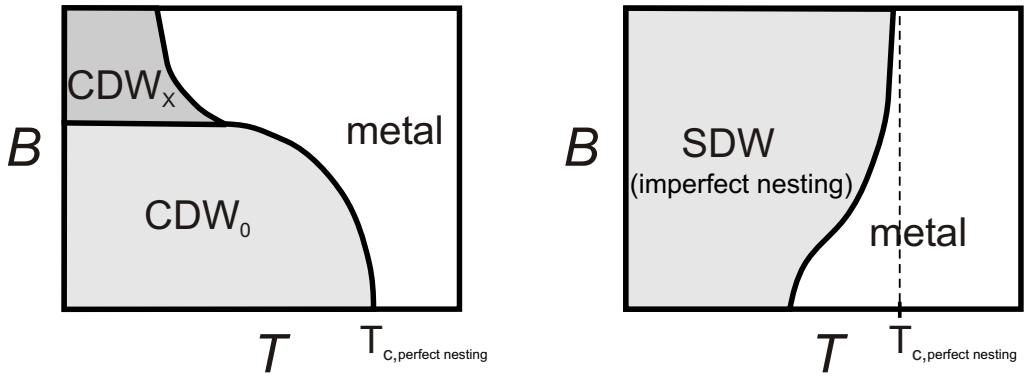

Figure 2.7: The perfectly nested CDW system is suppressed in magnetic field due to the Pauli effect, to the left. An imperfectly nested SDW system is on the other hand known to become stabilized in magnetic field due to the orbital motion of the carriers.

bilization of the imperfectly nested SDW state in magnetic field that is a well known characteristic of the Q1D SDW system [5, 2]. Within theoretical investigations this has indeed been shown to be directly reflected in an enhanced susceptibility (or response function) of an imperfectly nested SDW system. In relatively low magnetic fields this stabilization of the SDW was shown to lead to a quadratic enhancement of the transition temperature in field, which becomes stronger with worsening the nesting conditions [30, 22]. At high fields the transition temperature then saturates at the one of the perfectly nested system, Fig. 2.7 [30]. Several experimental works have confirmed this prediction on SDW systems [31, 32, 33].

For an imperfectly (Q1D) nested CDW system the orbital field effect has theoretically also been proposed [22, 34] and some indirect hints for its presence have indeed been observed in the title compound [12], although a direct evidence is still missing.

Thus, for such an imperfectly nested CDW system in a magnetic field there should be a competition between Pauli and orbital effects [14]. This will turn out to play an important role within the present work.

2.2 Magnetic Quantum Oscillations

2.2.1 Conduction Electrons in a Magnetic Field

Solving the Schrödinger equation for a free electron gas in a magnetic field, applied in z-direction, yields the energy eigenvalues [35]

$$E_{n,k_z} = (n + \frac{1}{2})\hbar\omega_c + \frac{\hbar^2}{2m_c}k_z^2, \tag{2.9}$$

with the cyclotron frequency given by $\omega_c = eB/m_c$, where m_c is the cyclotron mass, k_z being the electron's wave vector component parallel to the applied magnetic field and n an integer. The allowed electron states in k-space are now all lying on co-axial tubes parallel to the magnetic field also known as Landau tubes, Fig. 2.8. The area of the nth Landau tube cross section perpendicular to the field $A_{k,n} = \pi k_\perp^2$ is then expressed by the famous Onsager relation [36]:

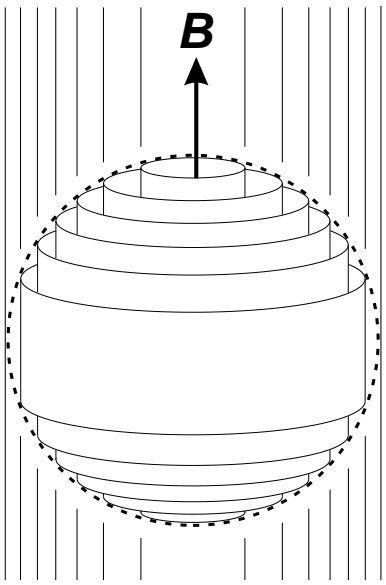

Figure 2.8: Free electrons condense on co-axial Landau tubes parallel to the applied magnetic field.

$$A_{k,n} = (n + \frac{1}{2})\frac{2\pi eB}{\hbar}. \tag{2.10}$$

For dispersion relations other than parabolic $\frac{1}{2}$ in this equation is replaced by a fractional correction λ which, however, in most cases takes a value [35] close to $\frac{1}{2}$. All electron states condense on the Landau tubes which therefore must be highly degenerated. Neglecting the electron spin the degeneracy is given by the ratio of the total flux through the sample to the flux quantum: $D = (e/(2\pi\hbar))BL^2$. As follows from the Onsager relation (2.10), with increasing field the Landau tubes cross a fixed point in k-space periodically in scale of 1/B. Thus, the density of states on the Fermi surface in a slice dk_z perpendicular to the applied magnetic field will also alter with the same period. On

a 3D Fermi surface the phase of the oscillations, when n is large, varies rapidly along k_z except near extreme cross-sections. It can then be shown [35] that the resulting oscillation of the total number of electrons on the Fermi surface is determined by this extremal area. The periodicity of the quantum oscillations becomes

$$\frac{1}{B_{n-1}} - \frac{1}{B_n} = \Delta\frac{1}{B} = \frac{2\pi e}{\hbar A_{k_z,extr}}; \tag{2.11}$$

and the frequency is proportional to the area of the extremal Fermi surface cross section perpendicular to the field direction, $A_{k_z,extr}$:

$$F = \frac{1}{\Delta\frac{1}{B}} = \frac{\hbar}{2\pi e}A_{k_z,extr}. \tag{2.12}$$

If there are several extrema there will be several frequencies contributing to the total oscillation. In the following we will show that these oscillations can be seen in measurable quantities and how one can extract useful information about the charge carriers.

2.2.2 The de Haas-van Alphen (dHvA) Effect

The magnetization of a system of conduction electrons is easiest calculated via the derivative of the thermodynamic potential Ω with respect to the magnetic field, keeping the chemical potential μ constant:

$$\overrightarrow{M} = -\left(\overrightarrow{\nabla}_{\overrightarrow{B}}\Omega\right)_{\mu}. \tag{2.13}$$

With field the energy of the system will oscillate which gives rise to oscillations of the magnetization. This effect has been discovered by de Haas and van Alphen in 1930 [37].

The thermodynamic potential for a system of conduction electrons obeying the Fermi-Dirac statistic is given by

$$\Omega = -k_B T \sum_{\epsilon} \ln\left(1 + \exp\left(\frac{\mu - \epsilon}{k_B T}\right)\right), \tag{2.14}$$

k_B is the Boltzmann constant and the sum is taken over all possible energy states ϵ. Taking into account the degeneracy and energy eigenvalues of the Landau levels one thus obtains the contribution from a slice dk_z perpendicular to the field:

$$d\Omega = -k_B T\left(\frac{eBV}{2\pi^2\hbar}\right)\sum_{n} \ln\left(1 + \exp\left(-\frac{(E_n - \mu)}{k_B T}\right)\right)dk_z. \tag{2.15}$$

This equation can now be solved at $T = 0$ K using the Poisson or the Euler-MacLaurin formulas [35]. At the final integration over k_z only slices in the vicinity of extremal areas add up constructively and the oscillation finally becomes:

$$\tilde{\Omega} = \sqrt{\frac{e^5}{8\pi^7\hbar}} \frac{VB^{\frac{5}{2}}}{m_{\text{eff}}\sqrt{A''}} \sum_{p=1}^{\infty} \frac{1}{p^{\frac{5}{2}}} \cos\Big[2\pi p\Big(\frac{F}{B} - \frac{1}{2}\Big) \pm \frac{\pi}{4}\Big] \tag{2.16}$$

where

$$A'' = \Big(\frac{\partial^2 A_{k_z}}{\partial k_z^2}\Big)_{k_z = k_z, extr} \tag{2.17}$$

From Eqs.(2.13) and (2.16) the magnetization components parallel and perpendicular to the field can thus be derived as:

$$\tilde{M}_{\parallel} = -\sqrt{\frac{e^5}{2\pi^5\hbar}} \frac{VF\sqrt{B}}{m_{\text{eff}}\sqrt{A''}} \sum_{p=1}^{\infty} \frac{1}{p^{\frac{3}{2}}} \sin\Big[2\pi p\Big(\frac{F}{B} - \frac{1}{2}\Big) \pm \frac{\pi}{4}\Big] \tag{2.18}$$

$$\tilde{M}_{\perp} = -\frac{1}{F}\frac{\partial F}{\partial \theta}\tilde{M}_{\parallel} \tag{2.19}$$

with m_{eff} being the effective cyclotron mass, which, in the absence of electron-electron and electron-phonon interactions, equals to the band structure effective mass.

On taking into account effects of finite temperature, electron scattering and Zeeman spin splitting in magnetic field several independent reduction factors R_T, R_D and R_S have to be added to Eq. (2.18). Since it is especially these factors that give information about the electronic properties of the system we will focus on them in the next section. Including these damping factors into Eq. (2.18), one finally obtains the famous Lifshitz-Kosevich (LK) equation describing the de Haas-van Alphen (dHvA) oscillations in a 3D metallic electron system which, in the case of one extremal orbit, reads:

$$\tilde{M}_{\parallel} = -\sqrt{\frac{e^5}{2\pi^5\hbar}} \frac{F\sqrt{B}}{m_{\text{eff}}\sqrt{A''}} \sum_{p=1}^{\infty} R_D(p)R_T(p)R_S(p)\frac{1}{p^{3/2}} \sin[2\pi p(\frac{F}{B} - \frac{1}{2}) \pm \frac{\pi}{4}] \tag{2.20}$$

In polyvalent metals the FS generally exhibits more than one extremal cross-sectional area. In that case, the total oscillatory part of the magnetization is simply the sum over all contributions, each of them having the form (2.20), but with different parameters F, m_{eff}, A'' and R_T , R_D, R_S.

2.2.3 Reduction Factors

The temperature reduction factor R_T

At finite temperatures the Fermi distribution function

$$f(\epsilon) = \frac{1}{(1 + \exp(\frac{\epsilon-\mu}{k_B T}))} \tag{2.21}$$

is no more step-like at the Fermi level. The whole system can now be treated as a distribution of hypothetic metals, all at $T = 0$ K, having different Fermi energies and hence contributing to the system with different frequencies. The superposition of these oscillations, weighted according to the Fermi distribution, will cause a damping of the initial oscillation. For the p-th harmonic this damping can be shown to be expressed by the factor [35]:

$$R_T(p) = \frac{\alpha p m^* \frac{T}{B}}{\sinh(\alpha p m^* \frac{T}{B})} \tag{2.22}$$

with the constant

$$\alpha = \frac{2\pi^2 k_B m_e}{\hbar e} \approx 14.69 \frac{\mathrm{T}}{\mathrm{K}} \tag{2.23}$$

and the effective cyclotron mass m^* in relative units of the free electron mass, $m^* = m_{\mathrm{eff}}/m_e$. Thus, by fitting the experimentally observed temperature dependent amplitude with Eq. (2.22), one can extract m^*. This mass is renormalized by electron-electron and electron-phonon interactions.

The Dingle Factor R_D

Conduction electrons possess a finite relaxation time τ mostly caused by lattice imperfections and impurities. Due to the uncertainty principle this leads to a broadening of the otherwise δ-shaped Landau levels. Assuming this broadening to be described by the Lorentzian distribution function the system can be treated in a similar way as for finite temperature. The effect on the p-th harmonic of the oscillation amplitude is then given by the Dingle reduction factor [35, 38]:

$$R_D = \exp\Big(- \alpha \frac{p m_b T_D}{B} \Big) \tag{2.24}$$

with T_D being the so-called Dingle temperature,

$$T_D = \frac{\hbar}{2\pi k_B \tau}. \tag{2.25}$$

If the effective band mass m_b is known, the evaluation of the Dingle temperature via the field dependence of the oscillation amplitude is possible, and with it a measure of the crystal quality. Contrary to the effective cyclotron mass m^* introduced above the effective band mass m_b is not renormalized due to electron-phonon interactions. It should therefore be kept in mind that the use of m^* instead of m_b in (2.24), that is a common procedure in the field of organic metals, can falsify the evaluation of the Dingle temperature.

The Spin Reduction Factor R_S

In a magnetic field, the Zeeman splitting lifts the spin degeneracy of the electron energy. Accordingly, a Landau level of energy ϵ splits into sub-levels separated by an energy gap

$$\Delta\epsilon = g^* \mu_B B; \tag{2.26}$$

where $\mu_B = \frac{e\hbar}{2m_e}$, and g* is the Landé factor (for free electrons g*=2.0023). These two sets of Landau levels contribute to the oscillation at the same frequency but with a phase difference given by

$$\phi = 2\pi \frac{\Delta\epsilon}{\hbar\omega_c} \tag{2.27}$$

The superposition of these "spin up" and "spin down" oscillations causes an additional spin reduction factor. For the p-th harmonic it may be written by [35]

$$R_s = cos(\frac{1}{2} p\phi) = \cos(\frac{1}{2} p\pi g^* m^*) \tag{2.28}$$

with m^* being the effective cyclotron mass introduced above. Like m^*, g^* is renormalized by electron-electron and electron-phonon interactions.

2.2.4 Shubnikov-de Haas (SdH) Oscillations

Shortly before the first experimental observation of the dHvA effect, Shubnikov and de Haas [39] found quantum oscillations in transport measurements on a Bi single

crystal. This phenomenon is therefore called Shubnikov-de Haas (SdH) oscillations. The detailed theory of this effect, considering different kinds of scattering processes, developed by Adams and Holstein in 1959 [40], is far beyond the scope of this introductional chapter. However, a satisfactory description of the SdH effect is usually obtained following Pippard's idea that the scattering probability, and hence the resistivity, is directly proportional to the density of states around the Fermi level. The latter can be shown to be directly proportional to the field-derivative of magnetization [35, 41]:

$$\tilde{D}(\mu) \propto \left(\frac{m_c B}{A_{kz,extr}}\right)^2 \frac{\partial \tilde{M}}{\partial B}. \tag{2.29}$$

This gives an oscillatory part of the conductivity that may be expressed by:

$$\frac{\tilde{\sigma}}{\sigma_0} = \sum_{p=1}^{\infty} \frac{1}{p^{\frac{1}{2}}} a_p \cos\left[2\pi\left(\frac{F}{B} - \frac{1}{2}\right) \pm \frac{\pi}{4}\right], \tag{2.30}$$

where

$$a_p \propto \frac{m_c B^{\frac{1}{2}}}{A''^{\frac{1}{2}}} R_T(p) R_D(p) R_S(p) \tag{2.31}$$

and σ_0 is the background conductivity. One sees, that the same damping factors as for the dHvA effect can be used in order to extract properties of the electron system. In the field of organic conductors this has been indeed shown in many cases to be applicable [9].

2.2.5 Influence of Two-Dimensionality

The above derivation of magnetic quantum oscillations strictly works only for a 3D Fermi surface. Since in the field of organic metals most conduction systems are Q2D we point out differences which should be taken into account in such systems. The most significant difference is the following: in a 3D metal many Landau levels cross the Fermi surface and therefore contribute to the quantum oscillations, see Fig. 2.8. This eventually leads to smooth sinusoidal oscillations with the frequencies determined by extreme areas. In a highly Q2D system nearly the whole Fermi surface is "extreme" and is crossed by only few Landau tubes around the Fermi energy, as sketched in Fig. 2.9. This gives rise to a strong oscillatory behaviour. Moreover, if the distance between subsequent Landau tubes becomes larger than the warping of the Fermi surface cylinder, the chemical potential becomes pinned to the nearest

Landau level: It increases with field until the highest level becomes completely unoccupied and an abrupt jump down to the lower level occurs. This is immediately reflected in a sawtooth shape of the dHvA signal, causing higher harmonic contents of the oscillation [35]. On the other hand, if there are additional, non-quantized bands on the Fermi surface, these will act as a carrier reservoir.

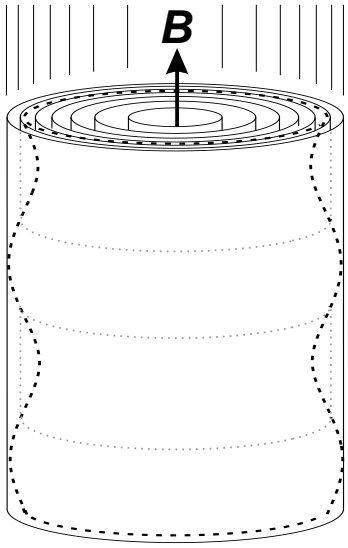

Figure 2.9: Only a few Landau levels cross a weakly warped cylindrical Fermi surface, characteristic of a Q2D metal, in a magnetic field applied in the least conducting direction.

In the (hypothetical) limit of an infinite reservoir the chemical potential becomes again constant and the dHvA oscillation takes the form of an inverse saw tooth [35]. However, since the carrier reservoirs in real systems are finite such an extreme case cannot be used to describe the shape of the oscillations. Taking into account both the oscillations from the quantized 2D band and the reservoir bands, it can be shown that the oscillation again takes a more symmetric shape in comparison to the above extreme cases [42]. Noteworthy, the temperature reduction factor might be affected by the low dimensionality. However, relevant changes in the amplitude of the first harmonic are only expected at very low temperatures and/or very high magnetic fields, i.e. $\hbar\omega_c/kT \gg 10$ [42, 43, 44]. Otherwise, the extraction of the effective mass from the temperature dependence of the oscillations, as described above in sec. 2.2.3, should still be valid. The envelope of the oscillations in a changing magnetic field, however, might be strongly affected so that a determination of the Dingle temperature T_D, as described above may be incorrect. Concerning the SdH oscillations in very anisotropic Q2D systems the situation will become even more complicated as will be pointed out in this work.

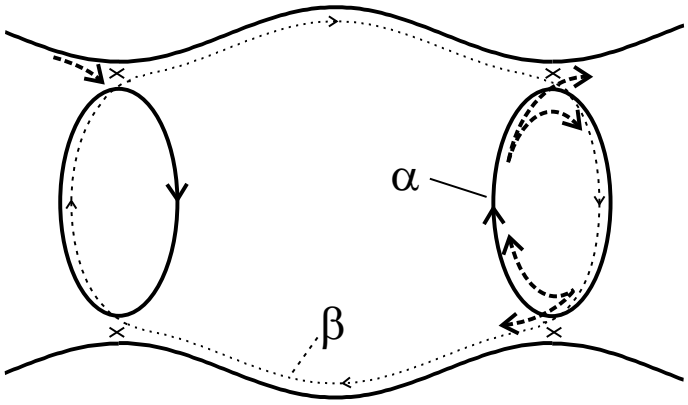

Figure 2.10: Example of magnetic breakdown between open and closed trajectories: In magnetic field the carriers on the Fermi surface have a finite probability to tunnel between different bands, dashed lines. This may lead to additional closed orbits, here: β-orbit, dotted line.

2.2.6 Magnetic Breakdown

The LK formula derived above only considers electrons on well defined closed orbits on the Fermi surface. There exists, however, another possibility in magnetic field for the electrons in multiband metals to run on closed pockets on the Fermi surface by tunneling processes between the bands, that is called magnetic breakdown (MB). Fig. 2.10 illustrates this phenomenon in the case of coexisting open and closed parts of the Fermi surface, that is typically found in many organic metals. If the energy barrier ϵ_g between neighboring trajectories is small in comparison to the Fermi energy there will be a finite probability for the electrons in a strong magnetic field to tunnel between the bands. This may lead to an additional orbit (here: β-orbit) contributing to the quantum oscillations. The probability of MB can be expressed as [45]

$$P = \exp\left(-\frac{B_0}{B}\right), \tag{2.32}$$

where the MB field parameter B_0 is defined as

$$B_0 \approx \frac{m^* \epsilon_g^2}{e\hbar\epsilon_F}. \tag{2.33}$$

With increasing field, referring to Fig. 2.10, more electrons will tunnel between the bands causing a bigger contribution to the β-oscillations while less electrons run on the semiclassical trajectories along the open and closed parts on the Fermi surface.

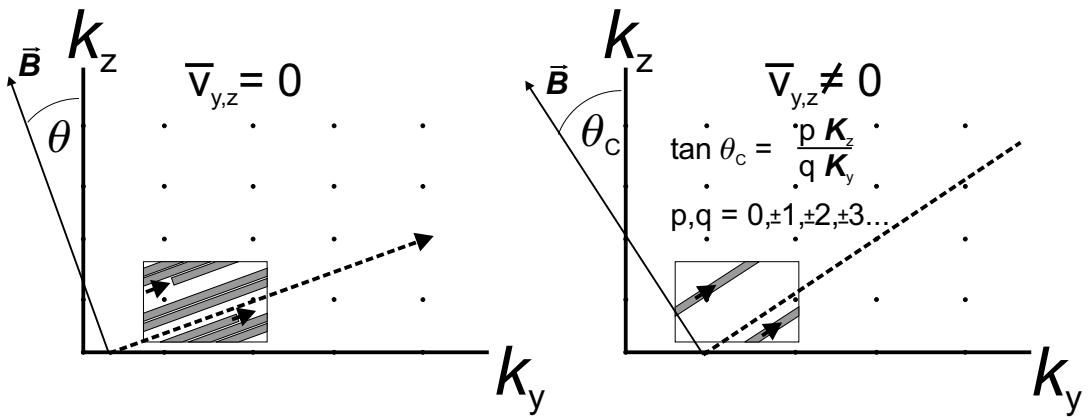

Figure 2.11: Due to the Lorentz force in magnetic field electrons move along the open sheets of the Fermi surface. If the trajectory does not run along a reciprocal lattice vector the electron path covers the whole area of the sheets, left picture. Otherwise the trajectory only consists of a few lines on the Fermi surface, right picture.

2.3 Angle-dependent Magnetoresistance Oscillations

Besides the SdH effect, the angle dependent (semiclassical) magnetoresistance oscillations turned out to be another powerful tool for studying the Fermi surface geometry. These oscillations, basically being caused by geometrical effects of the Fermi surface, will be briefly presented in the following.

2.3.1 Quasi-One-Dimensional Electron Systems

The dispersion relation for a Q1D electron system with conducting chains along the x-direction may be expressed near the Fermi level, as:

$$\epsilon(k) = \hbar v_F(\mid k_x \mid -k_F) - \sum_{m,n} t_{mn} \cos(m a_y k_y + n a_z k_z) \tag{2.34}$$

with the transfer integrals $t_{mn} \ll \epsilon_F$ and the lattice constants perpendicular to the chains $a_{y,z}$. In a magnetic field applied parallel to the open sheets of the Fermi surface, i.e. within the y-z plane, electrons move along the Fermi surface perpendicular

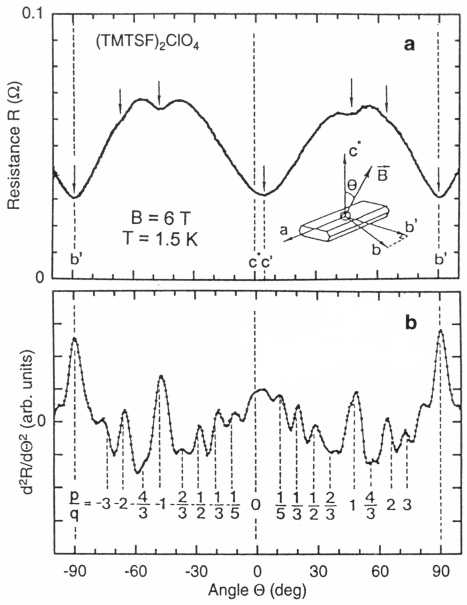

Figure 2.12: a) Q1D AMRO in the organic compound $(TMTSF)_2ClO_4$ exhibiting pronounced dips at angles expected from the theory [46]. b) Second derivative of the curve in a) clearly showing the modulated structure. For the definition of p and q see text, from [9].

to the field. Their velocity components in z and y direction, given by $v_{y,z} = \frac{1}{\hbar}\frac{\partial \epsilon}{\partial k_{y,z}}$, continously change (in fact they oscillate) and the mean velocity is given by an average over the scattering time τ. It then becomes evident that whilst τ is large for most field directions the electron path in momentum space will cover the whole reduced Brillouin zone, see Fig. 2.11. Hence, the electrons take all possible k-states on the Fermi surface and the averaged values $\overline{v_{y,z}}$ tend to become zero. However, if the field is oriented so that the trajectory runs along a reciprocal lattice vector, $\mathbf{K} = p\mathbf{K_y} + q\mathbf{K_z}$, the final path in the reduced Brillouin zone consists only of a few lines, as illustrated in Fig. 2.11. In this case, the field is directed (in real space) along a vector of one of the transfer integrals. Since the corresponding carrier motion in this direction is not affected by the Lorentz force, $\overline{v_{y,z}}$ keeps a finite value. Therefore, at special angles, θ_c, between the magnetic field direction and the k_z axis, satisfying the condition

$$\tan\theta_c = \frac{q\mathbf{K_z}}{p\mathbf{K_y}}, \tag{2.35}$$

dips of the resistivity components ρ_y and ρ_z can be expected. Indeed, such Q1D AMROs were found in the TMTSF based compounds possessing only two open sheets on its Fermi surface [47, 48, 49, 50]. An example of the measured magnetoresistance

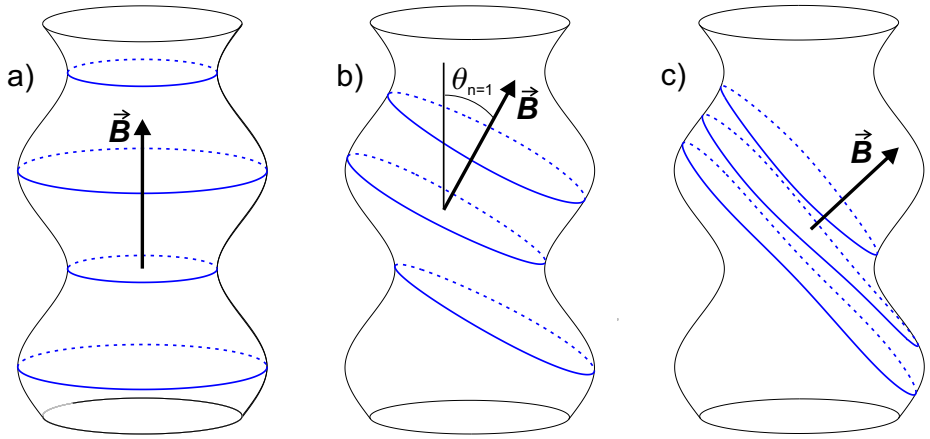

Figure 2.13: Closed electron orbits on a slightly warped cylindrical Fermi surface at different magnetic field directions: a),b),c). Only for certain field directions (b) all orbit areas are the same.

is given in Fig. 2.12 for the organic metal $(TMTSF)_2ClO_4$.

2.3.2 Quasi-Two-Dimensional Electron Systems

Besides the Q1D AMRO there exists another angular effect arising from a cylindrical Fermi surface, i.e. a Q2D electron system [51, 52, 53, 54]. By contrast to the Q1D AMRO, described above, these happen to appear only in the interplane resistance [55]. The simplest energy dispersion for a Q2D system may be expressed as:

$$\epsilon(k) = \frac{\hbar^2}{2m^*}(k_x^2 + k_y^2) - 2t_\perp \cos(a_z k_z) \tag{2.36}$$

The Fermi surface is thus represented by a cylinder slightly warped in k_z-direction. The 2D AMRO now occurs due to a simple geometrical fact. With tilting the magnetic field towards the conducting plane, angles appear at which the areas of all cyclotron orbits becomes independent of the plane position, K_z: i.e. $\frac{\partial A}{\partial K_z} = 0$, see Fig. 2.13. Since in a magnetic field the mean velocity $\overline{v_z}$ of an electron around one orbit can be derived as [54]:

$$\overline{v_z} = \frac{1}{\hbar}\overline{\partial\epsilon/\partial k_z} = -\frac{1}{\hbar}\frac{\partial A(K_z)/K_z}{\partial A/\partial\epsilon} = -\frac{1}{\hbar}\cdot\frac{\partial A(K_z)/K_z}{2\pi m_c}, \tag{2.37}$$

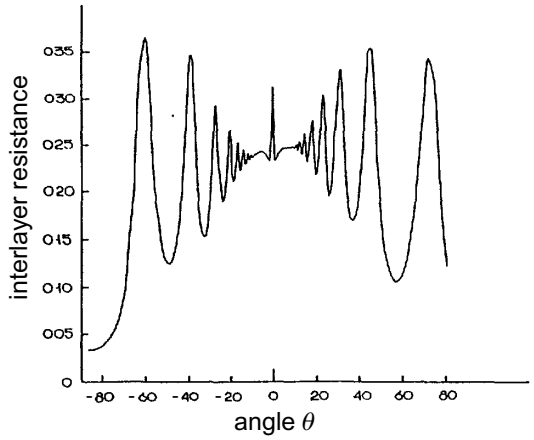

Figure 2.14: 2D AMRO observed in the Q2D organic compound β-(BEDT-TTF)$_2$IBr$_2$, from [54].

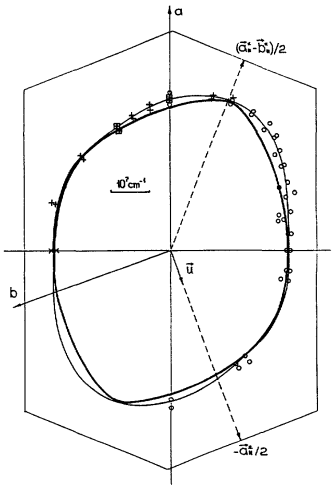

Figure 2.15: Extracted Fermi surface within the a-b plane (thick line) [54].

one thus expects peaks to occur in the magnetoresistance at those specific angles. They are given by [51]

$$\tan(\theta_n) = \frac{\pi}{a_z k_F}(n - \frac{1}{4}). \tag{2.38}$$

This equation, however, only holds for a circular basal plane of the FS cylinder. In real systems the basal plane has typically a lower symmetry and, additionally, the vector $\mathbf{h}$ of the interlayer transfer integral has an inplane component $\mathbf{u}$, i.e. $\mathbf{h} = (u_x, u_y, h_z)$. The above condition (2.38) for maxima in the resistance then becomes [54]:

$$\tan\theta_n(\varphi) = \frac{\pi(n \mp \frac{1}{4} + (\mathbf{k}_\parallel^{max}(\varphi) \cdot \mathbf{u})}{k_B^{max}(\varphi) \cdot a_z}, \tag{2.39}$$

where the signs $-$ and $+$ correspond to positive and negative θ, respectively, $\mathbf{k}_\parallel^{max}(\varphi)$ is the Fermi wave vector component within the x-y-plane for which the projection onto the field rotation plane, $k_B^{max}(\varphi)$, becomes maximal and φ determines the direction of the rotation plane within the x-y plane. By use of Eq. (2.39), a determination of the Fermi surface cross section is possible via the angular positions of the resistance maxima at different φ. An example of an AMRO observed in the Q2D organic compound β-(BEDT-TTF)$_2$IBr$_2$ together with the determined inplane Fermi surface is shown in Fig. 2.14 and Fig. 2.15 [54].

2.4 Kohler's Rule

In a magnetic field $\overrightarrow{B}$ the motion of an electron is affected by the Lorentz force, causing (at least for closed Fermi surfaces) a curving of the electron trajectory in the plane perpendicular to the applied field. The characteristic size of this curving is given by the magnetic length (Larmor radius in the case of closed orbits) which is inversely proportional to the magnetic field B and is given by the electron velocity divided by the cyclotron frequency $\omega_c = \frac{eB}{m_c}$. As a result, the effective mean free path in the direction of the electric field decreases and the resistivity ρ in that direction increases. For anisotropic metals it has turned out to be extremely difficult to calculate the field dependence of the resistivity in moderate fields, i.e. fields where $\omega_c\tau \sim 1$, τ being the electron scattering time. Because of this, use is sometimes made of Kohler's rule, which is a similarity law for the magnetoresistance. A summary of its derivation given by Pippard [56] is presented below.

A bunch of electrons, all having the same initial wave vector $\overrightarrow{k}$ on the Fermi surface, give a current contribution in a steady electric field $\overrightarrow{E}$ (with or without an applied magnetic field), that can be written as [56]:

$$\delta\overrightarrow{J} = \frac{e^2\overrightarrow{E}\delta\overrightarrow{S}}{4\pi^3\hbar}\overrightarrow{L}, \tag{2.40}$$

$\delta\overrightarrow{S}$ being an element of the Fermi surface. $\overrightarrow{L}$, the effective path, is defined as the mean vector distance traveled by each electron from the bunch until the centroid of them comes to rest due to scattering. One can treat this effective path as a k-dependent mean free length for electrons in a given magnetic field. In an applied magnetic field, this bunch of electrons moves on orbits, with linear dimensions inversely proportional to B, and dissipate by collisions. The idea is to look what would happen, if the scattering rate is increased by a factor a, for example by adding impurities, and at the same time the magnetic field B is also enhanced to the same amount, $B' = aB$. If these "extra" collisions, causing the reduced scattering time $\tau' = \tau/a$, are of the same sort, the pattern of the electronic behaviour should be simply scaled down without changing the character. This implies, that the scattering rate does not depend on the magnetic field. In this case the effective path L and all components of the conductivity will be divided by a and any measured resistivity multiplied by this factor, $\rho'(B) = a\rho(B)$. This means that if we keep the ratio $B/\rho_{\text{zero-field}}$ constant, on the one hand the probability of an electron to be scattered over one cycle of the orbit remains constant ($\omega_c\tau$ = const.). Then

on the other hand, the magnetoresistance, which is the resistivity normalized to its zero-field value, remains the same; i.e.:

$$\frac{\rho'(B)}{\rho'_{\text{zero-field}}} = \frac{a\rho(B)}{a\rho_{\text{zero-field}}} = \frac{\rho(B)}{\rho_{\text{zero-field}}} = \text{const.} \tag{2.41}$$

In other words, the magnetoresistance is a general function of the magnetic field divided by the zero-field resistance:

$$\frac{\Delta\rho(B)}{\rho_{\text{zero-field}}} = F(\frac{B}{\rho_{\text{zero-field}}}); \Delta\rho = \rho(B) - \rho_{\text{zero-field}}. \tag{2.42}$$

This is *Kohler's rule.*

Since this law is derived using certain assumptions, one should be careful as to which cases it can or cannot be used. Some examples for which the rule fails are given in the following:

- If the scattering time is field dependent, Kohler's rule is no longer valid. This would be the case, for example, when the scattering is due to magnetic impurities.
- Effects of orbit quantization will also break the law because the scattering rate becomes field dependent in a way that it starts oscillating.
- In the case of a magnetic breakdown, the electrons have a finite probability (depending on the magnetic field) to switch to another band, that will cause a different current distribution in real space and therefore a deviation from Kohler's rule.
- If there is a large content of phonon scattering, the modification of the phonon spectrum with changing the temperature results in an altered scattering pattern. One of the basic assumptions made for Kohler's rule is not fulfilled.
- If there is a phase transition to another (conducting) state on changing the temperature and/or magnetic field, the scattering pattern will be altered. Therefore, Kohler‘s rule in some cases can even be used for the determination of such phase transitions.

Chapter 3

The Organic Metal α-(BEDT-TTF)$_2$KHg(SCN)$_4$

3.1 Synthesis

Single crystals of α-(BEDT-TTF)$_2$KHg(SCN)$_4$ are prepared using standard electrochemical techniques [57, 2]. The salts KSCN and Hg(SCN)$_2$ are dissolved in a mixture of (1,1,2)trichlorethane and methanol. Organic BEDT-TTF (often shortened to ET) molecules are then electrochemically oxidized in this solution by applying a constant current between Pt-electrodes, the initial salts serving as electrolytes. To initiate crystal growth the current density is kept at a very low level of about 1-2 μA/cm^2 while the temperature is held at the constant value of 20°C. After 2-4 weeks small plate-like samples with a typical size of 0.5*0.5*0.1 mm^3 appear on the Pt-anode. In our measurements samples were taken from different batches, some prepared by N.D.Kushch in the WMI , others by H.Müller at the ESRF in Grenoble.

3.2 Crystal Structure

All the charge transfer salts (BEDT-TTF)$_m$X$_n$ have a nearly planar donor molecule BEDT-TTF due to an extended π-electron orbital system [58, 2]. The crystal struc-

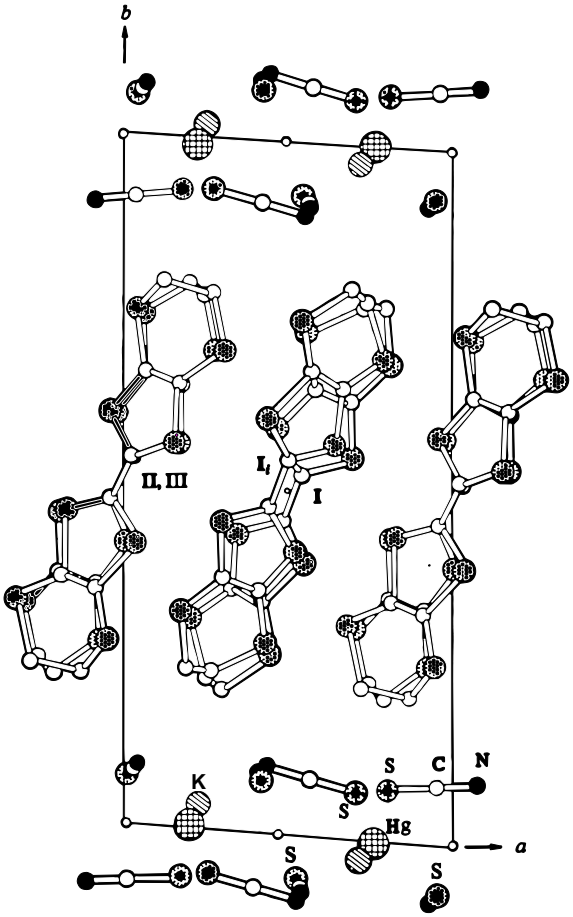

Figure 3.1: Crystal structure of α-(BEDT-TTF)$_2$KHg(SCN)$_4$. The BEDT-TTF molecules arrange in conducting planes which are separated by insulating anion layers [57].

ture of α-(BEDT-TTF)$_2$KHg(SCN)$_4$ is illustrated in Fig. 3.1. It contains conducting cation-radical layers of BEDT-TTF, within the crystallographic **a-c** plane, alternating along the **b**-axis with relatively thick polymeric insulating anion layers [57]. Within the BEDT-TTF sheets, the molecules are connected via π-orbitals between the sulfur atoms. The transfer of charge between the layers results in stable crystalline materials. In the anion sheets each SCN molecule forms a bridge between the K^+ and Hg^{2+} cations leading to a polymeric network in the **a-c** plane. This layered structure is typical for (BEDT-TTF)$_2^+$X$^-$ compounds. Depending on different anions, the BEDT-TTF molecules are arranged within the layer in different formations, which are denoted by Greek characters. In the α-type salt with the anion $[KHg(SCN)_4]^-$ the BEDT-TTF donors are ordered in stacks, labeled A and

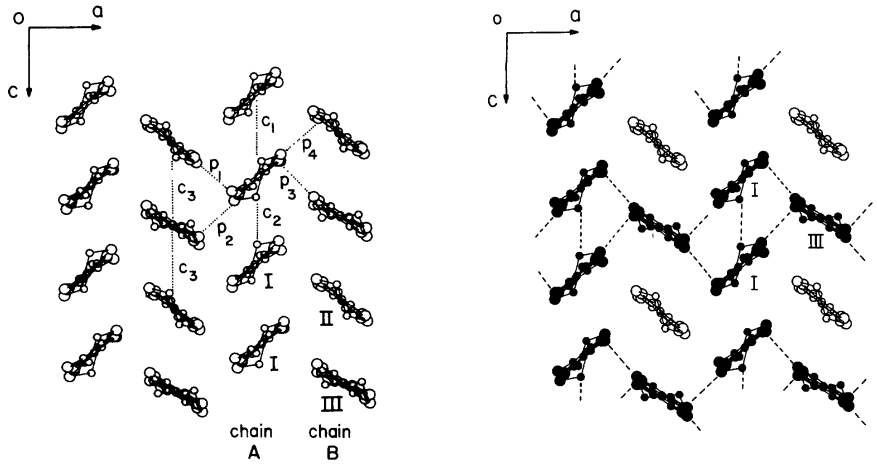

Figure 3.2: Left: Inplane arrangement of the ET molecules viewed along their molecular axis. The dotted lines between the molecules stand for the different transfer integrals in the stack direction (c_i) and interstack direction (p_i). Right: Molecular chains in the **a**-direction (black) give rise to a Q1D electron motion.

B, with a characteristic "fish bone" pattern (Fig. 3.2). The molecules in stack B are located in non-equivalent inversion centres marked II and III, whereas in stack A they are in equivalent positions I. Therefore the unit cell contains two formula units. The crystal structure is triclinic with the parameters a=10.082Å, b=20.565Å, c=9.973Å, α=103.7°, β=90.91°, γ=93.06° and a cell volume of 1997 Å^3.

3.3 Fermi Surface and Band Structure

Since two BEDT-TTF molecules give one electron to the anion leaving a hole behind, there are two holes in one unit cell, the latter containing four BEDT-TTF molecules. This means, that there will exist four HOMO(= highest occupied molecular orbital) bands, which are filled with six electrons per unit cell. Due to the fact that the upper two bands (in energy scale) overlap [57], both of them cross the Fermi level, i.e. the BEDT-TTF sheets possess a metallic character. Small overlaps of the molecular orbitals of adjacent BEDT-TTF layers lead to an electron exchange between them and thus to a finite conductivity perpendicular to the highly conducting planes. The band structure determined by Mori et al. [59] via an extended Hückel tight-binding calculation, based on the crystal structure at 100 K, and the corresponding Fermi

surface within the conducting **a-c** plane are shown in Fig. 3.3. This method of computing band structures has turned out to be quite successful, in that it qualitatively agrees with the experimental data, in the case of organic metals [9, 2]. Due to the finite conductivity in the interplane direction, the Fermi surface is slightly warped along the b*-axis, the direction perpendicular to the picture in Fig. 3.3. From the observed ratio of the in- to interplane conductivity, $\sigma_{\parallel}/\sigma_{\perp} \approx 10^5$ [60], a lower limit for the ratio of the effective in- to interlayer transfer integrals can be evaluated to be ≈ 300 [21]. The Fermi surface contains open sheets and closed cylindrical parts, respectively corresponding to Q1D and Q2D electron systems. The closed orbit gives rise to quantum oscillatory effects in magnetic field and the frequency of the SdH and dHvA oscillations yields the orbit area equal to 16 % of the Brillouin zone cross section [9]. The Q1D band mostly originates due to the fact that the transfer integrals labeled p_1, p_4, c_3 and to some extent also c_1 cancel each other [57]. This results into conducting chains, provided via p_2 and p_3, as depicted in Fig. 3.2. The Fermi energy may be estimated, e.g. via quantum oscillations measurements, to the extremely low value of ≈ 300 K.

Thus we see that although organic metals are chemically very complex, the electronic systems, i.e. Fermi surfaces, turn out to be beautifully simple. This is one of the most attractive properties of organic metals. Such electron systems can be described theoretically much easier than other conducting materials. They therefore may be regarded as model substances for theoretical investigations. This includes studies of quantum oscillations arising from the slightly warped cylinders as well as investigations of low temperature ground states in metallic systems mainly owing to the instability of the Q1D electron system.

3.4 The Low Temperature Ground States

During the last decade the family of organic metals α-(BEDT-TTF)$_2$MHg(SCN)$_4$, M=NH_4, K, Tl, Rb has become a subject of intense interest in the field of organic metals. The reasons for this are twofold. First, they appear to "span a boundary" between superconducting and density wave groundstates [9, 61]. While the compound with M = NH_4 happens to undergo a superconducting transition at about 1 K [62,63], otherwise showing a normal metallic (NM) behaviour, the other members of this family possess a density wave ground state with slightly varying transition

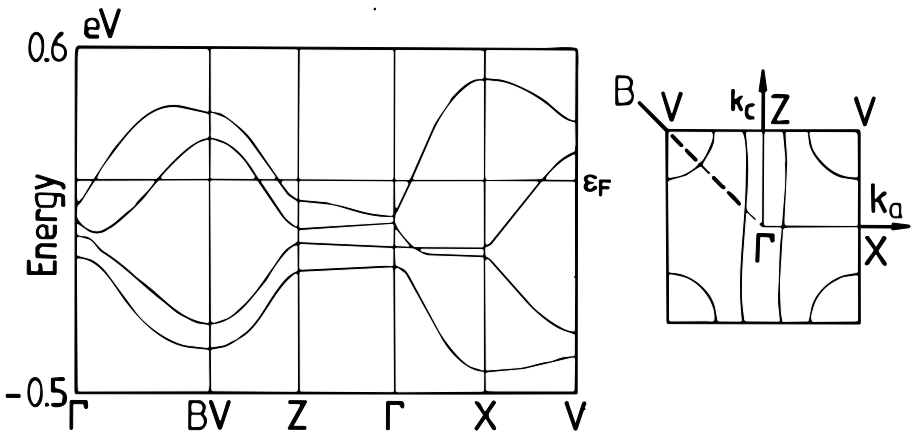

Figure 3.3: Band structure and Fermi surface of α-(BEDT-TTF)$_2$KHg(SCN)$_4$ calculated by Mori et al. [59]. For newer results see also ref. [57].

temperatures of 8 K (M=K), 9 K (M=Tl) and 12 K(M=Rb). After a long series of investigations there is nowadays a general agreement that it is the charge density which becomes modulated at low temperatures. Since the transition temperatures of these compounds are uniquely low, an investigation of a CDW system becomes possible in an extremely wide range of its B-T phase diagram, giving the other main reason for the broad interest in these compounds. This section gives a short review on the most important observations on the low temperature state known by the beginning of this work, mainly focusing on the M = K salt.

Historically, the K-compound was the first one to attract attention due to an extremely anomalous magnetoresistance observed by Osada et al. in 1990 [10]. As shown in Fig. 3.4, the transverse magnetoresistance starts to decrease with field above $\approx$ 10 T followed by a pronounced kink structure at $\approx$ 24 T. In addition, the angle dependent magnetoresistance oscillation (AMRO) turned out to possess dips rather than the, by that time, expected peaks from the 2D conducting band of

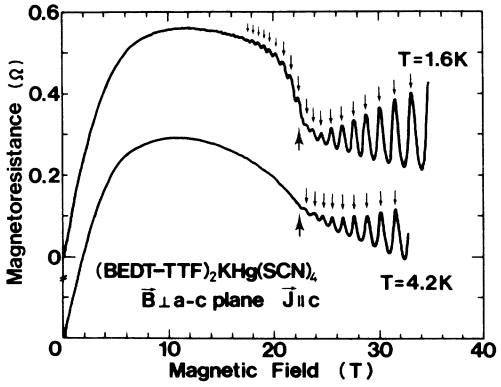

Figure 3.4: Transverse magnetoresistance data observed by Osada et al. in 1990 [10].

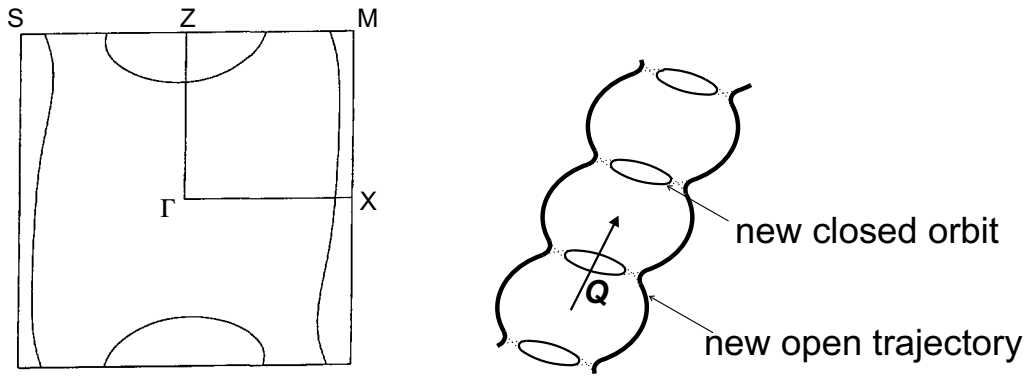

Figure 3.5: Left: Fermi surface of the normal metallic state calculated by Rousseau et al. [57]. Right: Within the CDW state the open sheets on the Fermi surface become completely nested, while the cylindrical parts are reconstructed. The new periodicity given by the nesting vector creates new closed orbits and open trajectories.

the electron system, introduced in section 2.3. Indeed, the AMROs in the low temperature state of these α-salts turned out to be caused by open sheets on the Fermi surface [11, 64]. This type of AMRO had already been observed in the Q1D organic metal (TMTSF)$_2$ClO$_4$ [65, 48, 49, 50] and could be reasonably described by a theory developed by Osada et al. in 1992 [46].

Surprisingly, these open sheets were found to be tilted by an angle of $\approx 20°$ within the conducting plane with respect to the proposed ones from band structure calculations [59, 57], Fig. 3.3. From the observed data it was possible to determine the periodicity of an additional periodic potential that has to be superposed on the system at low temperatures. Kartsovnik et al. [11] attributed this additional potential to a Peierls-type transition of the system that causes a reconstruction of the Fermi surface. How this schematically looks like within the **a-c**-plane is depicted in Fig. 3.5. The wave vector of the additional potential nests the Q1D part of the Fermi surface completely and therefore the Q1D carriers become gapped. The remaining Q2D part is then periodically shifted by the nesting vector building a reconstructed Fermi surface. As a result, there exist open sheets on the Fermi surface, running along the nesting wave vector and in between smaller pockets get formed. Indeed, Kartsovnik et al. in the same work presented additional SdH frequencies which were then attributed to these small pockets. As is evident, the orientation of the new Q1D sheets and the area of the new pockets will strongly depend on the exact coordinates of the nesting vector. The latter was proposed by Kartsovnik et al. [64, 66] to be

expressed by:

$$\mathbf{Q} = \frac{1}{8}\mathbf{K_a} + \frac{1}{8}\mathbf{K_c} + \frac{1}{6}\mathbf{K_b}, \tag{3.1}$$

which is tilted within the plane from the c-axis by $\approx 20°$, $\mathbf{K_{a,c,b}}$ being the reciprocal lattice vectors. However, since the nesting vector determined by other groups from AMRO measurements for unclear reasons are slightly more tilted, 27° [67] and 30° [68], there is up to now no general agreement about how the Fermi surface is reconstructed.

After this finding of a nested Fermi surface a long debate started about the nature of the density wave state. Due to a drop in the inplane magnetic susceptibility on crossing the phase boundary at $\approx$ 8 K, while the interplane component remains unchanged, Sasaki et al. [69] concluded that the low temperature state orders antiferromagnetically and therefore should emerge due to the presence of a SDW. Such a suggestion was then supported by μSR measurements [70], in which possible ordered magnetic moments of $\approx 10^{-3}\mu_B$ were predicted. However, besides the fact that this was the only μSR study reported on this compound, ESR [71] and NMR [72] investigations could not detect any magnetic ordering at low temperatures down to $\approx 10^{-4}\mu_B$, while a clear reduction of the density of states on entering the low temperature state has been observed. Moreover, Christ et al. [73, 74] have shown that the drop in the susceptibility within the plane is isotropic, revealing an "easy plane" rather than an "easy axis", that would be highly unusual for a SDW in its conventional form [2].

Due to the various anomalies found in magnetic field and also since no direct evidence for either spin- or charge density wave was found, intensive investigations on the B-T phase diagram have been performed [12, 76, 77, 74]. The CDW system mainly differs from the SDW one in that it is paramagnetically limited [26, 13, 14], similar to conventional singlet superconductors. The phase diagram, with the magnetic field directed perpendicular to the layers, on which there is to the moment a general agreement [12, 78, 79] is depicted in Fig. 3.6. Here we show data observed in magnetic torque measurements by Christ et al. [12] together with specific heat data from Kovalev et al. [75]. As can be seen, a gradual suppression of the transition temperature with increasing field is observed. Additionally, at $T < 4$ K a hysteresis appears between the up and down field sweeps in the torque [74] that most likely occurs due to a first order transition to another state at high fields. Remarkably, this phase diagram very well resembles the one which was theoretically predicted [28, 13, 14] for a perfectly nested CDW system and is shown in the inset of Fig. 3.6. At small fields, the transition temperature is proposed to decrease

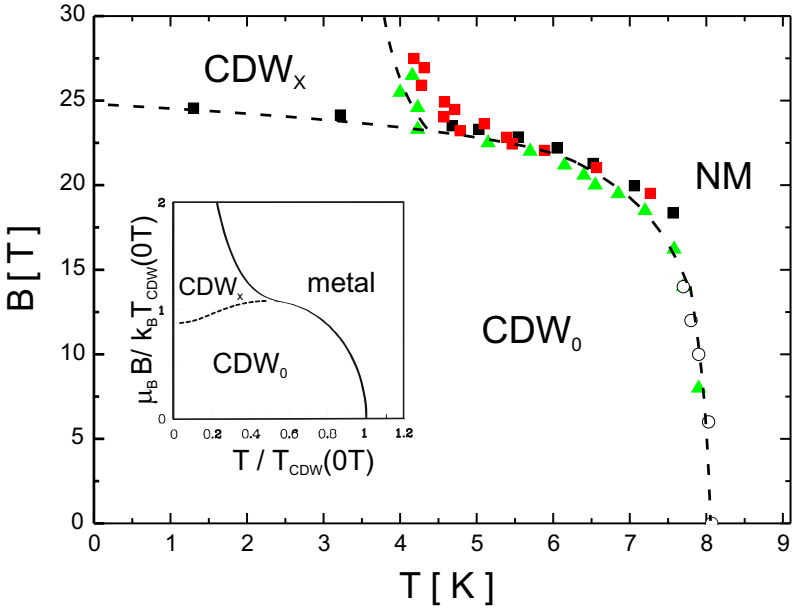

Figure 3.6: B-T phase diagram determined via the magnetic torque [12](solid symbols) and specific heat [75](open symbols). The phase diagram resembles the one proposed theoretically for a perfectly nested CDW$_0$ state by McKenzie [13]and Zanchi et al. [14] that is shown in the inset. At high fields there exists the first example of a modulated CDW$_x$ state.

proportional to B^2 [26]. At the critical field value B_k, which is determined by the zero temperature energy gap of the density wave, the state labeled CDW$_0$ becomes suppressed. CDW$_0$ is the phase with a fixed nesting vector that perfectly nests the Q1D sheets of the Fermi surface at zero field [14]. On crossing B_k there is then the first order transition expected at low temperatures ($T < 0.56T_c$) between the CDW$_0$ and the CDW$_x$ states [27, 26, 13, 28, 29]. The latter is actually a mixed SDW and CDW state with a nesting wave vector expanded along the conducting chains. This high field state is an analog to the Fulde-Ferell-Larkin-Ovchinikov state [80, 81] that is supposed to occur in highly anisotropic clean singlet superconductors, and it is expected to remain present up to much higher fields than the perfectly nested CDW$_0$ state. The whole phase boundary between the normal metallic and the CDW states is of second order [27, 26, 29].

Finally we mention that, besides the strong arguments for a CDW state given within this thesis, two groups collaborating with ours very recently found further evidences. A non-linear current-voltage dependence found by Hamzic et al. [82] was interpreted to be due to a sliding CDW. The latter is known to add an additional

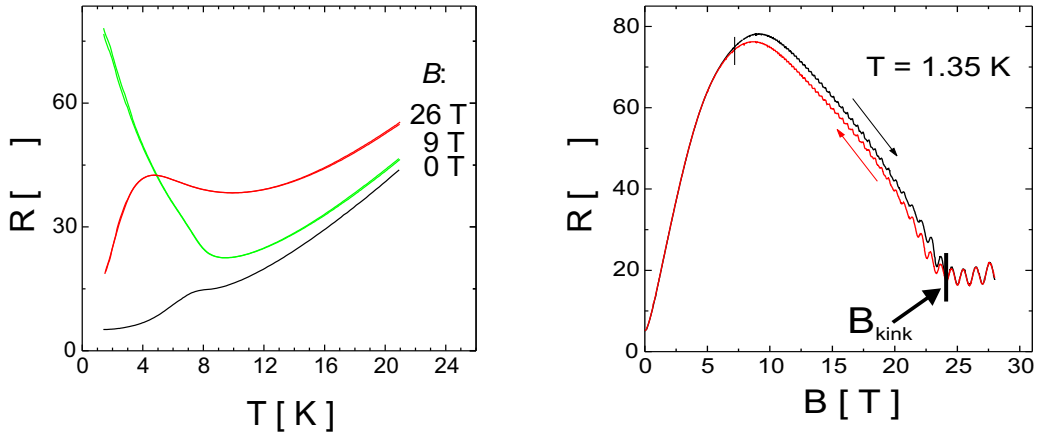

Figure 3.7: Typical field and temperature dependent resistance seen in the title compound. For a detailed description see text.

contribution to the total conductivity. Further, Foury-Leylekian et al. [83] performed the first x-ray measurements at low temperatures that could indeed resolve a crystallographic superstructure within the density wave state, that to the moment may be regarded as the most direct evidence for the existence of a CDW.

Since this work mainly deals with the interlayer magnetoresistance measured under hydrostatic pressure the general features of the interlayer resistance seen within the CDW state at ambient pressure will now be introduced. The magnetic field is directed perpendicular to the conducting **a-c** plane. In Fig. 3.7 the general properties of the field- and temperature-dependent resistance are summarized. At zero field the transition to the CDW state is reflected in a characteristic hump. The system keeps its metallic character , i. e. a decreasing resistance with lowering the temperature, within the CDW state as expected from the remaining ungapped parts on the reconstructed Fermi surface. The most remarkable property of the CDW state is a strong magnetoresistance at fields directed perpendicular to the **a-c** planes. This most probably owes to the motion of the carriers along the open sheets, that for this direction of magnetic field strongly diminishes their net component of the velocity perpendicular to the planes. At $\approx$ 11 T the magnetoresistance reaches a maximum followed by a long field range with a negative slope. At $\approx$ 24 T the decrease of the background resistance in perpendicular field accelerates, followed by

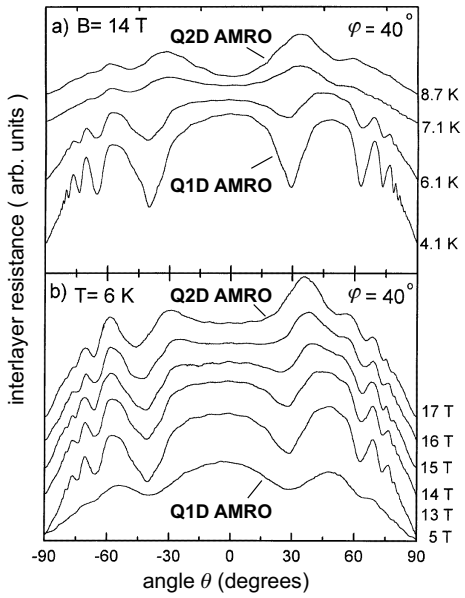

Figure 3.8: AMRO measurements by House et al. [84] at different temperatures and magnetic fields. The curves are offset from each other.

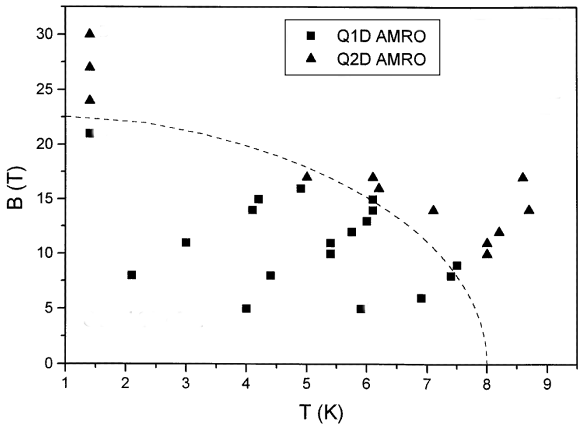

Figure 3.9: Suggested phase diagram due to different AMRO types [84].

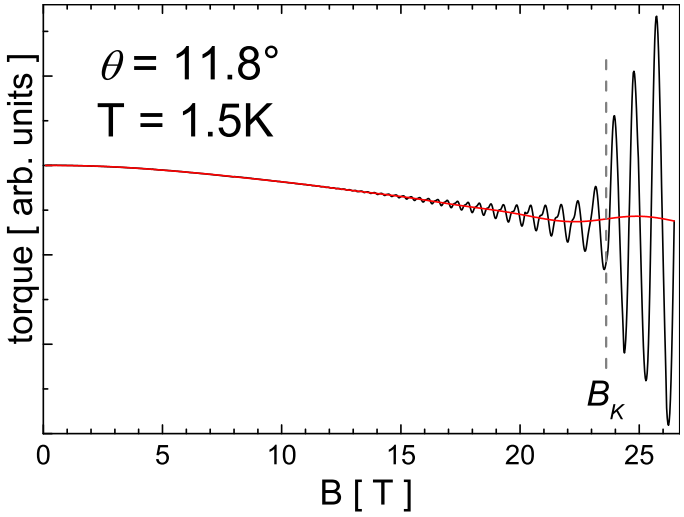

Figure 3.10: Field dependent torque (black curve). The kink transition is directly reflected in a sudden increase of the dHvA oscillation amplitude as well as in a slight change of slope in the non-oscillating torque component (red curve).

a moderate increase that determines the so-called "kink"-transition from the CDW_0 into the modulated CDW_x state. Correspondingly, distinct changes can be seen in the temperature sweeps of the magnetoresistance on entering both CDW states. On sweeping the field up and down there is a hysteresis observed in a wide field range within the CDW_0 state, the origin being still unknown. The negative magnetoresistance above 11 T is thought to occur due to magnetic breakdown between the open trajectories and the small pockets [85], depicted in Fig. 3.5. This means that the electrons again start to circle around the initial cylindrical part of the Fermi surface. The decrease in the background magnetoresistance is thus related to a gradual change of the AMROs from a Q1D to a Q2D character. In Fig. 3.8 results of House et al. are shown [84]. They measured AMROs at different temperatures and fields and could determine an approximate phase transition line separating Q1D AMRO from the Q2D AMRO regions, see Fig. 3.9.

In the magnetic torque, with a magnetic field directed nearly perpendicular to the layers, the transition from the CDW_0 to the CDW_x state is clearly reflected in a change of the slope of the torque background as well as in a sudden enhancement of the dHvA oscillations. An example is depicted in Fig. 3.10.

3.5 Effects of Hydrostatic Pressure

The application of hydrostatic pressure usually results in an overall increase of the molecular orbital overlap. All the transfer integrals therefore can be expected to become enhanced. For a density wave ground state, which emerges due to a strong one-dimensionality of the system, the perfectness of the nesting then mostly depends on the relative changes of the in- and interchain transfer integrals within the conducting planes. If the relative increase of the interchain transfer integral exceeds the inchain one, the sheets on the Fermi surface become stronger warped, therefore giving less perfect nesting conditions. Since a complete suppression of the CDW state under a hydrostatic pressure of only a few kilobar in the present compound has already been suggested by several experimental works [15, 16], it is natural to assume that hydrostatic pressure indeed causes such an enhanced dimensionality of the Q1D band. A suppression of the density wave (in that case, of the SDW) under hydrostatic pressure has also been observed in the (Q1D) SDW ground state of the well known TMTSF based compounds. Remarkably, a simple theoretical consideration involving only the nearest and next-nearest interchain hopping of the carriers

turned out to describe the experimental observations on the SDW under hydrostatic pressure very well [2]. Since a similar theoretical consideration exists for a (Q1D) CDW system in an applied magnetic field [14], a direct comparison of our experimental results with theoretical predictions will be possible. As pointed out in the theoretical background above, one can expect orbital effects of the charge carriers to become important on worsening the nesting conditions of the CDW system.

Concerning the superconducting state existing in many BEDT-TTF based salts, the anisotropy of the electron system also seems to be important. Generally, these superconductors turn out to possess a very strong pressure dependence of the transition temperature, T_c, that amounts to the order of -1 K/kbar. Since T_c was suggested to correlate with the anion layer thickness [9], its strong pressure dependence might be attributed to the strong interlayer compressibility. On the contrary Q1D organic superconductors do show a much weaker pressure dependence of T_c of about an order of magnitude lower. Here the strong lattice stiffening rather than the above lattice pressure effect is thought to be the reason. This means that the change in the phonon spectrum, as for conventional superconductors, leads to a reduced electron-phonon coupling that finally leads to a decrease of T_c.

Chapter 4

Experiment

Within this experimental study resistance and magnetic torque measurements were performed. After explaining these techniques in more detail the realization of the external conditions to which the samples were exposed in this work, namely low temperatures, high magnetic fields and hydrostatic pressure, will be described. This includes new experimental developments which have been done in the frame of this work.

4.1 Measurements

4.1.1 Resistance

To perform transport measurements platinum wires of $\varnothing 10 - 20$ μm were attached to the sample using graphite paste. The sample resistance was measured by the common four probe technique. Two contacts on the sample served to apply the current across the sample, while another two were used to detect the induced voltage. Thus the observed resistance did not contain the additional contact resistance, which was normally about 10-40 Ω at room temperature.[1] The contacts were placed on opposite sides of the sample with the current perpendicular to the highly con-

[1] The interlayer resistance of the sample was typically several kiloohm at room temperature.

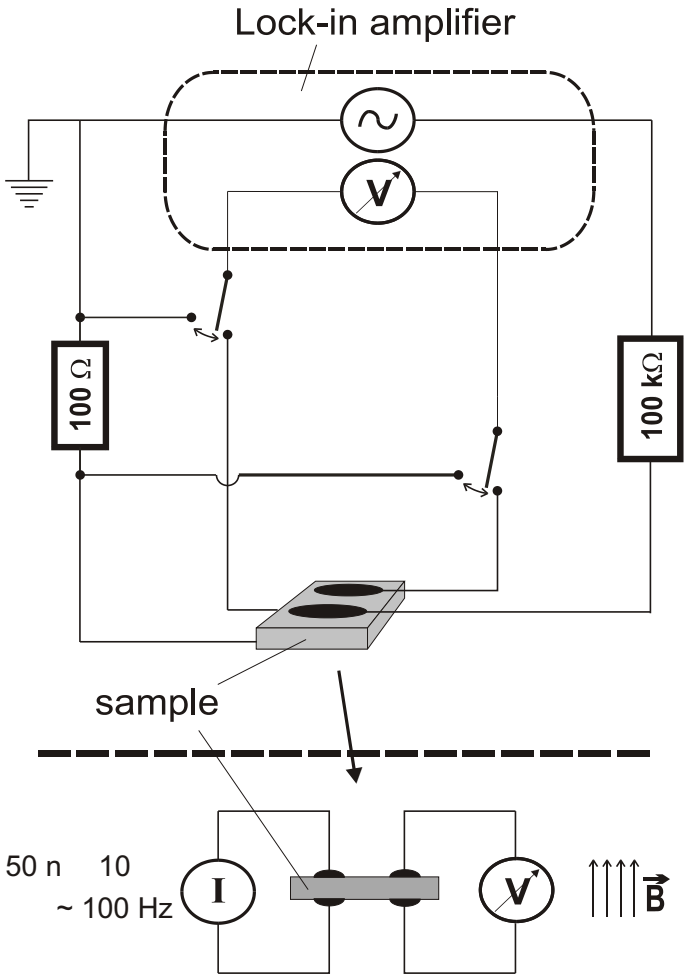

Figure 4.1: Circuit of the four point resistance measurement.

ducting **a-c** plane. We were thus measuring the interplane resistance. The reasons for this are manifold. Firstly, the resistivity in the interplane direction is about 4-5 orders of magnitude bigger than the intraplane resistivity, reflecting the extremely high anisotropy of the electron system. The interlayer resistance can thus be detected much more accurately. Secondly, our single crystals tend to be rather irregular in shape, so that the apparent (measured) intraplane resistivity is actually a combination of all resistivity tensor components. In contrast, the measured interlayer resistance is almost exactly proportional to the interlayer resistivity [86]. Thirdly, the unusual magnetoresistance features (in which we are interested) are more pronounced at the interplane current direction.

A sketch of our measuring circuit is shown in Fig. 4.1. To measure the resistance

an AC current of 0.01 to 10 μA with a frequency of the order of 100 Hz is applied and the voltage is amplified and detected by a highly sensitive lock-in amplifier. The low current value serves to prevent overheating of the sample at low temperatures, and has to be adjusted to the given experimental conditions, e.g. contact resistances and temperature range. To keep the current amplitude constant and stable during the measurement a high resistance (typically 100 kΩ- 1 MΩ) is placed in series. For the adjustment of the current and the phase a reference resistance (of 10-100 Ω) is placed into the circuit. By measuring the AC voltage across this resistance a desired current value can be set.

The absolute sample resistance at low temperatures (with or without a magnetic field) was thus checked to be detected to an accuracy of at least 5 %. The signal-to-noise ratio during our measurements was typically $\gtrsim 10^4$.

4.1.2 Magnetic Torque

A magnetic moment $\mathbf{m}$ placed into an external magnetic field $\mathbf{H}$ experiences a torque $\boldsymbol{\tau}$ in the direction perpendicular to $\mathbf{m}$ and $\mathbf{H}$:

$$\boldsymbol{\tau} = \mathbf{m} \times \mathbf{B}, \tag{4.1}$$

where B is the magnetic induction in the sample, $B = \mu\mu_0 H$. In our compounds we assume $\mu \approx 1$.[2] For a sample with a homogeneous magnetization $\mathbf{M}$ over its volume V the torque then amounts to:

$$\tau = M_\perp BV, \tag{4.2}$$

where $M_\perp$ is the component perpendicular to the field direction. For the measurement of quantum oscillations, using Eq. (2.19) the oscillatory torque may thus be written in terms of the magnetization $\tilde{M}_\parallel$ parallel to the field:

$$\tilde{\tau} = -\frac{1}{F}\frac{\partial F}{\partial \theta} M_\parallel BV. \tag{4.3}$$

The detection of the dHvA oscillations by the torque method obviously needs an anisotropic Fermi surface, $\frac{\partial F}{\partial \theta} \neq 0$. Further, the torque vanishes if the magnetic field is directed along a symmetry axis of the crystal. In such cases either $\frac{\partial F}{\partial \theta} = 0$ or opposite components of the torque cancel each other out. This offers a perfect possibility to align the sample or, in other words, calibrate the offset angle with

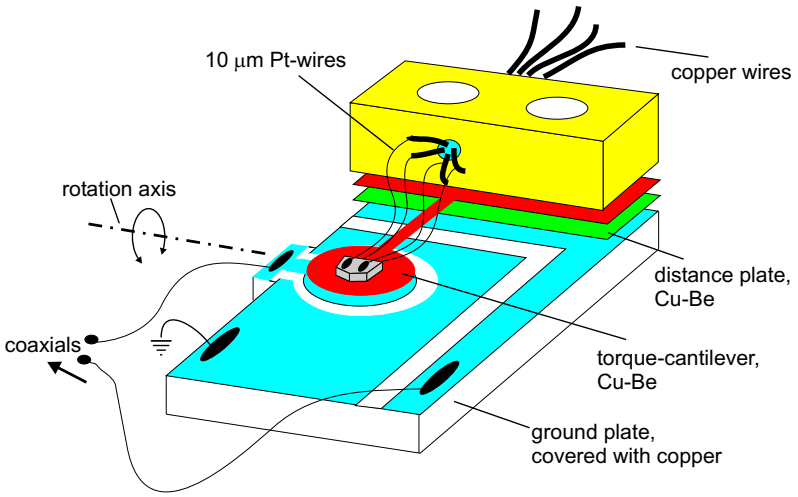

Figure 4.2: Currently used capacitive torquemeter. The sample resistance is measured simultaneously with the torque.

respect to the magnetic field direction. Within our experiment a cantilever beam torquemeter developed by Biberacher and Christ [87] was employed. A sketch of this capacitive torquemeter is shown in Fig. 4.2. One electrode of the capacitor is built by the Cu-Be cantilever itself. The other one is on the ground plate. The cantilever consists of a circular plate of 3 mm diameter and is connected to a rectangular plate by a narrow beam, which is 2.5 mm long and $\approx$ 0.4 mm wide. In order to keep a small distance between both electrodes there is another rectangular Cu-Be plate placed below the cantilever (with a thickness of the order of 50 μm). On the ground plate there are 2 Cu-areas belonging to the electrodes which are separated by another one that is connected to the ground. To avoid the so-called torque interaction during the measurement the changes in the capacitance must be kept rather small, $\Delta C/C < 1\%$, since under such conditions the capacitance change ΔC can be assumed to be proportional to the torque induced by the sample. Thus, depending on the field and angular range of the measurement the thickness of the cantilever had to be chosen between 25 and 50 μm. Both electrodes are connected to co-axial cables and the capacitance was directly read out by a capacitor bridge with a signal-to-noise ratio of typically 10^5. Since we were only interested in relative changes of the torque signal a calibration of the setup was not done.

In order to perform combined torque and resistance measurements, which was always done within this study, the sample had to be additionally contacted by

[2]In this thesis **B** instead of **H** will be taken as a measure of the applied magnetic field

Ø 10 μm platinum wires. Here, care had to be taken that these wires did not contribute an additional force to the sample that would falsify the torque signal. These wires thus have to be as soft and flexible as possible. Therefore, they had to be shortly annealed using a conventional lighter and they were chosen rather long, avoiding current loops in the field direction as good as possible. Hence, the additional contributions from the wires were reduced to a minimum. Since in our measurements only relative changes in the torque signal were of interest, a small additional contribution from the platinum wires, that could still be seen in the background torque signal, did not affect the results presented in this work. This was in a few cases assured in successive measurements of the torque with and without attached platinum wires.

4.2 Low Temperatures

Within this experimental study measurements were performed at temperatures between 20 mK and 300 K. In this rather wide temperature range different cooling techniques have to be used.

To continuously vary the temperature above $\approx$ 1.5 K as well as for magnetic field sweeps at constant $T > 4.2$ K the sample was exposed to a constant ^{4}He gas flow, while the temperature was set by a resistive heater. Magnetic field sweeps at constant T within 1.4-4.2 K were performed in liquid ^{4}He, where the temperature was regulated via the vapour pressure. The same was done using liquid ^{3}He within the range of 0.4-1.4 K. For even lower temperatures a dilution fridge containing a ^{3}He-^{4}He mixture has to be used. The one used in this study was built up by K. Neumaier at the WMI. Its cooling power of $\approx$ 25 μW at 100 mK allowed a pressure cell to be cooled down to 20 mK. A picture of this system is shown in the appendix.

To monitor the temperature different resistive sensors were used:

- a self-calibrated *Cernox* sensor in the range 1.4-300 K,
- a commercially calibrated *Cernox* sensor in the range 0.3-300 K,
- a RuO_2 sensor, calibrated by K. Neumaier, in the range 20-500 mK.

4.3 High Magnetic Fields

The creation of magnetic fields is based on the fact, that a current, flowing in one direction, is surrounded by a magnetic field, that is the law of Biot-Savart. High steady fields can thus be achieved inside coils wound from highly conducting materials. Depending on the geometry and the arrangement of several coils the high field can be made homogeneous in a finite volume. Two kinds of magnets which are commonly used to apply high steady fields are briefly presented in the following parts.

4.3.1 Superconducting Magnets

To apply a steady magnetic field up to 17 T, a superconducting magnet from *Cryogenics* was used in the Walther-Meissner-Institute. It consists of two coils, mounted co-axially on a common base. The inner coil is wound from multifilamentary Nb_3Sn, the outer from NbTi. Both solenoids are coupled in series. Due to the finite critical current and field of both superconducting materials, the achievable magnetic field in the centre of the magnet is limited to 15 T when the latter is kept at 4.2 K inside the ^{4}He main bath. On cooling the coils down to the lambda point of ^{4}He, 2.17 K, fields of up to 17 T may be reached.

4.3.2 Resistive Magnets

Since in a superconducting magnet the reachable field is limited by the critical field and current, higher fields (currently $\gtrsim$ 21 T) can only be created by the use of resistive magnets. Here, however, the technical and financial efforts become much higher, in contrast to superconducting magnets, which can be run almost powerless apart from cooling the whole system to low temperatures. Resistive magnets are mostly made with copper as the conducting material to keep the resistance as low as possible. The Joule heat produced in the coil by the electrical power has to be drawn off by deionized water, which flows under high pressure through holes placed within the conducting material.

High field resistive magnets can be separated into two kinds: First is the so-called

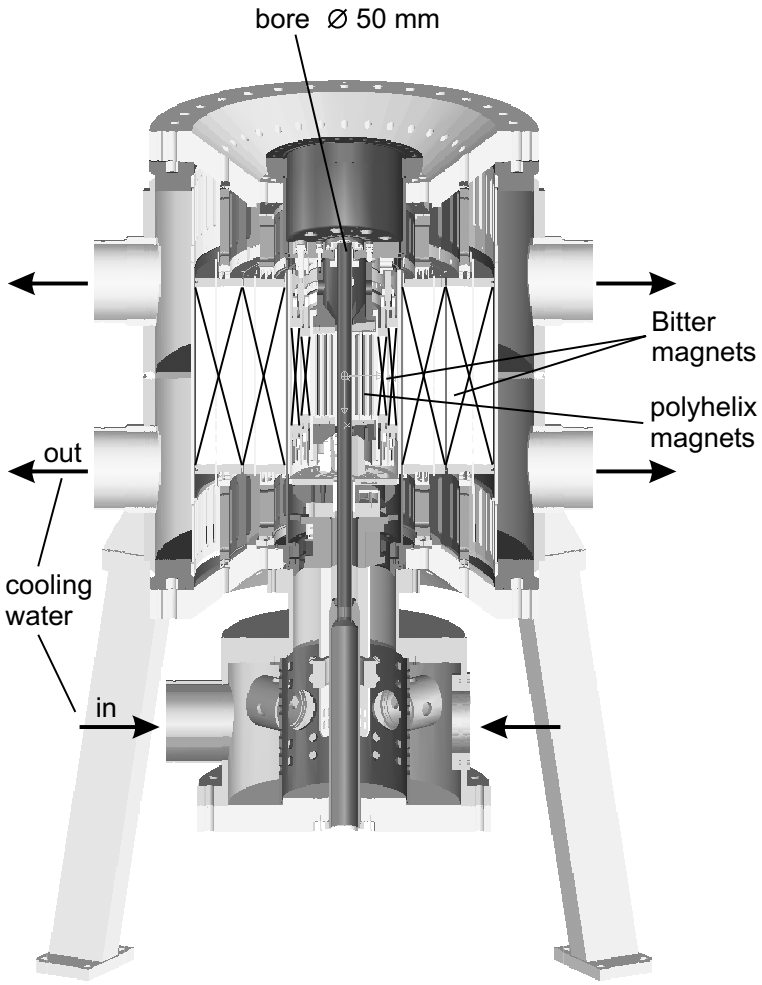

Figure 4.3: Sketch of a 30 Tesla magnet used in the high field lab in Grenoble.

Bitter magnet (named after the inventor). Copper discs are layered on each other with an insulating material in between except a slice of about 20°. By pressing them together with a strong force a sort of coil is built with a radial current density that is inversely proportional to the distance from the coil axis. To prevent the system from "melting", deionized water flows through holes, drilled parallel to the coil axis through the copper discs.

Another resistive magnet is the polyhelix magnet. It consists of several copper coils fitted coaxially into each other. The advantage in comparison to the Bitter magnet is, that the current density can be regulated radial to the field. In this work

high field (> 17 T) experiments were made in the High Magnetic Field Laboratory (HMFL) in Grenoble with a resistive magnet. Here, two Bitter magnets are placed around a polyhelix magnet, Fig. 4.3. This configuration allows to reach a maximum steady field of 30 T at a current of 10 kA and a water flow of 1000 m^3/h, while applying the power of 20 MW.

4.4 Hydrostatic Pressure

In this work two different pressure techniques have been applied, one using helium and the other silicon oil as a pressure medium. Since the former technique was further tested and improved for the use at low temperatures in the frame of this work, this will be described in more detail.

4.4.1 ^{4}He-pressure Apparatus

In Fig. 4.4 the whole ^{4}He pressure setup is sketched. It can be roughly separated into two stages. One, where the pressure never exceeds 3 kbar and another, where pressures up to 10 kbar (= 1 GPa) can be reached. ^{4}He comes from the gas bottle (P=180 bar) into the completely pumped system and is filtered in a nitrogen trap. This prevents blockages in the lines during pressurisation, especially at low temperatures inside the cryostat. In the first stage, a membrane compressor applies up to 3 kbar to the whole pressure system. After the desired pressure is reached the valve between the first and second stage is closed. Oil pressure then drives up a piston in an amplifier that reduces the volume of the second stage. The pressure applied from the first stage can thus be multiplied by a factor of 4. The high pressure is then transferred via a 4 m long Cu-Be capillary to the pressure cell inside the cryostat. Except this low-temperature part, all parts of the system were bought from the company "Nova Swiss". To monitor the pressure, commercial (membrane) pressure sensors are placed in each stage, one measuring up to 3 kbar and another up to 10 kbar. In order to prevent damages of the compressor and the pressure sensor in the first stage, a rupture disk is located there which would immediately break if the pressure exceeds 3 kbar. For safety reasons, in the case of an explosive decompression of the system, a steel rope is fixed to the Cu-Be tube and the whole system is surrounded with thick plastic shields. The pressure system was successfully tested

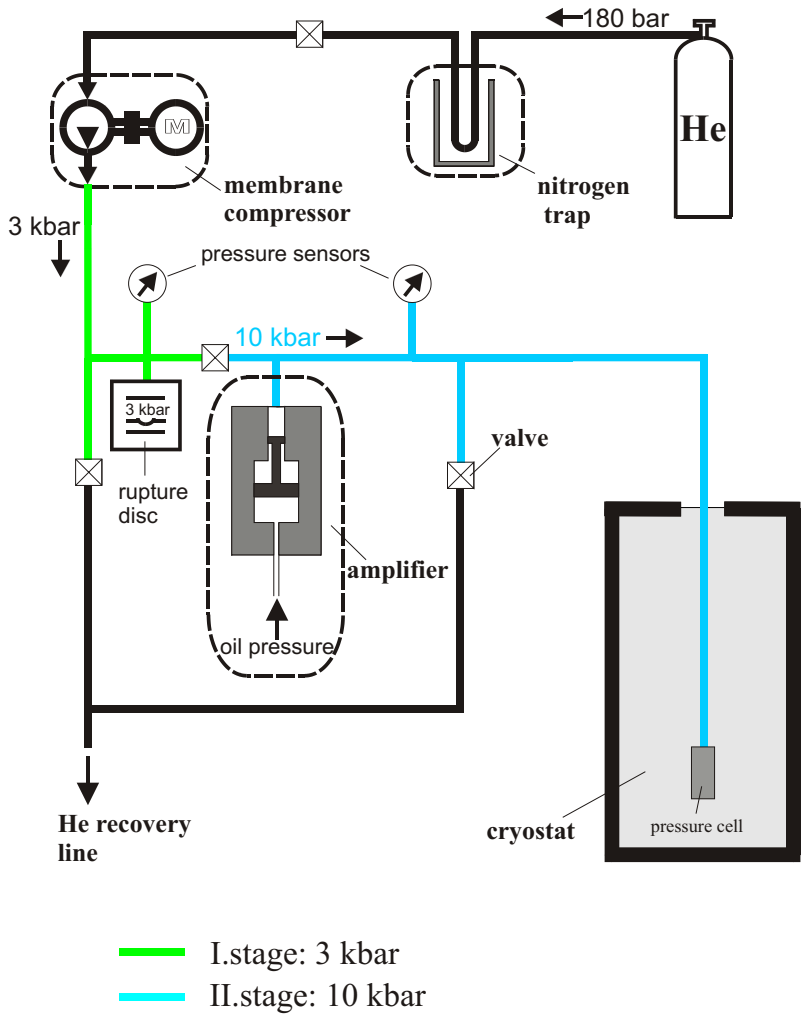

Figure 4.4: Sketch of the ^{4}He pressure apparatus.

at room temperature up to 10 kbar.

The advantage of this pressure apparatus is, that the pressure can be changed at low temperatures, in contrary to other pressure techniques such as the clamp cell (see below). This is quite important for such fragile compounds like organic metals, which are known to be very sensitive to thermal cycling. Another advantage is the easy measuring of the pressure value, that allows to apply even low pressures (< 1 kbar) with a very high accuracy.

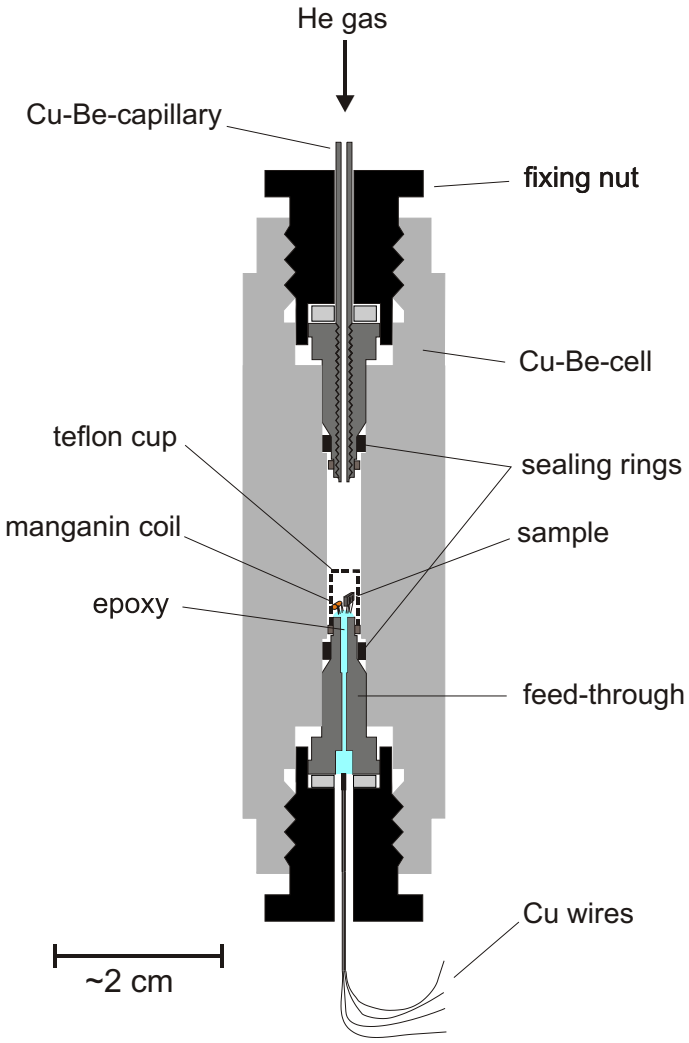

Figure 4.5: ^{4}He-pressure cell at the end of the capillary.

4.4.2 ^{4}He-Pressure Cell

The ^{4}He pressure cell is sketched in Fig. 4.5. Helium comes through the capillary with the inner diameter of 0.3 mm into the sample chamber. The upper Cu-Be feedthrough is screwed on the capillary and soldered all along the thread. To provide sufficient tightness the sealing rings are made out of brass and covered with a thin layer of lead. Copper wires are embedded in 'Stycast'-epoxy inside the lower feedthrough, thus allowing electrical measurements inside the cell. Care has to be taken on filling the feedthrough with epoxy that no cavities remain within the chan-

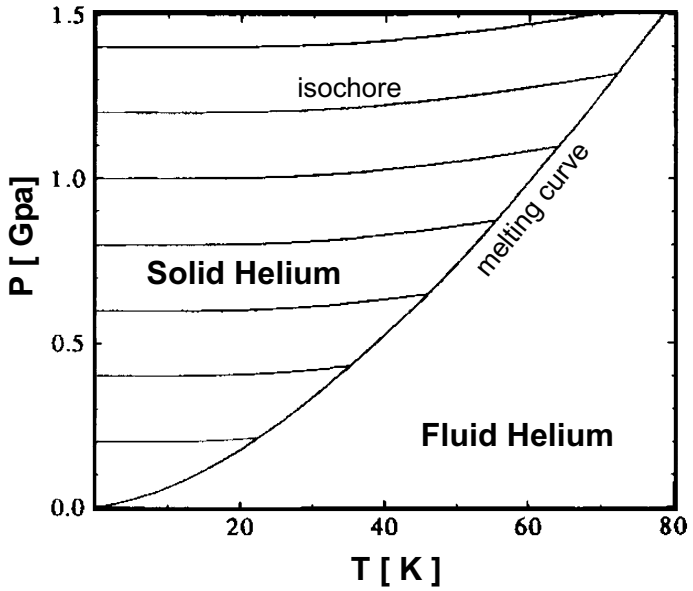

Figure 4.6: P-T phase diagram of ^{4}He [88].

nel. This is first due to the possibility of a compression of the cavity that may cause the wires to break and second due to liquid (or superfluid) Helium entering these cavities during the experiment. On warming above the condensation point, a small bomb may be created, shooting a part of the epoxy out of the channel and cutting all wires.

On the top of the feedthrough annealed 20 μm platinum wires are soldered to the copper wires and 4 of them are contacted to the sample with graphite paste. To monitor the pressure changes inside the cell (when the ^{4}He is already solid) a manganin coil (see section 4.4.5), which is also contacted by 4 platinum wires, is placed next to the sample.

4.4.3 Helium as a Pressure Medium

Helium is the last element to become solid at a given pressure ($\gtrsim$ 25 bar) with lowering the temperature. The melting curve of ^{4}He is illustrated in a P-T phase diagram in Fig. 4.6. In view of this, liquid (or gaseous) ^{4}He as a pressure medium provides a truly hydrostatic environment in the widest possible temperature and pressure range in comparison with any other element.

In the solid state additional shear strains occur. However, there exist experimental results which highly suggest that these shear stresses are reduced to a minimum for solid ^{4}He in comparison to any other crystalline element [89] [88]. Thus ^{4}He as a solid should also provide quite good hydrostatic conditions.

A disadvantage of ^{4}He as a pressure medium is the difficulty to maintain leak-tight seals. This turned out to be the most time consuming problem during our experiments. Additionally, there is the possibility of an explosive decompression of the system, as already mentioned, which requires certain safety precautions.

Pressure is applied in the liquid state of ^{4}He. After the desired pressure is reached, the cell is cooled down and at a certain temperature ^{4}He becomes solid. At this point great care has to be taken to minimize shear strains during solidification. For example, if ^{4}He is frozen inside the capillary before the solidification level has reached the top of the sample chamber, the pressure inside the cell will drop with further cooling, causing already frozen ^{4}He to expand and thus inducing additional shear strains. Therefore the solidification level should slowly move *from the bottom to the top* of the sample chamber. This means, that the temperature gradient along the cell should be kept as high as possible and the temperature at the capillary should always be higher than that at the top of the cell. A careless treatment of this point in our first experiments led to a pressure drop inside the cell during solidification which at 5 kbar became so big that the frozen ^{4}He inside the capillary shot into the sample chamber and completely destroyed (actually powdered) the sample. With a rearranged heater distribution along the cell and capillary this pressure loss could be eliminated, at least at $P \lesssim 3$ kbar. Fig. 4.7 shows the heater arrangement on the

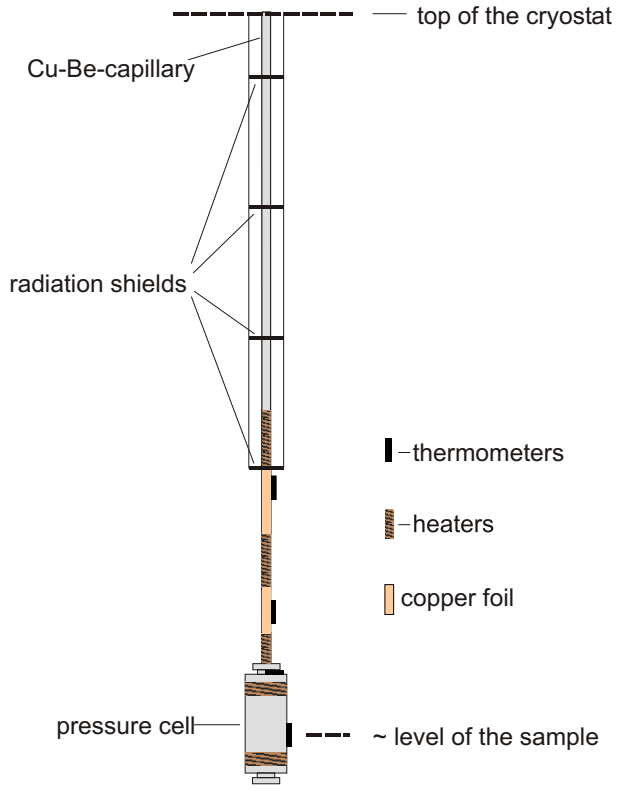

Figure 4.7: Currently used ^{4}He-pressure insert.

^{4}He pressure insert, as it is currently used. The cooling of the insert is provided by cold ^{4}He gas coming from the bottom of the cryostat. Four heaters are placed along the axis to provide a temperature gradient as good as possible, the latter being monitored by four thermometers. The heat is applied resistively by manganin wires, wound around the cell and capillary. Additionally, a copper foil is wound around the capillary that turned out to improve the heat distribution and to prevent possible "cold spots" on the capillary. However, at pressures above 3 kbar, it still remains difficult to avoid pressure gradients inside the cell during solidification, that makes it difficult to cool down without a displacement of the sample. Whether these pressure oscillations are still caused by a wrong temperature distribution is not clear at the moment. Another reason could be, that the latent heat, released during solidification, at high pressures becomes too big to be immediately carried away. This might result in already frozen ^{4}He to become liquid again causing pressure oscillations inside the cell. To try to eliminate this problem, a teflon cup was placed around the sample in order to reduce the sample space, that could result in smaller pressure gradients. Up to now, tests at 4 kbar were successful, so that it should be possible to apply even higher pressures.

4.4.4 The Clamp Cell

The most conventional technique to apply (quasi-) hydrostatic pressure up to ∼15 kbar is a Cu-Be clamp cell with a liquid pressure medium. A sketch of the cell used in our experiments is given in Fig. 4.8. The preparation of the feedthrough as well as the electrical contacts are the same as described above for the ^{4}He-pressure cell. A cylindrical teflon cup filled with the silicon oil "GKZh", which serves as the pressure medium, is put around the sample. In order to seal the pressure space, a Cu-Be washer is placed between the teflon cup and the feedthrough. GKZh solidifies at about 150-220 K (depending on pressure), with a rather small volume effect, into an amorphous structure, therefore providing rather isotropic pressure at low temperatures. Due to the low compressibility of the oil the teflon cup and the pressure channel can be rather short. To apply pressure, a piston, placed above the teflon cup, is pushed down into the sample space and the pressure is kept by fixing the nut. Since the middle of the channel became a little bit wider after several measurements under pressure, another Cu-Be sealing ring was put on the top of the cup. This is to prevent the teflon cup to "flow" between the piston and the channel wall during pressurisation. With this technique, pressures up to 15 kbar can be

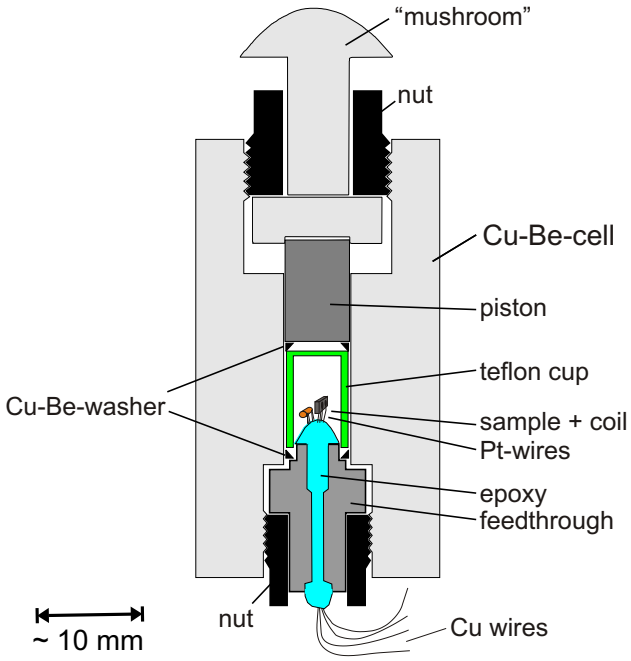

Figure 4.8: The liquid medium clamp cell.

applied without a problem. To measure the pressure, a manganin coil, calibrated with the ^{4}He pressure station, was placed next to the sample. To cool a pressurized sample down to the lowest possible temperature the cell has been mounted on a dilution refrigerator. Here, problems appeared on applying high magnetic fields. Besides the expected eddy current heating, while sweeping the field, the cell showed a considerable demagnetization effect on ramping the field down. The latter cooling mechanism could be reduced with a new cell that was made out of very pure Cu-Be containing less magnetic impurities. However, these two parasitic effects made it impossible to make magnetic field sweeps (in the tesla range) and especially to study the hysteretic magnetoresistance between raising and falling fields below $T = 100$ mK.

4.4.5 Pressure Determination

The pressure inside both cells (described above), was monitored by a manganin coil. It was wound from a 50 μm manganin wire and the coil resistance took the value of a few Ω. The resistance of manganin is known to depend linearly on pressure. For a

better reproducibility of the pressure dependence the coil first has to be annealed for one day at 140°C and then must be pressurized to the highest pressure of the desired measurable pressure range. The commercial pressure sensor of the ^{4}He pressure apparatus was then used to calibrate the coil resistance. Coinciding with results from other groups [90,91], the resistance at room temperature was found to increase nearly linearly with pressure by about 0.24 %/kbar. Not coinciding with previous results was the appearance of a considerable hysteresis in the resistance in up and down sweeps of the pressure, which became bigger at applying higher pressures. At applying 8 kbar the maximum deviation of up and down sweeps amounted to more than 100 bar. Yamamoto et al. [90] reported, that a hysteresis can occur due to certain insulation materials covering the manganin wire, but with a maximum deviation of 20 bar. This is far too small to explain our results, since Yamamoto et al. worked at even higher pressures. The hysteresis was also observed at low temperatures and thus gave an additional error in the pressure estimation. The pressure dependence of the resistance, however, kept to be nearly the same down to low temperatures. In the ^{4}He pressure cell the error in the pressure estimation in this work amounts to ± 50 bar. Since in the clamp cell the pressure had to be changed at room temperature and the low-temperature resistance of manganin slightly changes after warming up to room temperature, the error in the pressure estimation became bigger, with a maximum deviation of ±150 bar.

4.5 Two-Axes Rotation

In order to perform AMRO experiments under hydrostatic pressure a new ^{3}He double axes rotation insert for the use in the high magnetic field lab in Grenoble as well as in the WMI has been designed. An explosion-sketch of the lower part of the insert is shown in Fig. 4.9. The rotation is provided via two worm gear units, an outer and an inner part. A small pressure cell, of approximately half the size of the one shown above, is fixed inside the inner worm wheel. The inner rotation therefore serves to set the angular position of the cylindrical cell. The outer worm gear rotates the whole inner part, setting the angle θ between the cell axis and the magnetic field direction. A sample within the cell can thus take any possible position with respect to the magnetic field. While the outer worm axis is directly linked to the top of the insert the inner gear must be disconnected during the measurement. Therefore, to change the angular position of the cell within the inner rotation unit, the inner

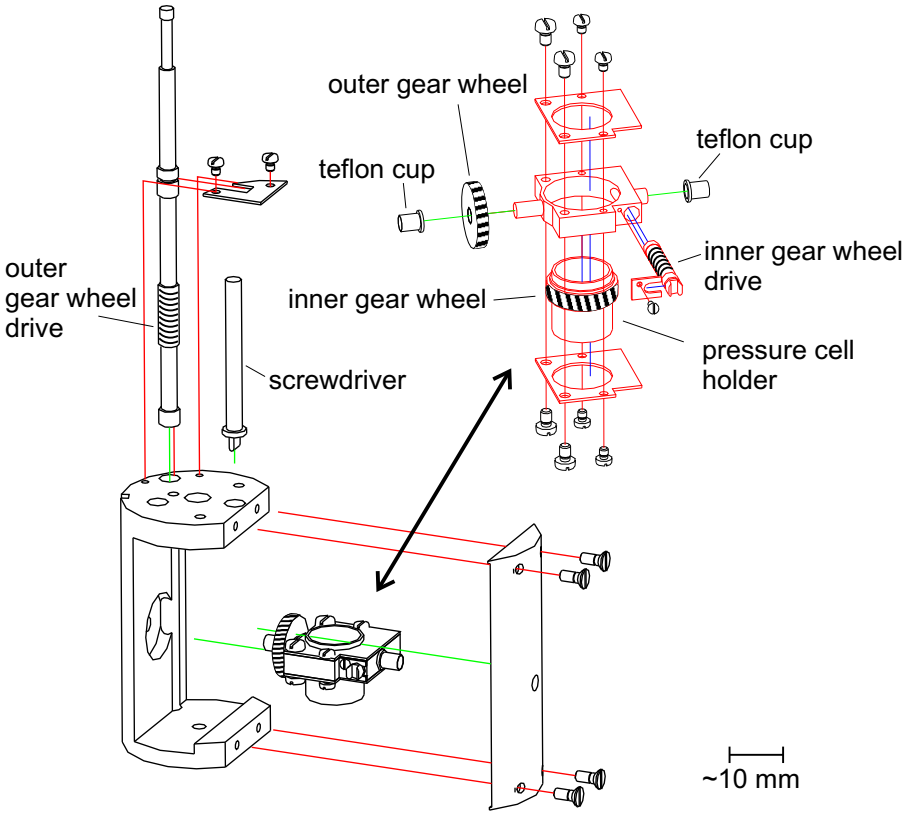

Figure 4.9: Self designed in-situ two-axes rotation unit allowing a small pressure cell to take any position with respect to the magnetic field.

worm axis has to be put to the vertical direction (by changing the angle θ) and a screwdriver, that can be pushed down, has to "catch" the slit on top of the inner worm drive. Thus, by putting a sample inside the pressure cell with the interlayer direction parallel to the cell axis this rotation unit is very suitable to perform AMRO measurements. To diminish the heat production during the steady rotation of the outer gear, the metal to metal friction on the suspension points is avoided by the use of additional teflon cups placed in between. All the other parts in Fig. 4.9 are made out of brass. The accuracy to which both angles can be set with this setup amounts to $< 0.05°$.

Since the whole insert is designed for the use in 30 T magnets, which possess enormous stray fields, it is clear that the use of any kind of magnetic material is not very suggestive. Therefore the driving force on the azimuthal rotation axis is given by a piezo-electric motor. Due to a limited speed range of the latter an additional gear is placed on the top of the insert. The gear reduction can be set over three

orders of magnitude to 10 different values. The sweeping rate of the sample rotation can thus be continuously changed in a wide range of $\approx 0.003 - 10°$/sec. Since a steady rotation of the sample always causes heat induced by the friction, there will be a low temperature limit depending on the rotation speed. With this setup the lowest achievable temperature at a reasonable[3] sweeping rate of 0.1-0.15°/sec turned out to be 0.7 K.

4.6 Sample Preparation and Treatment

The typical dimensions of the samples amounted to about $0.5\times0.5\times0.1$ mm^3 with a corresponding mass of ≈ 75 μg. As a matter of fact the samples appear to be mostly as-grown bi-crystals. This, however, falsifies the measurements in magnetic field, since we know that our measurements strongly depend on the exact field orientation. Therefore most of the samples had to be ground in order to get perfect single crystals. To do this, the samples were embedded into a (afterwards solvable) glue, allowing a part of the sample to be ground off with a conventional disk-grinder. This method of preparing single crystals has turned out to be quite successful, in that the quality of the samples was found not to suffer. This can be seen, for example, from the amplitudes of the quantum oscillations. Actually, this is rather surprising since the fragile samples are otherwise known to be very sensitive to the light and also to thermal cyclings due to the easy formation of micro-cracks. Organic metals generally should be kept in the dark and the cooling and heating rates during our measurements were always checked not to exceed 3 K/min.

[3]here, "reasonable" is linked to the strongly limited magnet time in the high field lab in Grenoble.

Chapter 5

Results and Discussion

5.1 The CDW Ground State under Hydrostatic Pressure

5.1.1 Zero-Field Transition

The transition from the normal metallic state to the density wave state at ambient pressure is manifested in a characteristic hump in the zero-field resistance. Within the density wave state the resistance keeps a metallic behaviour, i.e. it decreases with lowering the temperature. On cooling down from room temperature the interlayer resistance of α-(BEDT-TTF)$_2$KHG(SCN)$_4$ thus shows a steady decrease. The residual resistance ratio between 1.4 K and room temperature in our measurements was typically in between 50-200. This value is commonly taken as a measure of the sample quality; i.e. a higher ratio determines a higher quality.

In Fig. 5.1 we plot the interlayer resistance, measured on the same sample at different hydrostatic pressures at zero magnetic field. In the normal metallic state the resistivity shows a strong negative pressure dependence of $\frac{1}{\rho} \cdot \frac{\partial \rho}{\partial P} \approx 10^{-3}\mathrm{MPa}^{-1}$. This is about 2 orders of magnitude larger than observed in conventional metals like e.g. copper. With increasing pressure the hump moves down in temperature, becoming less pronounced and at 2.3 kbar no sign of the transition is seen any more. Obviously, the density wave state becomes suppressed under hydrostatic pressure, which coincides with the results from other groups [15, 16]. As a characteristic density wave transition temperature T_p we take here a minimum in the derivative (see inset and vertical lines in Fig. 5.1) since this point at ambient pressure coincides best with specific heat measurements [75].

These observations under hydrostatic pressure are easily understood by considering the overlap of the molecular orbitals. With pressure the small overlap across the layers increases rather strong so that an enhanced conductivity should be expected. Furthermore, the transfer integrals between the conducting chains within the layer also do increase, the relative enhancement being very likely stronger than in the in-chain direction. Altogether we thus expect the electron system, and in particular the Q1D part of the Fermi surface, to become less anisotropic. This in turn explains the suppression of the density wave state. In Fig. 5.2 we plot the transition temperatures extracted from Fig. 5.1 against pressure. The data is compared with the results from Schegolev et al. [94] obtained on the Tl-salt of this family of

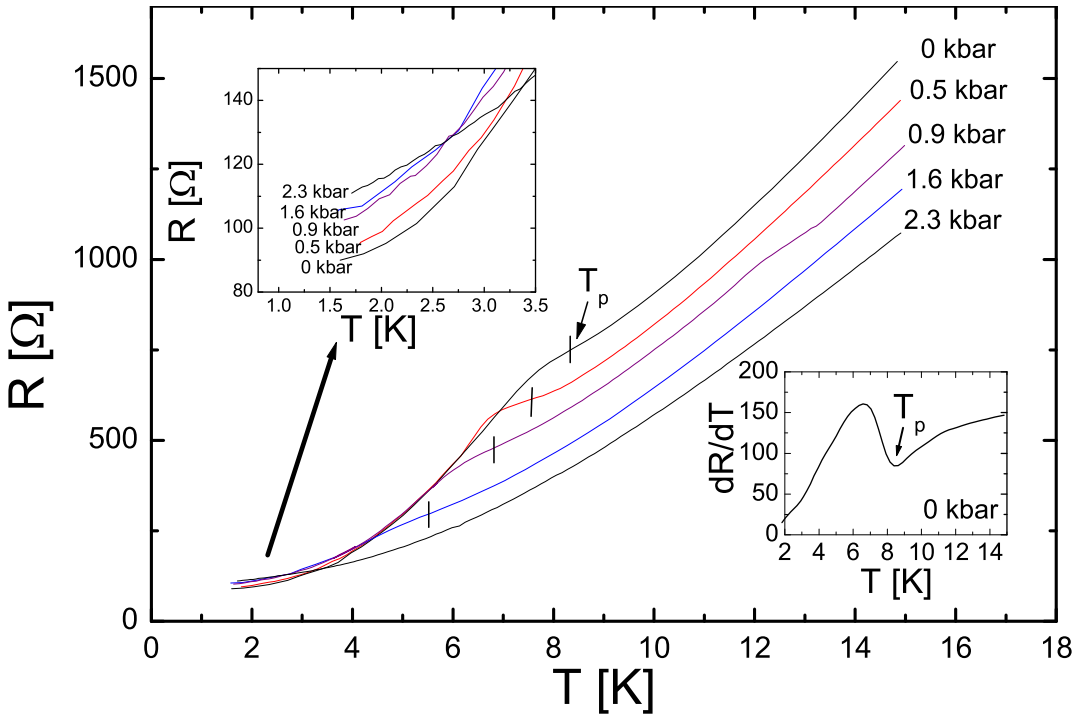

Figure 5.1: Zero-field resistance measured at different pressures [92, 93]. The upper left inset shows the enlarged low temperature part of the curves. The lower right inset shows the determination of the CDW transition temperature from a minimum seen in the derivative. The extracted transition temperatures are marked by vertical lines. The apparent increase of the resistance at $\simeq$ 12 K and 900 bar is due to a slight pressure drop within the cell during the solidification of ^{4}He

organic conductors possessing a slightly higher density wave transition temperature (T_p =9 K) at ambient pressure. Both compounds show similar results. In the K-salt T_p at 1.6 kbar decreased to $\approx 65\%$ of the ambient pressure value.

An interesting observation is shown in the upper left inset of Fig. 5.1. Within the density wave state the resistance, at low temperatures, shows an inverse pressure dependence. It *increases* with pressure. Together with the facts that (i) within the normal metallic (NM) state the pressure dependence of the resistance seems to be temperature independent and that (ii) the NM state at 2.3 kbar persists to lower temperatures, we then conclude that the resistance within the density wave state is *lower* than the expected one in the NM state would be at the same temperature. A lower resistance, however, is normally associated either with an increase of the number of charge carriers contributing to the current, or with a longer carrier life time, i.e. lower scattering rate or with an increase of their velocity. Since a part of

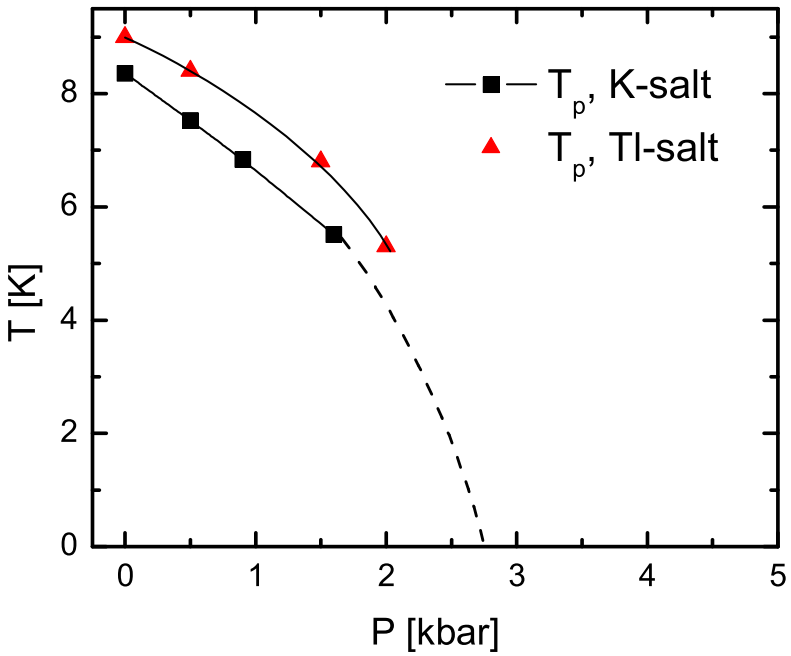

Figure 5.2: Extracted transition temperatures vs. pressure. The data are compared with the results from Schegolev et al. on the Tl-compound [94]. The dashed line is a guide for the eye.

the carriers become gapped in the density wave state a decrease of the resistance is exactly the opposite from what is expected. An easy explanation may come from the fact that the scattering time is to first approximation inversely proportional to the number of states to which the carriers may scatter. In a naive picture the scattering time of the Q2D carriers increases within the CDW state, since the density of states on the Q1D part of the Fermi surface vanishes. If the Q1D part does not contribute too much to the total interlayer conductivity in the normal metallic state, the resistance would then indeed decrease within the CDW state. Moreover, there can be a collective motion of the CDW. This so-called sliding density wave is known to exist in CDW systems giving an additional contribution to the conductivity [19]. Which of the mechanisms leads to this decrease of the resistance cannot be judged from our data and to the moment remains an open question. However, this inverse pressure dependence of the interlayer resistance we take as an additional property of the present CDW state. Above the critical pressure one thus expects the pressure dependence of the resistance at low temperatures to become again negative.

Here, we want to emphasize the advantage of the ^{4}He-pressure apparatus utilized

in the measurements presented in this section. Since we do not have to warm up to room temperature to change pressure but only above the ^{4}He-solidification point, at the given pressure, it is possible to resolve the small inverse pressure dependence of the resistance. Organic metals are known to be very sensitive to thermal cycling. This means that by warming up to room temperature and cooling down again the crystal quality suffers, leading to a smaller residual resistance ratio. Applying pressure with the clamp cell technique thus makes it impossible to study small pressure-induced changes of the resistance at low temperatures. Further, the exact application of low pressures, that had to be done in this section, is much easier to achieve with the ^{4}He-pressure technique.

Coming back to the suppression of the density wave, we expect the increase of dimensionality of the Q1D band to be describable by the model dispersion relation introduced in sec. 2.1.1 [2]:

$$\epsilon_{\mathbf{k}} = \hbar v_F(\mid k_a \mid -k_F) - 2t_c \cos(k_c c) - 2t'_c \cos(2k_c c) \tag{5.1}$$

where t'_c, the effective next nearest neighbor hopping, parameterizes the imperfect nesting. The dispersion in the b*-direction, i.e. perpendicular to the layers, is considered to be small enough so that its changes under pressure do not affect the nesting conditions. Therefore it is usually neglected in theoretical investigations [2].

Within such a model of the dispersion relation the density-wave transition temperature T_p was shown [95,30] to depend on t'_c as sketched in Fig. 5.3. Actually, this plot reflects the BCS type gap equation of superconductors if T_p is replaced by the superconducting energy gap Δ and t'_c by temperature. At $t'_c = 0$ the system is perfectly nested. With increasing t'_c only a small part of the Fermi surface keeps perfect nesting conditions and the effective gap of the density wave at zero temperature decreases. This leads to the decrease of the density wave transition temperature. In Fig. 5.4 the energy bands along the k_c directions

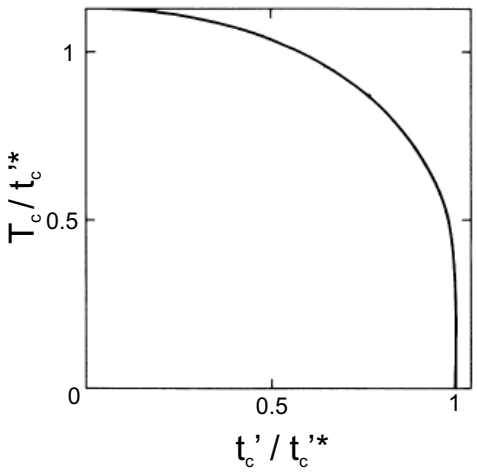

Figure 5.3: Proposed dependence of the density wave transition temperature on the effective next nearest interchain transfer integral t'_c of a Q1D electron system [30].

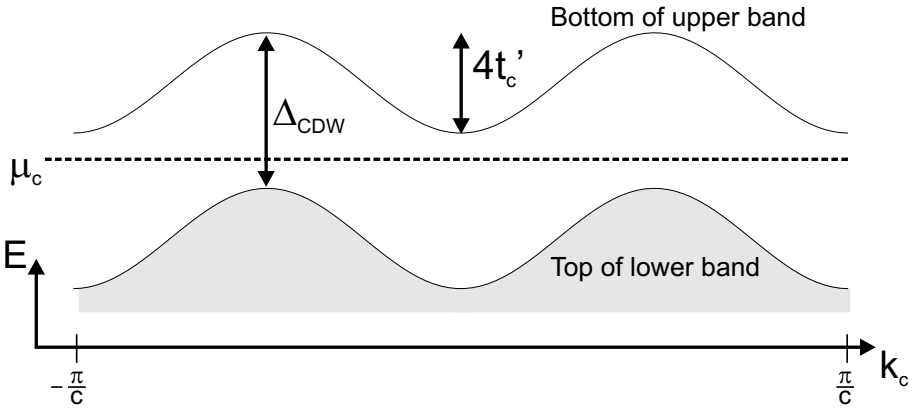

Figure 5.4: Energy dispersion of the Q1D part of the electron system along the k_c-axis within the CDW state.

are sketched. The effective density wave gap is given by $\Delta_{\mathrm{CDW,eff}} = \Delta_{\mathrm{CDW}} - 4t'_c$. At $t'_c = t'^*_c$ (i.e. at $t'_c \approx k_B T_p(t'_c = 0)$ [95]) this effective gap becomes zero and there is no more energy gain of the system by forming a density wave [96, 2]. Up to the critical value t'^*_c all carriers on the Q1D part of the Fermi surface are considered to be completely gapped within the density wave state [2].

Montambaux [30] proposed t'_c to depend linearly on pressure and indeed the results of Biskup et al. [97] showed that this is approximately fulfilled, within the experimental error, in the quasi-one-dimensional organic SDW compound $(TMTSF)_2PF_6$. We therefore also assume a linear pressure dependence of t'_c in the present compound and to the moment neglect an impact of the Q2D part of the Fermi surface on T_p. Two conclusions can thus be made by the comparison of Fig. 5.3 with our data, Fig. 5.2. First, due to the strong change of T_p already at low pressures, we expect t'_c/t'^*_c to be considerably higher than zero already at ambient pressure. Second, the critical pressure corresponding to t'^*_c is likely below 3 kbar. Since we do not see any clear transition at 2.3 kbar it is hard to judge if the density wave state is already completely suppressed or not. The suggestion that the density wave state is already completely suppressed at P $<$ 3 kbar is in contradiction to the proposals of Hanasaki et al. [16] and Brooks et al. [15] who both claimed a higher critical pressure P_0, 5 kbar and 4 kbar, respectively.

5.1.2 Magnetoresistance

Determination of *B-T* Phase Lines via Kohler's Rule

All the data presented in this chapter were measured in a magnetic field applied perpendicular to the conducting layers. Fig. 5.5 shows typical temperature sweeps of the magnetoresistance taken at several constant fields at ambient pressure and at ^{4}He-pressure of 1.6 kbar. The CDW state is characterized by its strong magnetoresistance most probably emerging due to carriers running along the open sheets of the reconstructed Fermi surface. While a general suppression of T_p with pressure is seen in Fig. 5.5, one can imagine that an exact determination of transition points from these curves is not straightforward. Different criteria for extracting transition points has led to various kinds of suggested B-T phase diagrams and therefore to different proposals concerning the nature of the low temperature ground state [76, 77, 98].

In this work we give arguments for a reasonable estimation of the phase diagram via Kohler's rule, a similarity law for the magnetoresistance (see section 2.4):

$$\frac{R_B(T) - R_0(T)}{R_0(T)} = F(\frac{B}{R_0(T)}). \tag{5.2}$$

It is not obvious that BEDT-TTF based metals, possessing such anisotropic electron systems, should obey Kohler's rule. However, this rule has already been found to work well in other organic systems with a metallic state at low temperatures [99,100], showing that it might also be applicable to the title compound. So-called Kohler plots (i.e. magnetoresistance vs. the scaled zero-field conductivity) of the curves in Fig. 5.5 are depicted in Fig. 5.6. The temperature in each curve decreases from the left to the right. It is seen that the high temperature parts of the curves follow one general function, in accordance with Kohler's rule. We therefore suggest the rule to be valid in the NM state of our compound at the given orientation and range of magnetic field. At lower temperatures all the curves start to diverge dramatically that is in line with an earlier report on a strong violation of Kohler's rule in the CDW state of the title compound [101]. We therefore ascribe the deviation from Kohler's rule to the transition from the NM to the CDW state. As a characteristic transition temperature T_p we choose here the crossing point of linear extrapolations from the high and low temperature parts as depicted in Fig. 5.6. The transition lines extracted in this way are shown for three different pressures in Fig. 5.7. Noteworthy, other methods of determining T_p, e.g. max. curvature or a typical kink in

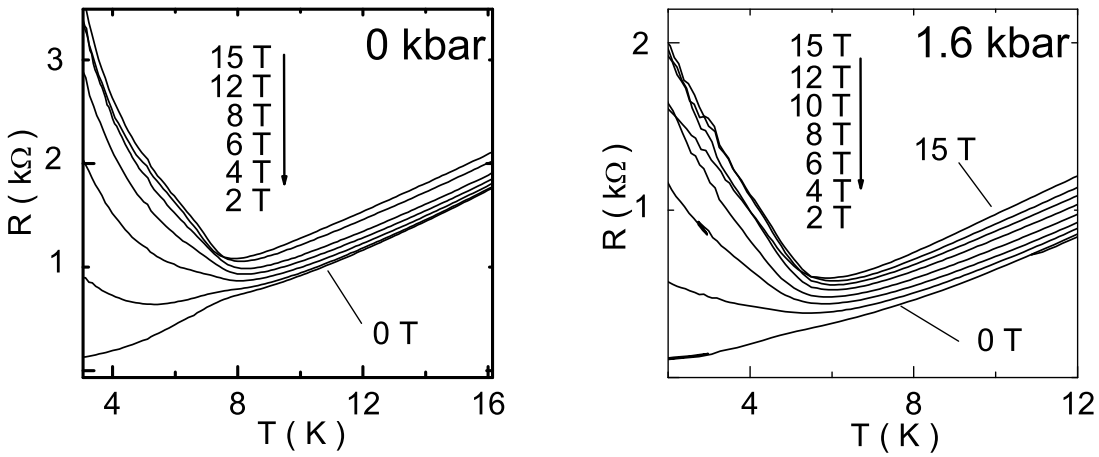

Figure 5.5: Temperature sweeps at several different constant magnetic fields at ambient pressure (left) and under hydrostatic pressure of 1.6 kbar (right).

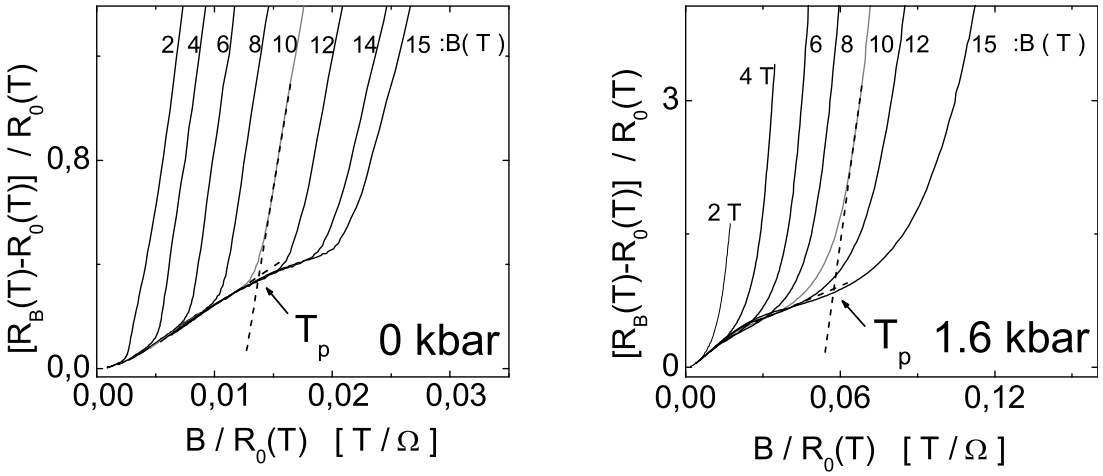

Figure 5.6: Kohler plots of the curves shown in Fig. 5.5. Dashed lines show the determination of the transition temperature T_p at 10 T.

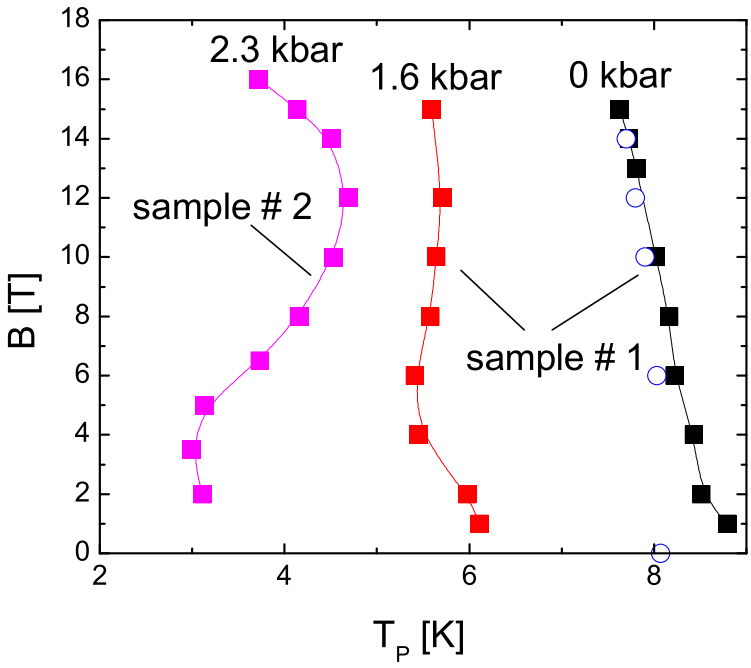

Figure 5.7: Transition temperatures extracted from the Kohler plots for 3 different pressures. At 2.3 kbar the transition temperature clearly increases with field between 5 and 12 T. Open circles mark the transition points found at ambient pressure in specific heat measurements [75]

the derivative of the Kohler plots, did not change the general behaviour of T_p that is going to be discussed in the following. The fact that at ambient pressure the observed transition points do coincide well with those determined from magnetic torque [12] and specific heat [75] (see Fig. 5.7) measurements to our opinion verifies this extraction method of transition points from the magnetoresistance. This method we thus assume to be also applicable under hydrostatic pressure.

At 2.3 kbar wee see that, although no zero-field anomaly was found, the density wave has still a finite T_p at low fields. We therefore suggest $T_p(B{=}0\ \mathrm{T})$ to take a close value, being already less than half the one at ambient pressure. Reconsidering Fig. 5.3 from above we therefore conclude that 2.3 kbar is almost the critical pressure P_0, for which $t_c' = t_c'^*$.

Besides the general suppression of the transition temperature with pressure, the shape of the phase line itself also changes. As seen in Fig. 5.7, it gets a kind of warped structure and at 2.3 kbar the derivative dT_p/dB, between 4 and 10 T, becomes positive. Thus magnetic field clearly stabilizes the CDW state in a certain

pressure and field range.

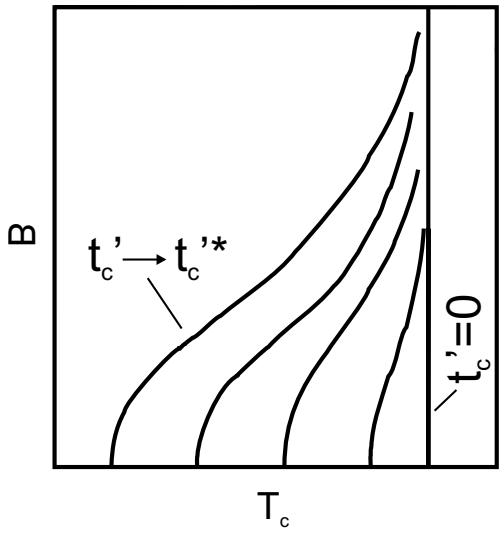

Figure 5.8: Proposed orbital effect on the transition temperature of a Q1D SDW system. The lines correspond to different nesting conditions. Compare with Fig. 5.3.

In order to understand this behaviour we recall the orbital effect of magnetic field on a Q1D electron system. The orbital motion along the open orbits on the Fermi surface leads to an oscillating motion of Q1D carriers in real space that, with increasing field, becomes more restricted to the conducting chains within the plane, as discussed in sec. 2.1.3. This effective reduction of dimensionality in the electron system is known to stabilize a spin density wave [5, 2]. A picture describing how this should theoretically affect the transition temperature of a SDW system, proposed by Montambaux [30], is sketched in Fig. 5.8. The lines correspond to different nesting conditions. For $t_c' = 0$ the system is perfectly nested, possessing the highest possible transition temperature. In magnetic field T_p remains unchanged. With increasing t_c' the zero-field T_p moves to lower temperatures due to imperfect nesting, as described above (Fig. 5.3). The stabilization of the SDW in magnetic field due to the orbital effect then leads to a quadratic increase of T_p. This increase remains, however, only quadratic as long as the characteristic frequency of orbital motion $\omega_c = eBv_F a_y/\hbar$ is much smaller than $t_c'/\hbar$. For $\hbar\omega_c \gtrsim t_c'$, $T_p(B)$ starts to saturate and finally approaches the value of perfect nesting.

Since in the title compound the CDW emerges from the imperfectly nested Q1D sheets on the Fermi surface a strong impact of the orbital effect on T_p should also be expected. However the additional, Pauli effect of magnetic field, suppressing the CDW, competes with the orbital effect. By taking into account both effects of magnetic field the observed phase lines can be understood as follows. At ambient pressure, where we expect $T_p(B = 0\ \mathrm{T})$ to be rather close to the value of the perfectly nested system, the orbital impact on the system must be small and the Pauli

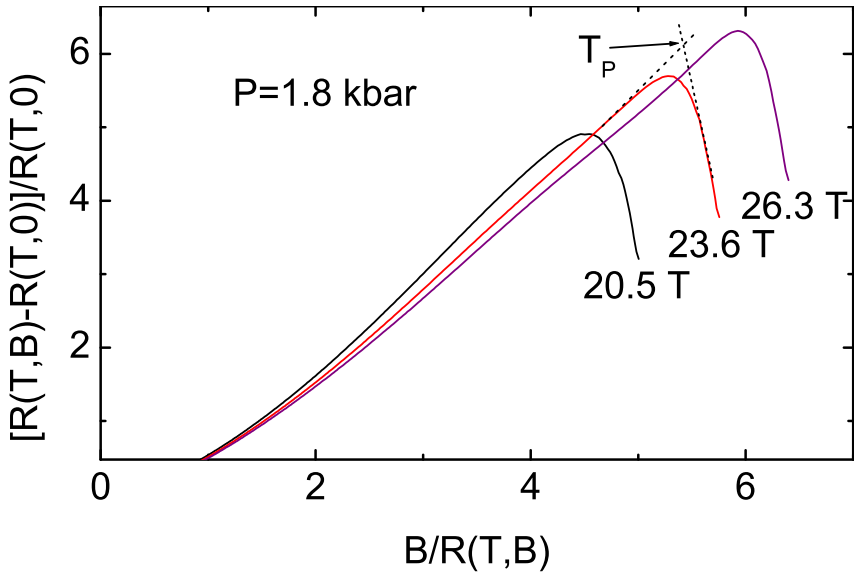

Figure 5.9: Kohler plots of the temperature sweeps made at const. fields above the kink transition at 1.8 kbar. The break down of Kohler's rule within the high field CDW$_x$ state is clearly reflected.

effect dominates. T_p decreases in magnetic field.[1] At $P = 2.3$ kbar the transition temperature is already strongly suppressed at zero field due to imperfect nesting. In this case the orbital effect, in the low field range, exceeds the Pauli effect. This is reflected in an increasing T_p with field until, at higher fields, the orbital contribution saturates and the CDW again becomes suppressed due to the Pauli effect.

Above we have investigated the effect of pressure on the low field CDW state. Now we come to the high field CDW$_x$ state. Also here, Kohler plots of the temperature sweeps entering the CDW$_x$ state (Fig. 5.9) showed a strong deviation, so that even in this high field range a determination of transition points could be done. Finally one should note that, since in magnetic field sweeps SdH oscillations from the Q2D part of the Fermi surface emerge, the temperature dependent resistance at constant fields may be influenced, especially in high magnetic fields. For this reason care was taken that all temperature sweeps were made at constant magnetic field values corresponding to the zero-phase of the quantum oscillations. A falsifying contribution from the SdH oscillations in the determination of transition points therefore can be neglected.

[1] A small but finite orbital impact on the transition temperature at ambient pressure has been proposed by a comparison of the B-T phase diagrams at different directions of magnetic field [12].

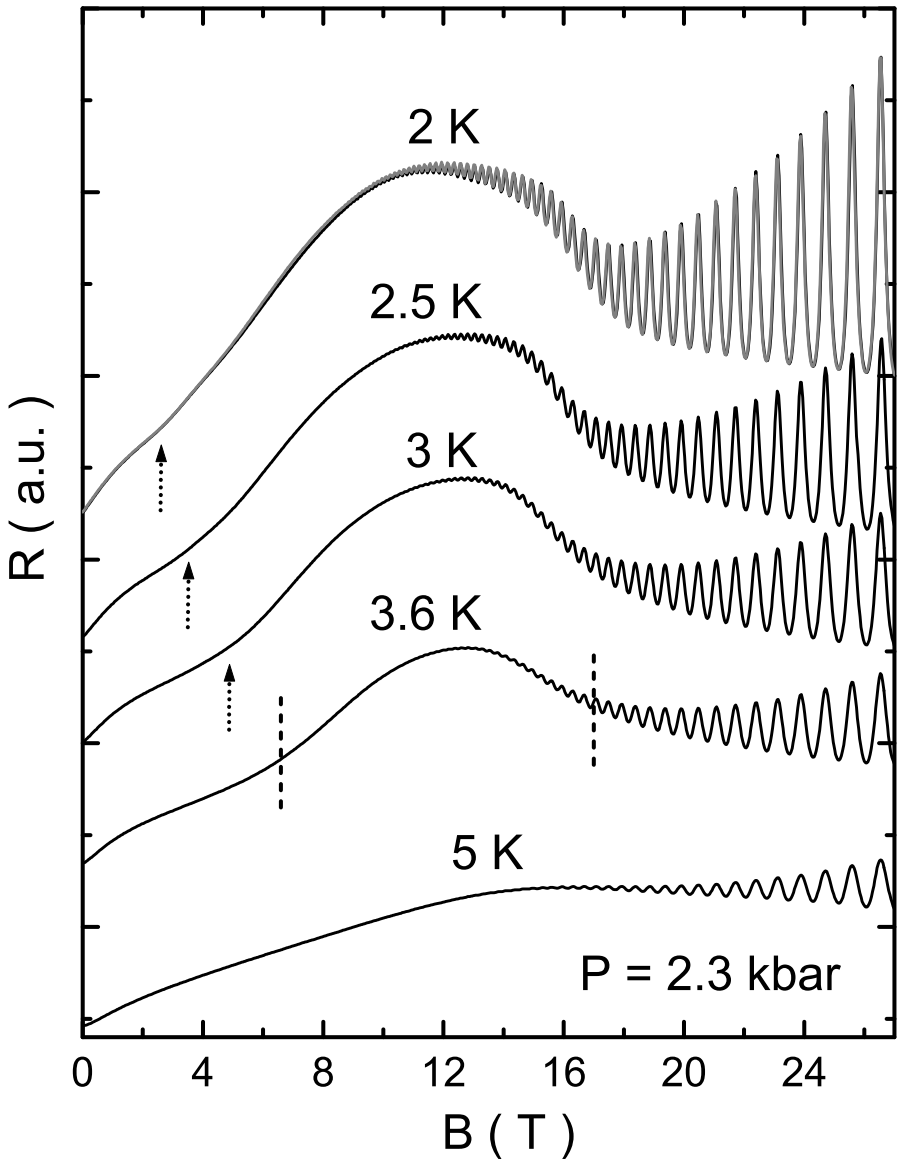

Figure 5.10: Isothermal magnetoresistance at different temperatures and 2.3 kbar. The curves are offset from each other. Dashed lines mark the transition points expected from Fig. 5.7. The dashed arrows mark an anomalous feature observed on lowering the temperature.

Before putting all the determined transition points into a combined phase diagram, we first discuss now some experimental results on the field dependence of the magnetoresistance.

To remind, within isothermal field sweeps at ambient pressure the magnetoresistance reaches a maximum that most likely occurs due to magnetic breakdown between the open sheets and the small lenses on the reconstructed Fermi surface (see sec. 3.4). At ambient pressure and 1.4 K this maximum of the resistance typically occurred in the field range of 11-12 T, exceeding the zero-field resistance by a factor of 20-300. Such a strong sample dependence is thought to be due to different scattering rates, i.e. different sample qualities. With further enhancing the field the background magnetoresistance decreases due to a stronger magnetic breakdown probability until at about 24 T a typical kink characterizes the first order transition into the high field state. The SdH oscillations start to appear close to the maximum in the background resistance, in agreement with the breakdown model [85].

We now present changes occurring on applying hydrostatic pressure. A set of field sweeps taken at 2.3 kbar is shown in Fig. 5.10. For clarity the curves are offset from each other. In the low field range (< 10 T) there are clear features seen in the magnetoresistance. To understand this, a comparison with the transition points presented in Fig. 5.7 turns out to be helpful. At 5 K the isothermal field sweep is expected to be completely within the NM state. This is in line with the observed moderate increase of the magnetoresistance with field showing no sign of any transition. Such a behaviour is also known to occur in the isostructural compound $\alpha-(\text{BEDT-TTF})_2\text{NH}_4\text{Hg(SCN)}_4$, which does not undergo a CDW transition and is normal metallic at low temperatures. At 3.6 K and 2.3 kbar we expect an entrance to the low field state at about 6.5 T and a re-establishment of the NM state at 16.5 T. These fields are marked by dashed lines in the 3.6 K field sweep in Fig. 5.10. Obviously there is a very good agreement between the temperature and the field sweeps if one expects the typical increase of the magnetoresistance within the CDW state. With further lowering the temperature the low field feature weakens and moves to lower fields, as indicated by the dashed arrows in Fig. 5.10. Below 3 K the slope of the magnetoresistance near 0 T starts to increase, suggesting the CDW state already to exist at zero field. The weak feature at low fields still existing below 3 K we therefore attribute to the vicinity of the phase line and not to a real transition.

Altogether, the phase line determined from Kohler's rule is thus clearly reflected in magnetic field sweeps. The kink transition field , deduced by the crossing point of

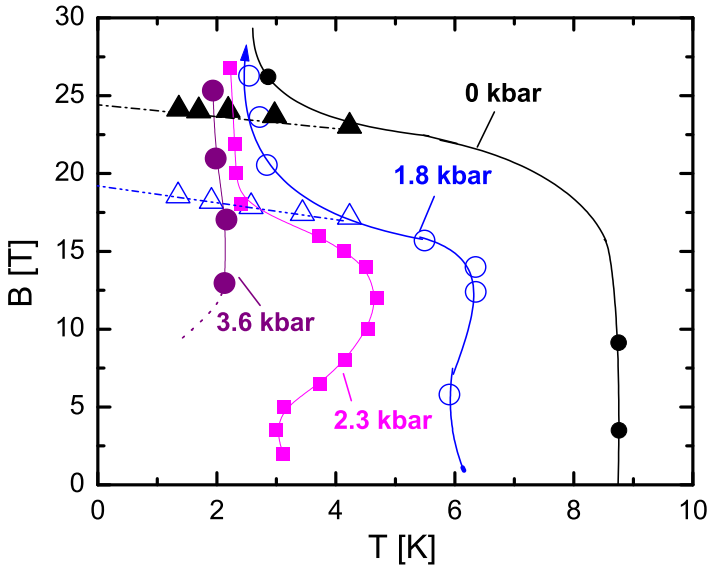

Figure 5.11: B-T phase diagrams determined for different pressures. The points for each pressure were obtained within the same experiment on the same sample. The lines show the behaviours observed on several samples. Triangles mark the kink transition fields at different temperatures for ambient pressure and for 1.8 kbar.

linear extrapolations from both sides of the transition (not shown here), obviously moves down in field with pressure. At 2.3 kbar it is located at about 17 T, that is 70 % of the ambient pressure value, also having a slight temperature dependence. At higher temperatures in Fig. 5.10 we expect a re-establishment of the NM state at $B \gtrsim 17$ T while at lower temperatures there should be a transition to the CDW_x state.

The B-T-P phase diagram

The resulting B-T phase diagrams for four different pressures are pictured in Fig. 5.11. For clarity only points from the very same experiment for each pressure are plotted. The solid lines correspond to the behaviour observed on several samples from different batches. Additionally, triangles mark the kink transitions into the high field CDW_x state, extracted from magnetic field sweeps at constant temperatures. Obviously, the low field CDW_0 state, especially at low magnetic fields, is suppressed

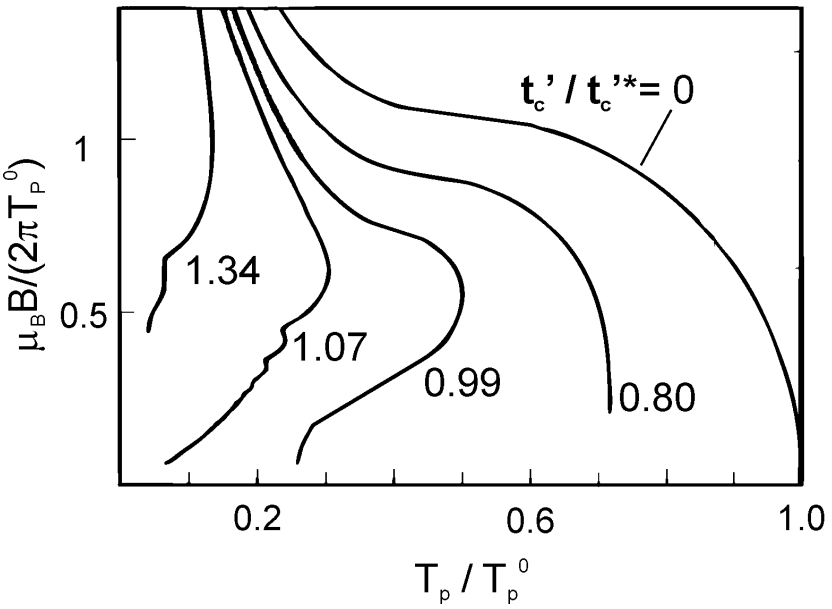

Figure 5.12: Proposed $B-T$ phase lines for a CDW system at different nesting condition. The imperfect nesting is introduced by the effective next-nearest-interchain transfer integral t_c'. $t_c'^*$ corresponds to the value of t_c' for which $T_{p,\mathrm{CDW}}(B = 0\ \mathrm{T}) = 0\ \mathrm{K}$. The kink transition is not shown here.

by pressure much more rapidly than the high field state. This leads to the observation that at 3.6 kbar no clear sign for the low field state is present any more above 1.4 K while the high field state still persists. Additionally, the kink transition field is observed to decrease with pressure [93].

As a whole the phase lines are strikingly similar to those predicted by Zanchi et al. [14] for a (Q1D) CDW system with varying nesting conditions. The latter are shown in Fig. 5.12. Here, t_c' and $t_c'^*$ are defined as above. For $t_c' < t_c'^*$ there exists a finite zero-field transition temperature and all Q1D electrons are gapped within the CDW state. If t_c' exceeds the critical value a part of the Q1D electrons would be ungapped at zero field. In this case, the CDW state can only be stabilized by the orbital effect of a magnetic field. The transition between the low field CDW state and high field CDW_x state was analyzed so far only for a perfectly nested system ($t_c' = 0$). Therefore, the phase diagrams in Fig. 5.12 do not include this transition.

We now compare the theoretical phase diagrams to the observed ones. Obviously, the estimation in the previous section of 2.3 kbar being very close to the critical

pressure value corresponding to $t_c'^*$ is also reasonable within magnetic field. The finding that at 3.6 kbar deviations from Kohler's rule above 1.4 K could only be found at $B > 12$ T strongly suggests that here $t_c'/t_c'^* > 1$. The proposal made above that t_c' at ambient pressure is considerably higher than zero remains also reasonable, since we do observe a rather steep phase line at low fields (the designation CDW_0 state we will take from now on for the low field CDW state at ambient pressure). One sees that our experimental observations can be qualitatively well described by a theoretical CDW model of a Q1D system at different nesting conditions. Thus, hydrostatic pressure serves as an experimentally accessible parameter that tunes the nesting conditions of the CDW system. Remarkably, this is the first direct evidence for an orbital stabilization of a CDW system within magnetic field.[2]

Yet, we do not pretend to make an explicit quantitative comparison between the experimental and theoretical phase diagrams here due to several reasons:

- The theoretical phase lines depend to some extend on the values of the coupling constants [14] which are not known for the present compound;
- The theory does not take into account effects of fluctuations. It is known that for such a low dimensional CDW system they cannot be neglegted [19]. In many CDW systems the value $2\Delta/k_BT_{3D}$ well exceeds the weak coupling BCS result of $2\Delta/k_BT_{3D} = 3.52$, suggesting that the transition temperatures are significantly lower than the mean field transition temperature, T_{CDW}^{MF} [19]. Examples for various CDW compounds are shown in Tab. 5.1.
- In our system there is an additional Q2D-electron band that is theoretically not taken into account and might also lead to quantitative modifications of the phase diagram.

Nevertheless, the qualitative physical understanding of our determined B-T phase diagrams at different pressures gives further strong arguments for the CDW nature of the present low temperature ground state. This immediately raises some interesting questions for further experimental investigations, namely:

→ 1. Zanchi et al. [14] predicted successive field-induced CDW transitions to occur under the conditions $t_c > t_c'^*$. Therefore, in order to check the possible

[2] A possible increase of T_p by $\approx$ 0.5 K ($\Delta T/T_p \approx$ 1%) in a field of 22.6 T in the CDW compound $NbSe_3$ was mentioned by R.V. Coleman et al. [102]; however, as noted by the authors, this increase did not exceed their experimental error bar.

compound	T_c(K)	$2\Delta_\rho$(K)
KCP	189	1400
$K_{0.3}MoO_3$	183	920
$TaSe_3$	215	1600
$NbSe_3$	145 and 59	700
$(TaSe_4)_2I$	263	3000

Table 5.1: Transition temperatures T_p and single particle gaps Δ_ρ (as obtained from the *dc* resistivity) for some linear chain compounds with a CDW ground state; from [19]

existence of these new phenomena the corresponding pressure range, $P > P_0 = 2.5 \pm 0.1$ kbar has been intensively investigated. The results will be presented in section 5.3.

→ 2. The experimental results considered up to now were obtained in a magnetic field applied perpendicular to the layers. It is certainly interesting to study the changes that may occur with tilting the field direction towards the conducting planes. This will be discussed in section 5.4.

→ 3. We know that another compound of this family of organic conductors, $\alpha-(\text{BEDT-TTF})_2\text{NH}_4\text{Hg(SCN)}_4$, does not undergo a density wave transition but becomes superconducting below $T \approx 1$ K. Since we can easily suppress the CDW state, the possible existence of a superconducting state under pressure has been investigated that will be presented in section 5.5.

It is however important to first figure out some physical properties of the different states existing in the title compound that is going to be presented in the following section 5.2.

5.1.3 Conclusion

The effect of pressure on the B–T phase diagram of the organic CDW compound α-(BEDT-TTF)$_2$KHg(SCN)$_4$ was investigated at $\overrightarrow{B} \perp$ **a-c** plane.

Hydrostatic pressure is found to suppress the CDW state. At about 2.5 $\pm$0.1 kbar the CDW is suggested to become completely suppressed at $B = 0$ T. In order to extract phase transitions from the magnetoresistance, Kohler's rule turns out to be well applicable. The obtained B-T phase diagrams can be consistently interpreted in terms of an interplay between the Pauli and orbital effects of the magnetic field on a CDW system. A recent theoretical model of a Q1D CDW system with varying nesting conditions turns out to describe the observed phase lines remarkably well. The experimental data thus gives further evidence for a CDW ground state in α-(BEDT-TTF)$_2$KHg(SCN)$_4$. Altogether, hydrostatic pressure turns out to easily tune the nesting conditions of the present CDW system. A strong increase of the transition temperature with magnetic field is found in a certain pressure and field range. We associate this result with a dramatic enhancement of the orbital effect of magnetic field due to a deterioration of the nesting conditions by pressure. This is the first direct evidence for an impact of the orbital carrier motion on the transition temperature of a CDW system [103].

5.2 Properties of the CDW state

5.2.1 dHvA and SdH Effects

One of the most direct indications of the reconstructed Fermi surface within the CDW_0 state besides the anomalous angle dependent (semiclassical) magnetoresistance is the appearance of additional frequencies in the spectrum of quantum (SdH and dHvA) oscillations. For a review on this topic see e.g. [9, 61].

A typical example of the oscillatory magnetoresistance at ambient pressure and two different temperatures is shown in Fig. 5.13, where the semiclassical (background) resistance has been removed by dividing by a polynomial fit. As before, the field is applied perpendicular to the **a-c** plane. Obviously, different frequencies are contributing within the CDW_0 state whereas in the high field CDW_x state one frequency is dominating. The corresponding fast Fourier transformation (FFT) of the curves, replotted in inverse field scale, are given in Fig. 5.14. In the CDW_0 state three different frequencies and their higher harmonics contribute to the oscillations with different amplitudes. At low temperatures the frequency labeled α, at ≈ 670 T, together with an anomalously high second harmonic content become dominant. Within the CDW_x state only α and its moderately strong second harmonic remain. The α frequency of the oscillation is established not to change on crossing the high field phase boundary and to also be present within the normal metallic state. It therefore belongs to the cylindrical or Q2D part of the Fermi surface.

The fact, that the cylindrical Fermi surface gives rise to only one single frequency, reveals the very high anisotropy of the electron system. This means that the warping of the cylinder, $\sim 2t_b/\hbar v_F$, must be very small. Otherwise we would see two slightly different frequencies corresponding to the minimum and maximum cross-sections and with it a typical beating behavior of the quantum oscillations. Examples for such a behavior, observed in other organic metals, can be found e.g. in the review of Wosnitza [9].

Within the CDW_0 state additional peaks are observed at frequencies of about 175 T and 850 T, hereafter labeled λ and ν, respectively. These frequencies definitely cannot be explained by the Fermi surface in the normal metallic state and must originate from new closed orbits appearing under reconstruction due to the density wave. While a general suppression of ν on going to temperatures below 1 K was always found, the relative amplitudes of these frequencies with respect to α turned out to be strongly sample dependent.

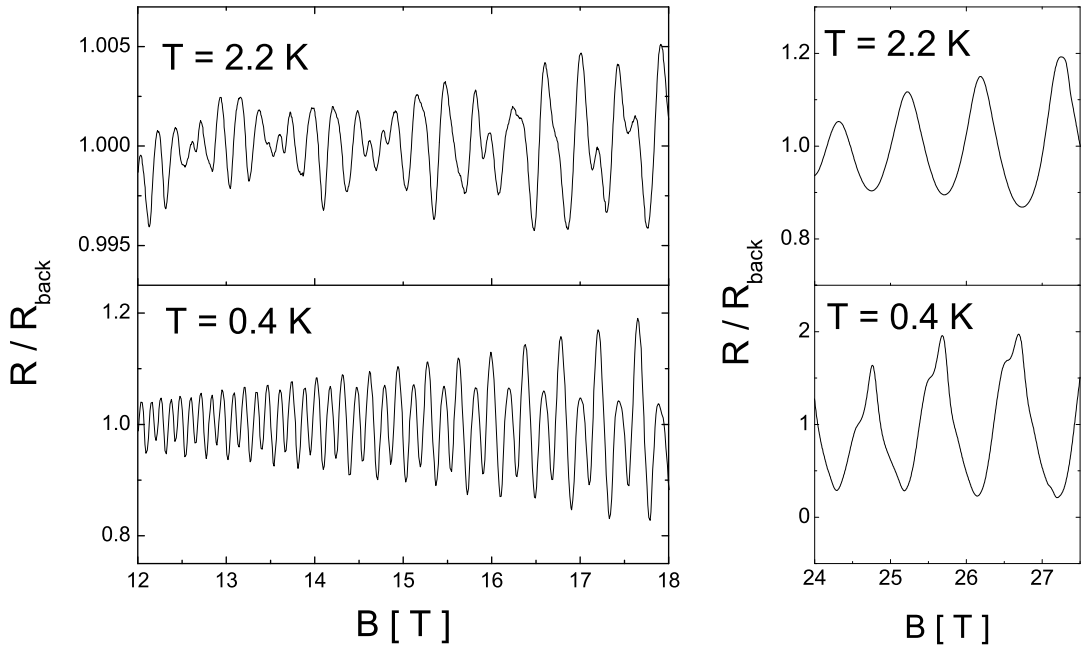

Figure 5.13: SdH oscillations at different temperatures and fields above (right) and below (left) the kink transition. The curves are normalized to the non-oscillating background magnetoresistance

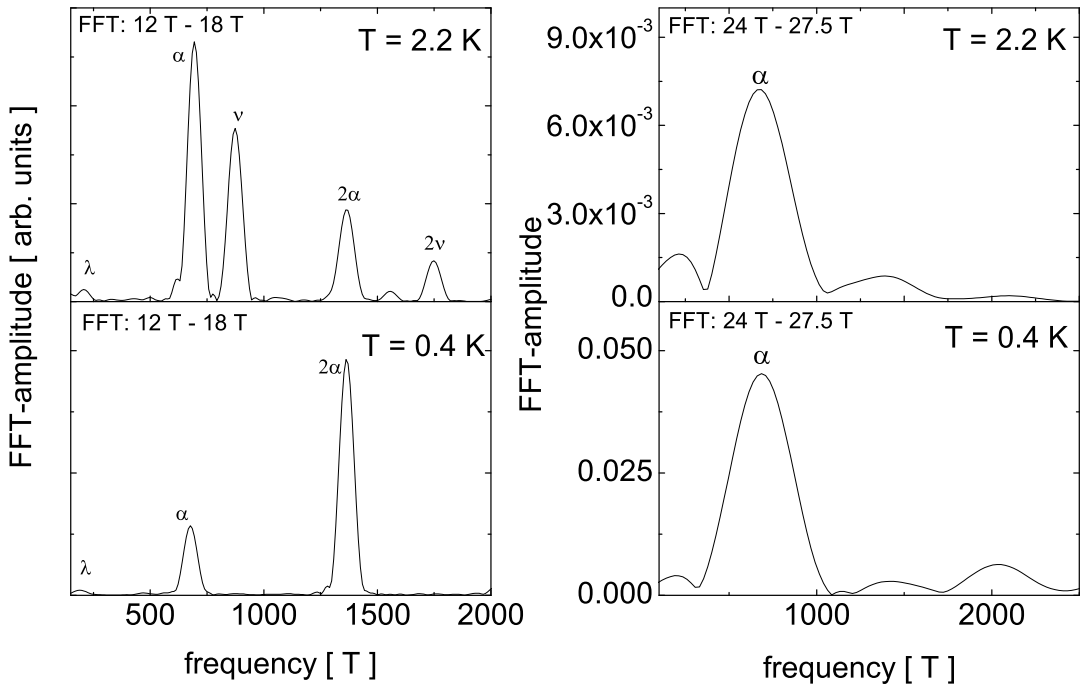

Figure 5.14: Corresponding FFT spectra of the curves in Fig. 5.13

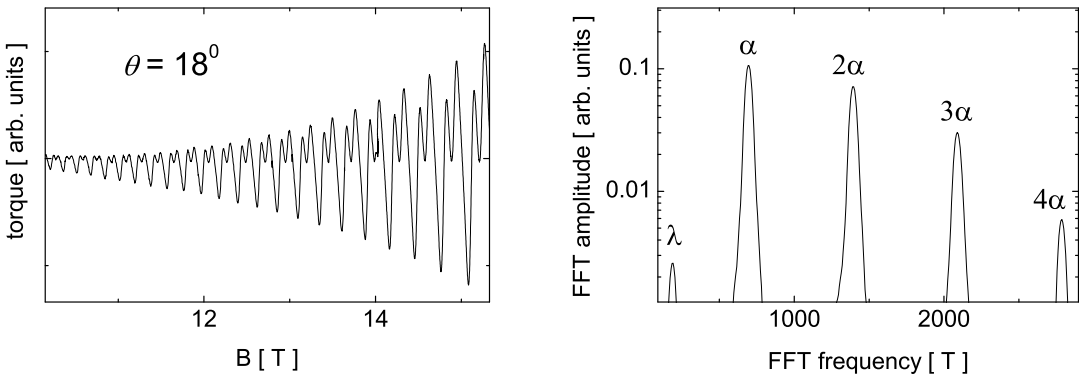

Figure 5.15: Left: Oscillating magnetic torque, the background has been removed by subtraction of a low order polynomial fit. The magnetic field is tilted by 18° from the perpendicular direction. Right: Corresponding FFT spectra of the dHvA oscillations.

By contrast to the SdH oscillations, the only additional frequency observed in dHvA measurements is λ. No sign of ν has been found, whereas ν in SdH experiments sometimes even exceeds α in amplitude. Fig. 5.15 shows an example of the field dependent torque together with its FFT spectrum. A possible explanation for such a finding, and in fact the only known mechanism up to date, is that ν arises mostly due to quantum interference. This effect, first proposed by Stark and Friedberg in 1971 [104], occurs when for the same electron (or hole) wave packet there is a possibility to travel on two different trajectories in k-space, which eventually come together again, see Fig. 5.16. The interference of the corresponding wave amplitudes gives rise to the oscillatory probability of propagating from P_1 to P_2. This is reflected in an oscillating magnetoresistance, periodic in $1/B$. The frequency is determined by the area enclosed between the two trajectories in a way similar to the usual SdH effect. Since the electron does not circle around a closed orbit the energy spectrum is not quantized. Therefore, thermodynamic quantities are not influenced by this interference; the effect will not be observed in dHvA measurements. Hence, we conclude that only the α and λ frequencies arise due to closed orbits on the Fermi surface. Noteworthy, this is the first report of the λ frequency in the dHvA effect, it was actually believed only to appear in the SdH effect [61]. Within the error of the frequency determination ν

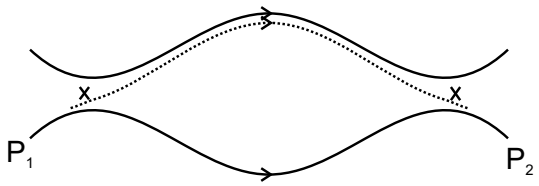

Figure 5.16: Stark quantum interference: due to magnetic breakdown the electron has two possible trajectories in k-space on going from P_1 to P_2.

equals to the sum $\alpha + \lambda$. This suggests the quantum interference to arise between these two closed orbits.

Within the huge amount of investigations on the SdH oscillations during the last decade there have also been other frequencies reported for the CDW_0 state [105, 15, 106] such as 750 T or 4200 T, the latter proposed to be a magnetic breakdown orbit between open and closed parts of the unreconstructed Fermi surface. Such frequencies have, however, not been found in our investigations on various high quality samples from different batches. We therefore believe that all these additionally reported frequencies cannot be taken as a real property of the CDW state and might be an experimental artifact, e.g. due to the use of polycrystalline samples.

The occurrence of a large second harmonic contribution of the α frequency at low temperatures in both SdH and dHvA measurements has been a subject of intense discussions during the last decade. Several suggestions concerning the anomalously large amplitude of 2α have been made. The easiest explanation would come from the standard Lifshitz Kosevich theory. In principle it may occur due to the spin splitting reduction factor. At certain conditions the latter suppresses the first but not the second harmonic of the oscillations [35]. However, the observed dependence of the oscillation amplitude on the field orientation for both the first and second harmonics shows a behaviour that is inconsistent with the usual Zeeman mechanism [11, 107] (see also sec. 5.2.5). Another proposal by Athas et al. [108], that the occurrence of the strong second harmonic is linked to the AMRO maxima, was ruled out in our measurements. An interesting explanation was given by Harrison [109]. He suggested the huge second harmonic content to arise because of oscillations of the chemical potential in the highly 2D electron system. His theoretical model is based on the assumption that the CDW potential is commensurate with the underlying crystal lattice and has a constant field-independent wave vector. Since the Q1D carriers are gapped within the CDW state, he expects the quantum oscillations to be in the limit of no carrier reservoir [35, 109]. The chemical potential thus immediately starts to oscillate with the quantum oscillations that in turn causes the effective energy gap of the CDW also to be modified. The eventual oscillation of the free energy of the whole system will then have a frequency twice as large as the initial oscillation frequency of the Q2D electrons. This causes a very strong second harmonic contribution in the dHvA and very likely also in the SdH signal. Since such a frequency doubling also seems to be present in another CDW compound,

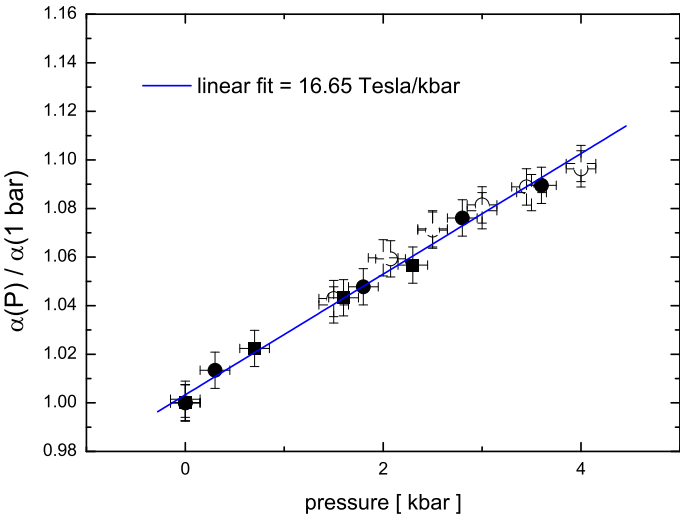

Figure 5.17: Pressure dependence of the α-frequency.

$NbSe_3$, with additional ungapped parts of the Fermi surface [110, 109], this model indeed looks promising.

There are, however, some questions concerning the applicability of Harrison's model to the present compound. At not too high fields, the free carriers in the CDW state are supposed to mostly run on open trajectories in k-space while a small part contributes to quantum oscillations due to magnetic breakdown. The electron's on the open orbits can be considered as a reservoir and, therefore, we would not expect the chemical potential to oscillate at such fields. An enormous second harmonic contribution is, however, observed in some samples immediately when the quantum oscillations set in. Another problem is that at higher fields the chemical potential oscillations are predicted to even exceed the CDW gap causing successive first order transitions between the CDW and NM states with field. Besides the fact that such successive first order transitions are not observed, the NM state will never be stabilized because the system in this temperature range always changes from the CDW_0 to the modulated CDW_x state which is certainly energetically more favorable. The possibility of the modulated state was not taken into account by Harrison. Further investigations on this topic might clarify these inconsistencies.

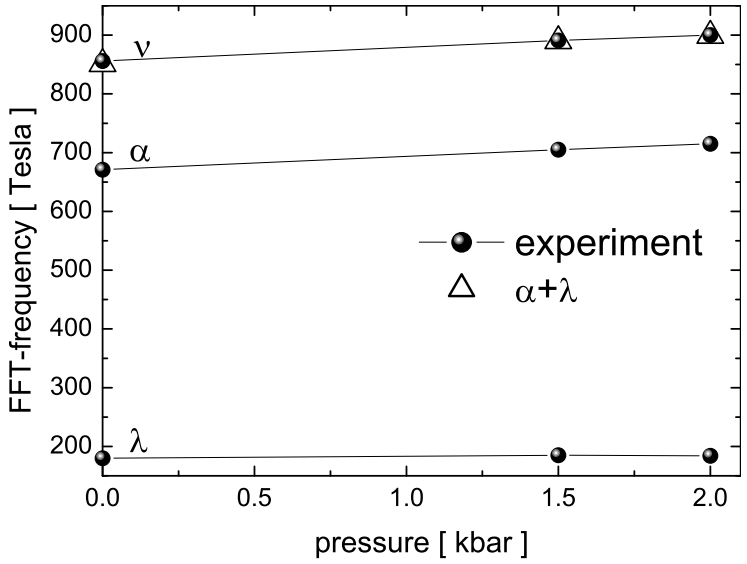

Figure 5.18: Pressure dependence of different SdH frequencies, obtained on the same sample.

5.2.2 SdH Effect under Pressure

Under hydrostatic pressure the crystal volume is reduced, the Brillouin zone expands and therefore an increase of the Fermi surface cross-sectional area can be expected, assuming the amount of Q2D electrons to stay constant. In Fig. 5.17 the increase of the α-frequency, normalized to the ambient pressure value, is plotted for several different samples. For each sample the pressures have been applied successively, i. e. without opening the clamp cell. This is important, since the sample orientation with respect to the magnetic field at different pressures is thus kept the same. For a cylindrical Fermi surface it is easily shown, that the frequency changes with $1/\cos(\theta)$, where θ is the angle between the field direction and the direction perpendicular to the planes. On keeping the sample orientation the same at different pressures, one thus gets the correct relative pressure dependence of the α-frequency. A rather linear pressure dependence of ≈ 16.7 T/kbar is found corresponding to a dependence of the Fermi surface area $S(P)$ on pressure given by $d[\ln(S)]/dP \approx 2.5$ %/kbar. This differs from the previously reported values of 10 and 12.1 T/kbar found by Hanasaki et al. [16] and Brooks et al. [15], respectively. Since our pressure value was directly monitored at low temperatures with a calibrated manganin coil, while the other two groups presumably only took a constant (pressure independent) pressure drop inside the clamp cell between room temperature and low temperatures, we think that our

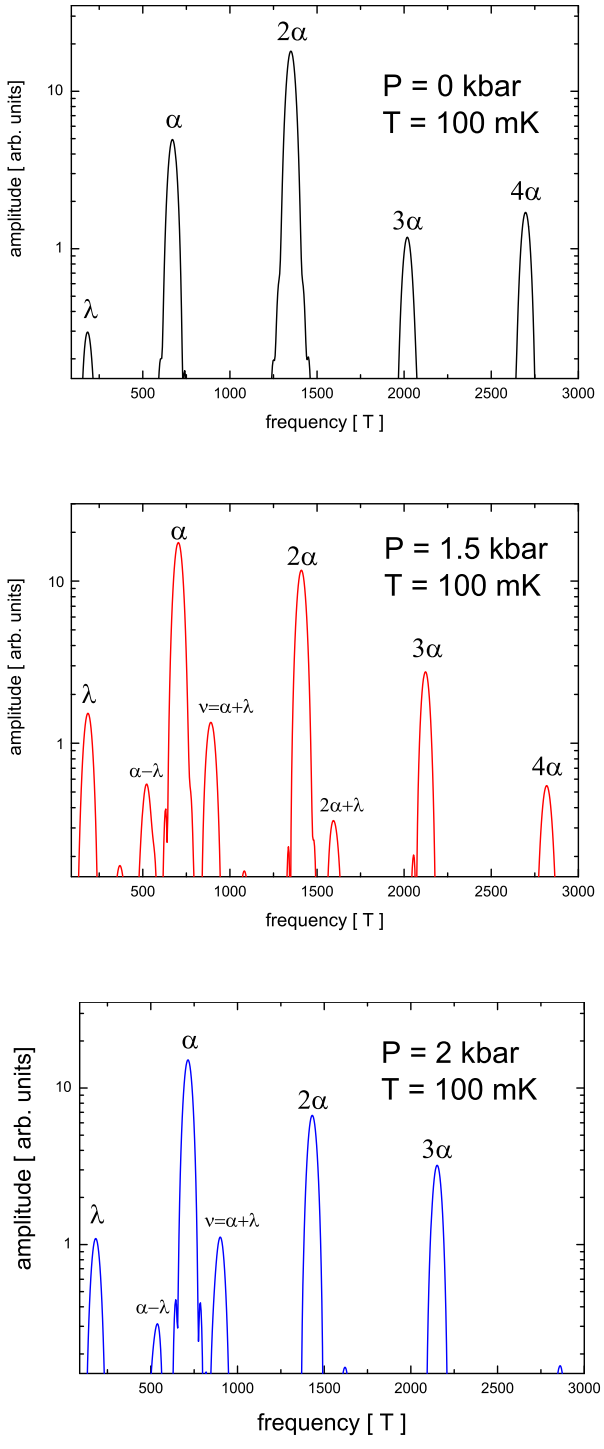

Figure 5.19: FFT spectra for one sample at different pressures and 100 mK.

result is more reliable. According to our results the pressure drop on cooling is in fact pressure dependent. Our data on the α frequency turns out to coincide very well with the theoretical prediction by Campos et al. [111]. In their tight binding calculations an isotropic compressibility of the crystal lattice was assumed.

Contrary to the α frequency, the λ frequency was found to be within the accuracy of frequency determination pressure independent. Frequency ν exactly follows the value of $\alpha + \lambda$ over the whole pressure range, see Fig. 5.18. This strongly supports the suggestion that ν is a combination of α and λ, arising due to quantum interference. Besides ν, other combinations of α and λ are also observed under pressure. Concerning the oscillation amplitude, the α oscillation shows a general tendency to become enhanced under hydrostatic pressure that may be expected due to a decrease of the magnetic breakdown gap. The amplitude of the additional frequencies, on the other hand, turned out to show no systematic changes under pressure. However, these frequencies clearly persist at low temperatures within the CDW state. Examples of the FFT-spectra for one sample at different pressures and T=100 mK are shown in Fig. 5.19.

5.2.3 Oscillation Phases

Another interesting property of the CDW states in the present compound is the phase inversion of the α-oscillation *in the SdH signal* on changing the temperature or magnetic field while, at the same time, *the phase of the dHvA signal remains constant* [77,112]. An example of such a phase inversion is shown in Fig. 5.20. With lowering the temperature within the CDW_x state the background resistance starts to decrease that is combined with a phase inversion of the SdH signal. This behaviour coincides with results published by other groups [112, 78]. However, not coinciding with predictions of other groups is the observation that the phase inversion as well as the decrease of the background magnetoresistance is also observed below the kink transition, i.e. in the CDW_0 state. Up to now, the phase inversion has been believed to be solely a property of the CDW_x state [112, 78].

Remarkably, the temperature where the phase inversion sets in was found to be strongly sample dependent. For one kind of samples, hereafter referred to as type 1 samples, the phase seemed to keep the same within the CDW states. On approaching the normal metallic state it then becomes inverted in a very narrow field interval. An example is shown for 1.8 kbar in Fig. 5.21 , where the normalized isothermal field

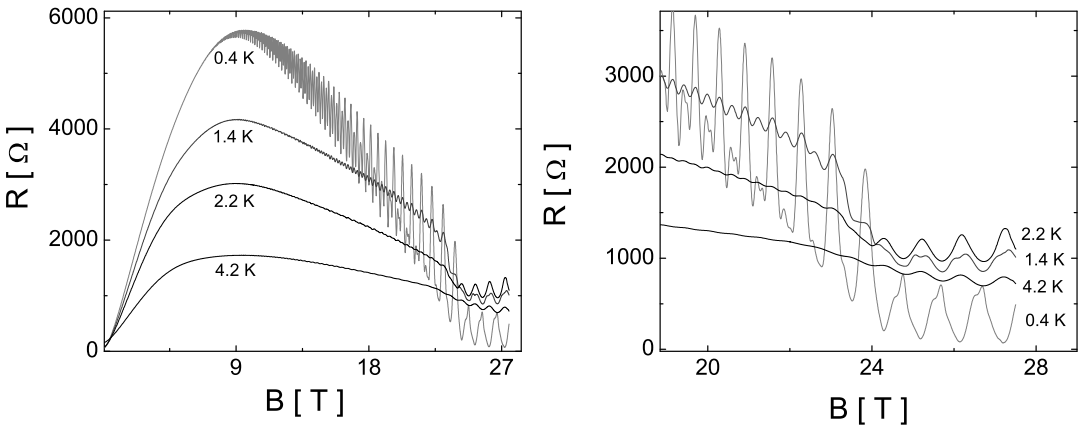

Figure 5.20: Left: several field sweeps at constant T. Right: enlarged high field range. At high fields the background resistance, on cooling, starts to decrease that is accompanied by a phase inversion of the SdH signal.

sweeps are plotted in inverse field scale multiplied by the oscillation frequency, that determines the so-called filling factor. This means that at odd half integer filling factors $F/B = (n + \frac{1}{2})$ the nth Landau level lies approximately on the chemical potential while at integer filling factor the chemical potential is in the middle between the Landau levels. Hence, for a 2D electron gas the highest occupied Landau level would be half filled at odd half integer filling factors while at integer numbers it would be completely filled. As can be seen at high fields and high temperatures the oscillations are in anti-phase with those at low temperatures. The relatively short intervals in magnetic field where the phase inverts are found to be close to the phase boundary between the CDW and the NM states determined above.

Indeed, in the isostructural compound α-(BEDT-TTF)$_2$NH$_4$Hg(SCN)$_4$, which is normal metallic down to the lowest temperatures [62, 9](see sec. 3.4), it has been shown that the oscillating magnetoresistance reveals a minimum at half integer filling factors [42]. We therefore denote in the following the phase with a minimum in the resistance when the Landau level is on the chemical potential as "normal phase" and a maximum in the resistance under the same condition as "inverted phase". On increasing pressure, the fields where the phase inversion occurs decrease. The observed phase inversion lines are shown in Fig. 5.22 in B-T coordinates. As can be seen, these lines resemble pretty much the B-T phase diagrams presented above, Fig. 5.11. This strongly suggests the inverted phase only to exist within the CDW$_0$ and CDW$_x$ states.

Besides these type 1 samples, we found another kind ("type 2") where the SdH

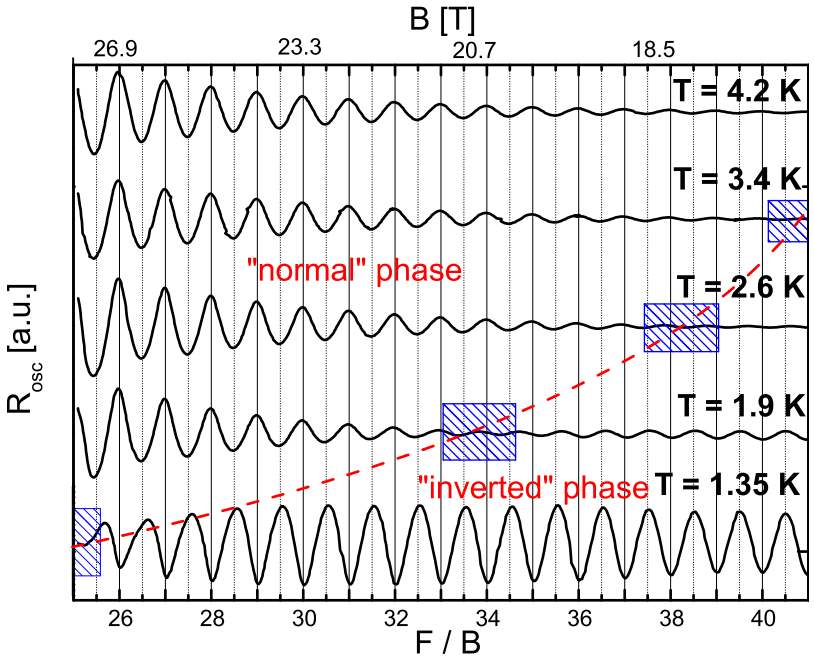

Figure 5.21: SdH signal vs. filling factor F/B for different temperatures and P=1.8 kbar. On approaching the phase boundary the phase of the oscillations inverts in a narrow field interval, marked by the shaded areas. The dashed line is a guide for the eye, separating the "normal" from the "inverted" phase-regions (see text).

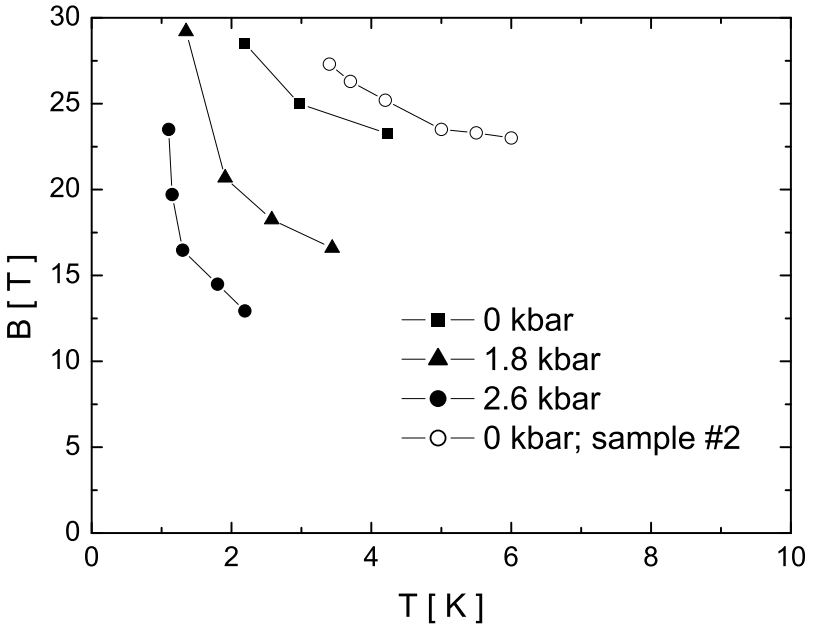

Figure 5.22: Phase inversion lines in a B-T diagram for different pressures. The points determine the midpoints of the field regions, in which the phase inverts (shaded areas in Fig. 5.21).

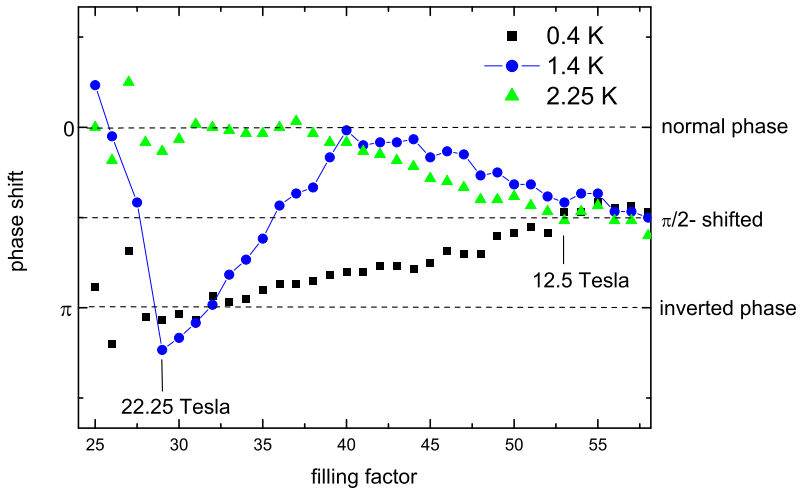

Figure 5.23: Phase of the SdH α-oscillations as typically obtained for type 2 samples. The points are extracted from field sweeps at different temperatures.

oscillations turned out to be more complex. Here the phase was inverted at lower temperatures, i.e. deep inside the CDW states. In the CDW_x state the phase inversion occurs only in a small temperature interval, corresponding to a very steep phase inversion line in the B-T diagram. The data shown above in Fig. 5.20 are an example of type 2 samples. At fields below the kink transition, unlike in type 1 samples, the phase does not stay inverted but changes gradually in a very wide field range. Moreover, below 12.5 T the phase of the first harmonic turned out to be shifted by $\pi/2$ with respect to the high field oscillations. The field and temperature dependent relative phases of the first harmonic are depicted in Fig. 5.23. The data are taken from the original curves presented in Fig. 5.20. The phase has been extracted from the SdH oscillations with respect to the simultaneously measured dHvA oscillations, the latter serving as a phase reference. A general phase inversion on crossing B_k could not be observed on various samples measured. The phase inversion in type 2 samples is thus also not restricted to the high field CDW_x state. The reason for this contradiction with the other reports [112, 78] might be the presence of a strong second harmonic content in the oscillations, that strongly hinders the exact determination of oscillation phases. In order to extract the first harmonic, we filtered out the 2nd harmonic in the FFT spectrum and performed a back Fourier transformation. Fig. 5.24 shows an example of the filtered signal at three different temperatures where the shift in the phase is clearly seen on changing temperature.

The gradual change of the phase in the CDW_0 state suggests that there are differ-

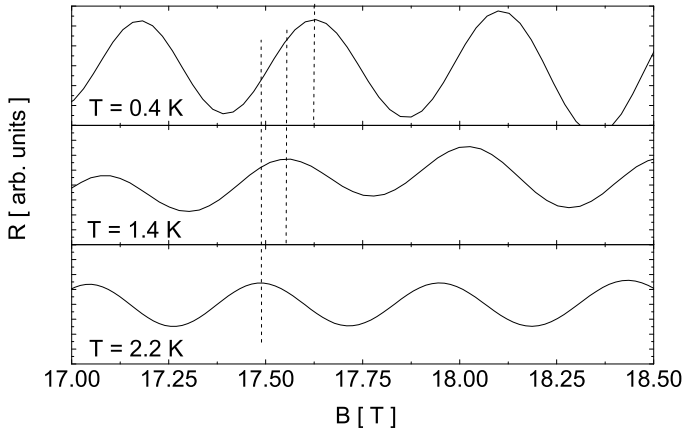

Figure 5.24: Extracted first harmonic from the SdH oscillations at 3 different temperatures. The phase shift on lowering the the temperature is clearly seen.

ent contributions to the SdH effect with different phases. At $T = 2.25$ K in Fig. 5.23 there is the $\pi/2$ shifted phase existing at low fields, and the normal phase becomes more and more dominant with enhancing the field. At low temperatures, $T = 0.4$ K, the inverted phase becomes dominant at higher fields. Similar behaviours were found on samples from different batches.

In our investigations type 1 samples always showed a maximum in the background magnetoresistance within the CDW_0 state that was about an order of magnitude lower than observed in type 2 samples. In the classical AMRO picture this would mean that the carriers in type 1 samples possess a much higher scattering rate. This is also in line with the quantum oscillations which seemed to be stronger damped.

Surprisingly, the phase of the second harmonic for both types of samples is observed not to change with temperature or field and was checked always to correlate with the dHvA signal in the combined resistance/torque measurements. Actually, it is this difference in the phase between the first and the second harmonics in type 2 samples that turns out to explain the (mis-)interpretation of some groups [69,113] concerning their observed SdH oscillations: The modulation of the SdH oscillation with field was thought to occur due to a SDW ground state that would cause a field dependent change of the Zeeman splitting. These proposals are definitely wrong since, once again, the phase shift of the first harmonic does not exist in dHvA oscillations.

One sees that the SdH effect can be very complex in these low dimensional electron systems. Although an exact theoretical simulation of the observed SdH signal

cannot be done at the moment, some qualitative remarks will be given in the following. Since this is a rather special topic, we note here that the discussion below is not needed for understanding further results presented in this thesis.

Normally, the SdH effect for the longitudinal interlayer magnetoconductivity in organic salts with such "highly" Q2D electron systems is considered via the Boltzmann transport equation:

$$\sigma_{zz} = e^2 \int d\epsilon \frac{df(\epsilon)}{d\epsilon} I(\epsilon)\tau(\epsilon) \tag{5.3}$$

where $f(\epsilon)$ is the Fermi distribution function, $I(\epsilon) \equiv \sum \mid v_z(\epsilon) \mid^2$ is the square of the electron velocity summed over all states at the energy ϵ, v_z is the interlayer-component of the electron velocity and $\tau(\epsilon)$ is the momentum relaxation time at energy ϵ. At high enough fields, we can assume the distance between subsequent Landau levels $\hbar\omega_c$ to become bigger than the interlayer bandwidth of the Fermi surface, $4t_\perp$. If then the chemical potential lies in between the Landau levels, the velocity at the Fermi level,

$$v_z(\epsilon_F) = \frac{1}{\hbar}\frac{\partial\epsilon}{\partial k_z}\Big|_{\epsilon\simeq\epsilon_F} \tag{5.4}$$

simply becomes zero. By taking into account the broadening of the levels due to a finite scattering time, the velocity is finite but takes a minimum value. In this case the term $I(\epsilon)$ in Eq. (5.3) determines the phase of the oscillation and one expects a minimum in the magnetoresistance at half integer filling factors, i.e. the normal phase (see Fig. 5.21).

For type 1 samples, we know that in the low field CDW_0 state the phase is inverted. This might be explained by assuming that the density of states oscillation rather than the oscillation of the interlayer velocity determines the phase of the quantum oscillations (after Fermi's golden rule the scattering rate is, to the first order, proportional to the number of states into which scattering is possible). This would mean that in the CDW_0 state the SdH oscillations are probably better described by conventional (3D) SdH theories, in which the scattering rate determines the oscillation phase. A crossover at the phase boundary between the CDW and the NM states would then cause a node in the SdH oscillations, combined with a phase inversion. Such a crossover might explain the behaviour observed in type 1 samples. It is, however, not understood at present why within the CDW_0 state solely the scattering rate should determine the oscillation phase.

The smooth *phase shift* over a wide field range in type 2 samples in the low field CDW_0 state must have a different origin. It might be caused by an interplay of the two oscillating terms in Eq. (5.3), i.e. the carrier velocity and scattering rate.

The change from the $\pi/2$-shifted to the normal phase with field may arise due to an increasing contribution of the carrier velocity to the total oscillation of the conductivity. Another possibility could be the presence of different scattering mechanisms. As has already been pointed out in the early works by Adams and Holstein [40] and Lifshitz and Kosevich [114] two terms add up to give the net (3D) SdH oscillation, one involving inter-Landau band scattering the other intra-Landau band scattering. For not too high fields, i.e. at large quantum numbers the first term may even give the major contribution to the quantum oscillation in the transverse conductivity. Indeed, the possibility of a phase difference between both contributions to the SdH oscillations has also been predicted [40].

Which mechanism eventually leads to such a strong phase shift in the longitudinal magnetoresistance with magnetic field as observed in type 2 samples is not clear, since a detailed theoretical description is still missing. Moreover, it is not clear to the moment if magnetic breakdown also affects the phase of the SdH oscillation.

A detailed theoretical analysis of the SdH effect of Q2D electron systems at different fields and temperatures is needed for a comparison with our experimental data. We emphasize here, that as long as this complex behaviour in the SdH effect is not understood, a reliable extraction of such values as m^*, g^*m^*, and T_D from the SdH signal cannot be done and all reports based on the SdH effect must be considered with great care.

Remarkably, the phase inversion at low temperatures and high fields, illustrated in Fig. 5.20, always occurs together with a strong decrease of the semiclassical (background) magnetoresistance. This is observed on all samples investigated. We, therefore, believe these two effects to be directly related to each other. In other words: as soon as the background resistance starts to decrease the phase becomes inverted. Obviously, an additional, at low temperature even dominating, contribution to the conductivity emerges. This could probably explain the phase inversion. At odd half integer filling factors, i.e. when the Landau level is on the chemical potential, there are more states into which the carriers of this additional conduction channel can scatter. The total resistance therefore increases. Correspondingly, at integer filling factors we then observe a minimum of the resistance. The nature of this additional conductivity contribution to the moment is however not clear. It might originate from partially ungapped Q1D carriers, which are indeed expected within the CDW_x state, but not at fields below the kink transition. Another possibility for an additional contribution to the conductivity is a sliding CDW. This collective motion of the carriers might occur within the CDW state [19]. How this can affect the phase

of the SdH oscillations is, however, not clear at present.

5.2.4 Magnetic Torque within the Modulated CDW$_x$ State

Up to now there is a general agreement about the existence of the CDW$_x$ state at high fields and low temperatures that was first proposed by McKenzie in 1997 [13]. It demarcates itself from the NM one in several distinct properties:

- As was shown by Christ et al. the phase boundary is directly reflected in a change of slope in the temperature dependent magnetic torque at constant field [74, 12, 77].
- In the magnetoresistance a rather strong decrease of the background resistance combined, at low temperatures, with the phase inversion in the SdH signal is typically seen in most of the samples [77, 112, 78].
- Latest AMRO experiments by Kartsovnik et al. showed clear signs of the Q1D AMROs at high tilt angles even at fields above B_k. This can be expected, since with tilting the field the magnetic breakdown gap on the closed orbits should increase and the 2D AMROs should diminish. In the NM state the 2D AMROs are known to dominate over the whole angular range.
- Additionally, the torque signal below ≈ 2 K was found to be hysteretic in field within the CDW$_x$ state [73, 78]. This point we investigated in more detail.

Fig. 5.25 shows the typical behaviour observed in the magnetic torque within the CDW$_x$ state. The background of the magnetic torque shows a considerable hysteresis on sweeping the field up and down. The hysteresis appears to be of diamagnetic origin. Note that this hysteresis has nothing to do with the first order kink transition at 24 T, since it exists up to the highest fields measured. Harrison et al. even showed that this hysteresis persists at low temperatures in magnetic fields up to the highest field of their experiments, 32 T [78]. We also emphasize that by no means this hysteresis can be simply ascribed to the oscillatory part of the torque signal. The hysteresis definitely appears in the background of the torque. Only with lowering the temperature the magnitude of the hysteresis was shown to become slightly dependent on the phase of the oscillation at $B > 28$ T [78]. This is likely related to the observed

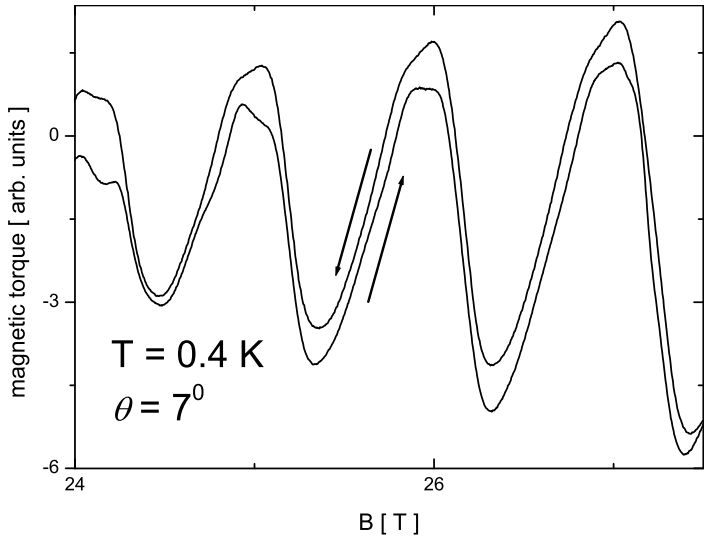

Figure 5.25: The magnetic torque exhibits a strong diamagnetic hysteresis on sweeping the magnetic field up and down, (only) within the CDW_x state.

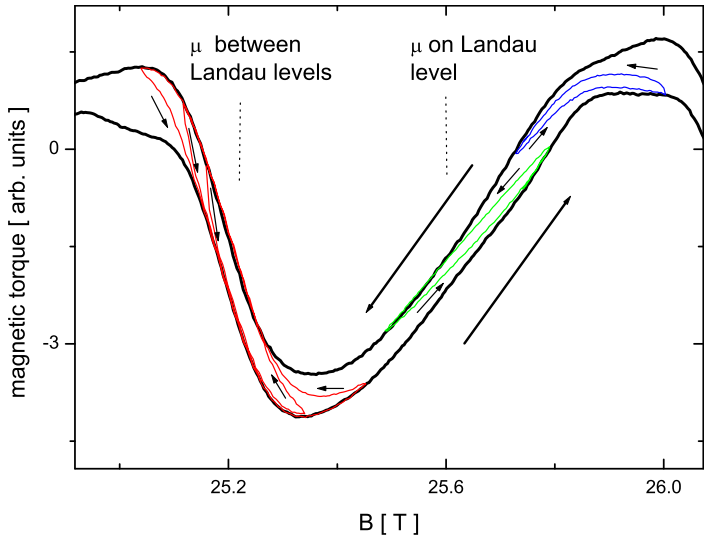

Figure 5.26: Several measured hysteresis loops at different phase positions of the dHvA oscillations. Arrows mark the field-sweep directions.

dependence of the measured hysteresis loops on the position of the chemical potential μ with respect to the Landau levels, see Fig. 5.26: On changing the sweep direction of magnetic field at around half odd integer filling factors the torque needs a much bigger field range to come to the maximum hysteresis envelope than at integer filling factors. All these observations coincide well with the data already published by Harrison et al. [78].

While the decrease of the background magnetoresistance combined with the phase inversion are observed in both CDW_0 and CDW_x phases, the hysteresis in the magnetic torque is only observed within the CDW_x state. This shows that these two effects do not necessarily have the same origin. All proposals up to now, trying to explain the hysteretic torque, are based on dissipationless, or persistent, currents, which in turn determine a decreasing background magnetoresistance. This has been, for instance, a sliding CDW exhibiting the Fröhlich type of superconductivity [78,115], which has not been found yet in any kind of material. Another explanation was based on persistent currents due to the quantum Hall effect [112]. The latter effect has indeed been proposed in several works [42,116,117,112], whereas the arguments for it given up to now are not free of doubts. Basically the same authors, in their newest publications, have actually withdrawn already these two proposals. Currently, the arguments of Harrison et al. [118, 119] are again associated with an oscillation of the chemical potential due to the dHvA oscillations, as in the case of the frequency doubling model. The new model is based on the fact that a CDW may become pinned by lattice imperfections or impurities, that is known to be common to CDW systems [19]. Within the CDW_x state they consider an incommensurate density wave with a nesting vector, that has the possibility to adjust itself according to the (oscillating) chemical potential in order to minimize the free energy. However, as soon as the CDW becomes pinned the system is proposed to be in some kind of non-equilibrium metastable state, in which additional persistent currents may flow. These would then cause the observed hysteretic diamagnetic behaviour in magnetic field.

Whether this model is true or not, is difficult to judge now, but it certainly does not include the following, non negligible, point. We know that the hysteresis only appears within the CDW_x state. Therefore, on trying to understand the origin of the magnetic hysteresis within the CDW_x state we first point out the most important difference between the CDW_0 and CDW_x states: Within the CDW_x state the nesting vector is predicted to gradually shift in magnetic field. This will be shortly explained in a simple picture. At the kink transition ($B = B_k$) the CDW_0 state

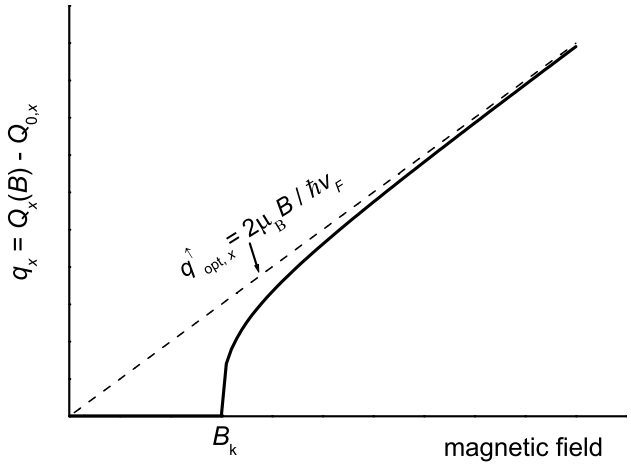

Figure 5.27: Within the CDW$_x$ state the Q_x component of the nesting vector starts to shift, in order to perfectly nest at least one of the spin-subbands [14].

becomes destroyed because free carriers appear on both spin up and down bands. Yet, this is only the case for a system that keeps a constant zero-field nesting vector. The system, however, has the possibility to take another nesting vector above B_k that has a slightly higher x-component, i.e. the component Q_x in the conducting chain direction. By doing this, the spin up band, i.e. spin $\| \overrightarrow{B}$, becomes again completely gapped, while a part of the spin down carriers become ungapped and appear again on the Fermi surface. This determines the CDW$_x$ state that was theoretically predicted to become stabilized at $T \leq 0.56\ T_{c,\text{zero-field}}$ in a perfectly nested CDW system [26, 14]. In Fig. 5.27 we sketch the proposed behaviour for the q_x-shift of the nesting vector in magnetic field [14]. At increasing the field, the CDW$_x$ wave vector asymptotically approaches the perfect nesting condition of the spin up band, that is affected by the Zeeman splitting and for the linearized dispersion relation must be given by

$$Q_x = Q_{x,0} + q_x = 2k_F + 2\frac{\mu_B B}{\hbar v_F}. \tag{5.5}$$

Note that Q_x will keep on moving with field.[3]

The above model from Harrison et al. should be extended to include the gradually changing nesting vector, that is anyway expected in the CDW$_x$ state. This then might explain the steady background found in the hysteresis, maybe indeed by the pinning of the CDW. An exact theoretical investigation on this point is highly desirable.

[3] according to newest results by P. Grigoriev there might also be the possibility of two coexisting nesting vectors, one for each spin-subband. In that case both nesting vectors will change with field.

5.2.5 Effective Mass Determination

Due to the problems with the SdH oscillations mentioned above we restrict ourselves here to the discussion of the dHvA effect. The analysis will be done for the first harmonic of the α oscillation. As shown in section 2.3 the temperature dependence of the amplitude of the quantum oscillations is directly related to the effective cyclotron mass m^*. In Fig. 5.28 the amplitudes at different temperatures and three different fields are plotted. As can be seen the fits give three different effective masses. Within the low field CDW_0 state the values appear to be slightly different and definitely lower than the one in the CDW_x state. The tendency of an increasing m^* on crossing B_k has indeed been reported in many publications [87,73,76,120,121] However, while the reported masses in the CDW_x state coincide reasonably well with each other [87,73,76,120,116], and so does ours, there is some inconsistency between the masses evaluated within the CDW_0 state, ranging inbetween 1.2-1.6 [87,73,76,120,122]. Thus even for the dHvA effect the extraction of m^* from the oscillation amplitude might not be straightforward. This suspicion becomes even stronger due to the behaviour of the effective mass on tilting the magnetic field with respect to the conducting plane. The increase of the mass with tilting the field has been found by Christ et al. [74] to be

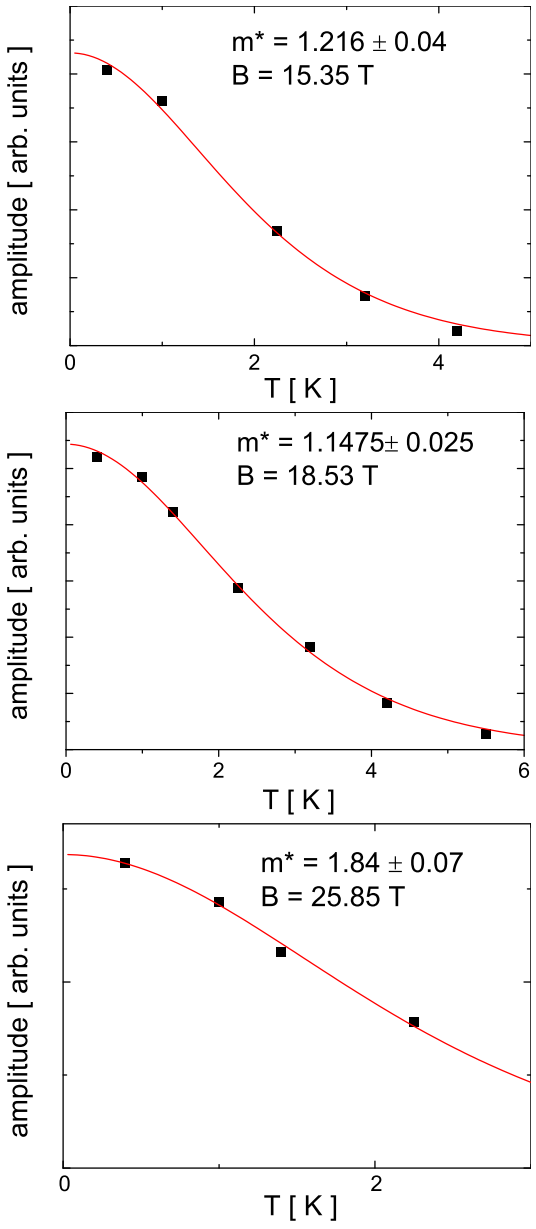

Figure 5.28: Effective mass determination from the temperature dependent amplitude of the dHvA oscillations at 3 different constant fields.

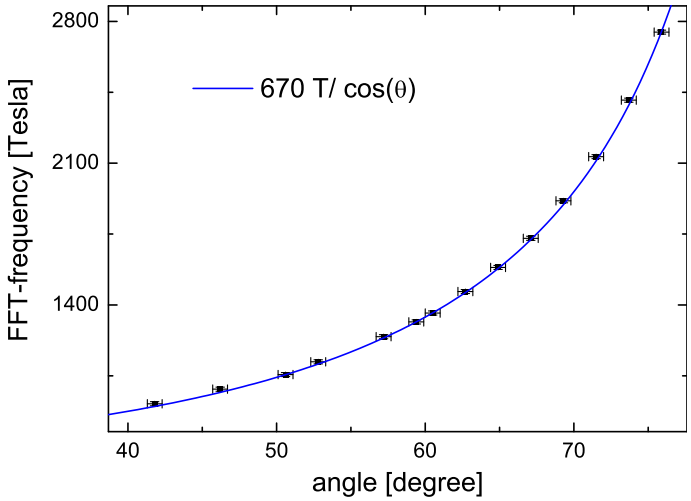

Figure 5.29: Dependence of the α-frequency on the tilting angle. The solid line is the expected $670/\cos(\theta)$ behaviour, perfectly fitting our data.

definitely stronger than the expected $1/\cos(\theta)$ law for a cylindrical Fermi surface, although the frequency exactly follows the 670 T$/\cos(\theta)$ behaviour, see Fig. 5.29. Altogether, it seems that the first harmonic of the quantum oscillation is somehow anomalously damped, especially at low temperatures at the perpendicular field direction. The reason for this remains a question at present.

Another problem related to the effective mass are different predictions concerning the angle dependent amplitude of the α-oscillation. Since the product g^*m^*, present in the spin reduction factor (see Eq. 2.28), is supposed to change with titling the field (due to the angle-dependent m^*), the amplitude should oscillate with θ. At certain angles $\cos(\frac{1}{2}p\pi g^*m^*)$ should become zero. This "spin zero" effect has been observed, for example, in α-(BEDT-TTF)$_2$NH$_4$(SCN)$_4$ [9] and was also shown to exist in the CDW$_x$ state of the present compound [123, 107]. By contrast, the data concerning the CDW$_0$ state are controversial.

In our investigations no clear oscillation of the amplitude within the CDW$_0$ state has been found. However, as we show below, reasonable results can be obtained by a direct comparison of the amplitude sign between the CDW$_x$ and CDW$_0$ states.

We start with the oscillation amplitude within the CDW$_x$ state. Open circles in Fig. 5.30 show the amplitudes extracted at different angles. The corresponding fit gives a value for g^*m^* of about 3.75 that quite well coincides with the results from other groups [123, 107]. Note, that the amplitude sign of our data could not be directly determined from the magnetic field sweep data, since this is simply not

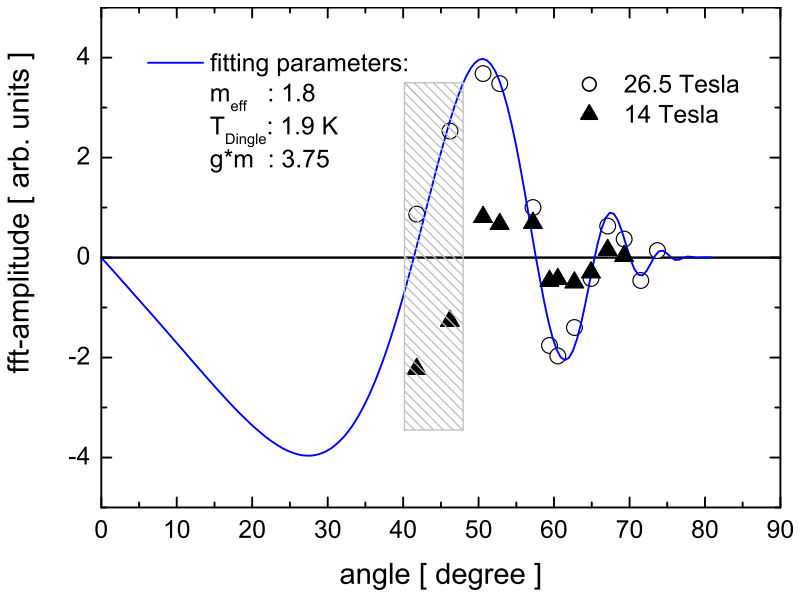

Figure 5.30: Angle dependence of the oscillatory torque amplitude at 2 different constant fields. The solid lines is a fit to the data at 26.5 T according to the Lifshitz-Kosevich formula including the spin reduction factor. The hatched area visualizes the angular range in which a phase inversion is observed on enhancing the magnetic field from 14 T to 26.5 T.

possible.[4] The good fit together with the coincidence with other groups' results, however, make us believe the sign of our data to be correctly determined. If we assume the renormalization due to the many body effects on both g^* and m^* to be rather small and take $g^* = 2$ as determined by ESR measurements [124] this would indeed give a reasonable coincidence with the effective mass determined above within the CDW_x state.

We now try to extract the corresponding g^*m^* value for the CDW_0 state by comparing the amplitude signs between the CDW_0 and CDW_x states, since a phase inversion is easily seen in the magnetic field sweep. Remarkably, the only phase inversions found in all our measurements at various different angles happened near the kink transition and were restricted to a small angular range between 40° and 50°, as visualized by the hatched area in Fig. 5.30. This was confirmed by measurements on different samples. The points plotted in Fig. 5.30 at 14 T must therefore be correct in the sign. From these points the following information can be extracted:

[4]The experimental error in the field orientation as well as in the FFT frequency does not allow a determination of the amplitude sign at high angles.

1. The extracted points at 14 T definitely cannot be fitted by the standard Lifshitz-Kosevich model over the whole angular range. This might explain the inconsistency in the g^*m^* values observed by different groups [123, 107].

2. At lower angles, assuming $g^* \approx 2$ to be fulfilled, m^* in the CDW_0 state is definitely lower than in the high field CDW_x state. This coincides with the observed enhancement of m^* on crossing B_k.

3. In the high angle range, $\theta > 60°$, both masses above and below B_k must be very close to each other. Otherwise we would have further changes in the sign of the amplitude at sweeping the field, which, however, is not observed.

Summarizing, the effective mass at 14 T indeed seems to change, on tilting the magnetic field, stronger than the expected $1/\cos(\theta)$ behaviour. As we will show later in this thesis (section 5.4), it is very likely that at a certain tilt angle there is a phase transition that would actually explain the third point from above.

5.3 The Re-Entrant CDW State

5.3.1 Stabilization of the CDW in Magnetic Field

The B-T phase diagrams presented in section 5.1, have shown that hydrostatic pressure is a parameter that tunes the nesting conditions of the density wave remarkably well. The critical pressure P_0, at which the density wave transition temperature at zero-field becomes 0 K, was estimated to be about 2.5 $\pm$ 0.1 kbar. Above P_0 we expect the CDW state only to become stabilized via the orbital effect of magnetic field. This field-induced state corresponding to $t_c' > t_c'^*$ we call re-entrant CDW state. In this section we point out the changes seen in the magnetoresistance which occur on crossing P_0. In particular we give further experimental evidence that the CDW is really suppressed at low fields and reappears at higher fields at $P > P_0$. As before the field is directed in the interlayer direction.

Fig. 5.31 shows magnetic field sweeps up to 15 T at the lowest possible temperature of our experimental setup, for different pressures covering the whole pressure range investigated within this work. The data presented in Fig. 5.31 are obtained on the same sample and have been qualitatively reproduced on another one measured at the same time. At $P < 2.5$ kbar we expect the density wave to exist at zero-field. The decrease of the maximum in the semiclassical resistance with pressure we attribute to a reduced breakdown gap on the reconstructed Fermi surface due to the worsening of the nesting conditions. The carriers have a higher probability to tunnel between the open and closed parts of the Fermi surface that causes the magnetoresistance, dominated by the motion of the carriers along the open sheets, to become reduced [85]. This then also explains the fact that the maximum of the magnetoresistance at 1.5 kbar and 2 kbar is found at ≈ 7.5 T that is clearly below the ambient pressure value of $\approx$ 11 T. However, we still consider the carriers to mainly run on the Q1D sheets of the reconstructed Fermi surface thus providing a rather strong magnetoresistance.

Remarkably, distinct changes occur in the field sweeps on crossing P_0. What is immediately recognized are rather slow oscillations of the background resistance starting from $P = 2.5$ kbar. With pressure these oscillations move gradually to higher fields as visualized by dashed lines in Fig. 5.31.

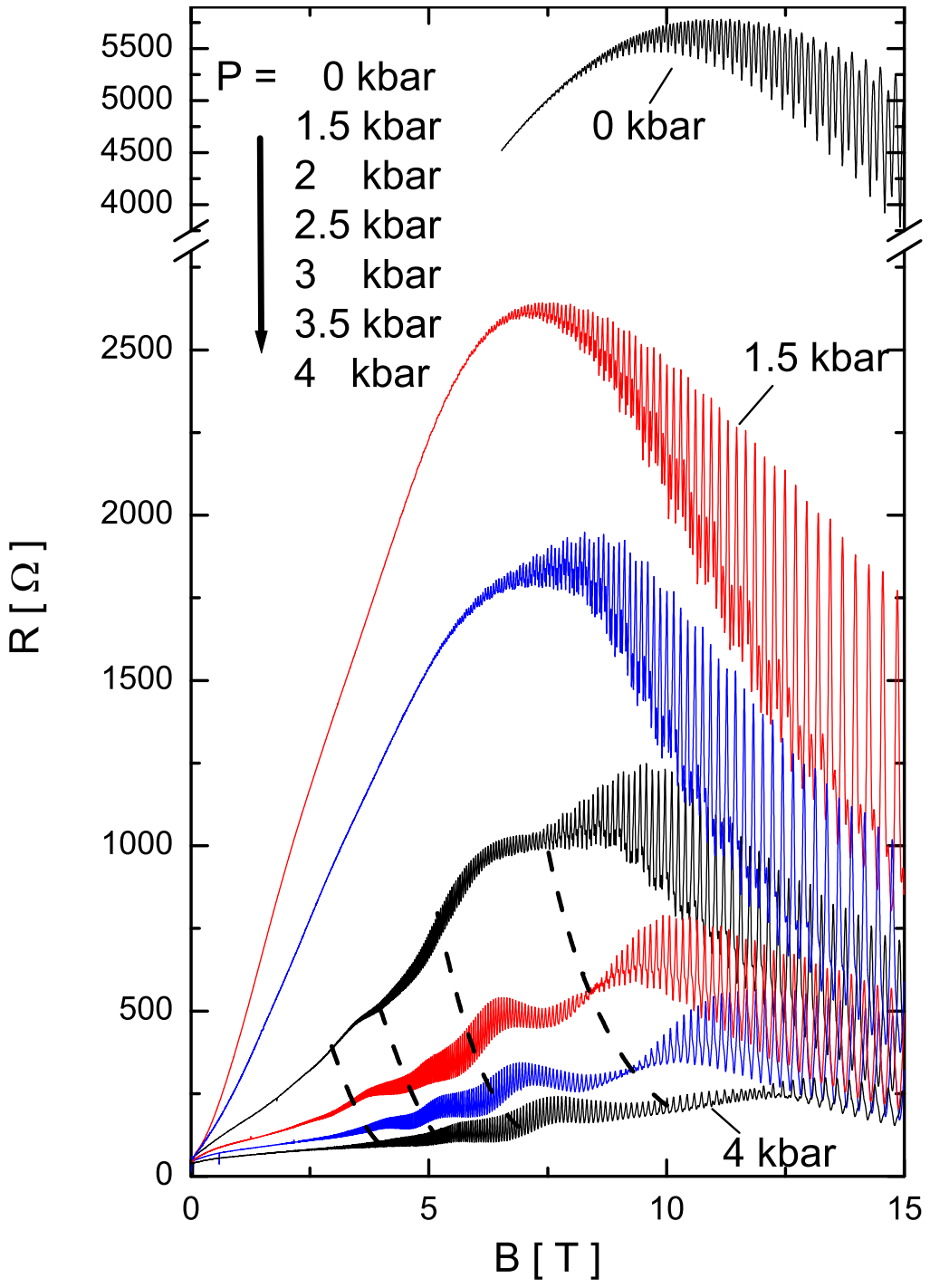

Figure 5.31: Isothermal magnetoresistance at various pressures at 100 mK. Above $P_0 \approx 2.5$ kbar slow oscillations appear in the background magnetoresistance. With pressure these oscillations move to higher fields as visualized by dashed lines.

Concerning the fast oscillations (from the α orbit), they start to appear with field, at P $<$ 2.5 kbar, shortly before the background reaches a maximum, also in line with the magnetic breakdown model. With increasing pressure above the critical value of 2.5 kbar the fast oscillations exist, at 100 mK, already at much lower fields of about 2 T that is shown in Fig. 5.32. Obviously, the magnetic breakdown gap in this pressure and field range dramatically decreases or even vanishes, that may be due to the presence of the NM state at low fields.

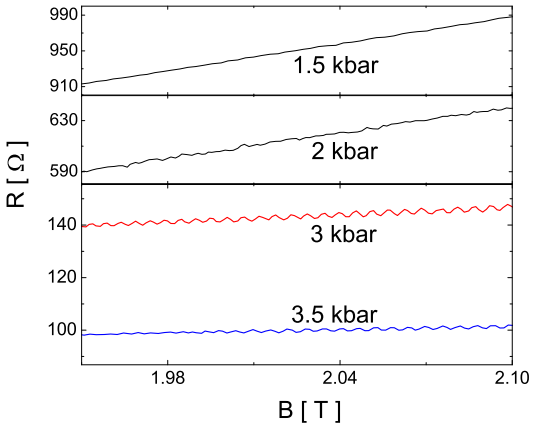

Figure 5.32: Above 2.5 kbar the fast oscillations start to appear already below 2 T, at 100 mK.

This assumption is supported by the isothermal field sweeps at different temperatures. In Fig. 5.33 the curves measured at 3 kbar are shown. At 4.2 K there is a moderately increasing magnetoresistance with no sign of any transition. We therefore consider the normal metallic state at this temperature to be present over the whole field range. At 2.5 K, the stronger enhancement of the resistance starting from 6 T we again ascribe to the formation of a CDW. These two curves resemble those discussed in section 5.1.2 in Fig. 5.10 for 2.3 kbar at higher temperatures, 3.6 K and 5 K. The orbital effect stabilizes the density wave state in a certain field range. With lowering the temperature the enhancement of the resistance then also appears at lower fields. Remarkably, this increase seems to occur step-wise and somehow to be correlated with the slow oscillations of the background. This already strongly suggests the slow oscillations to only occur within the re-entrant CDW state. Within the whole temperature range the slope of the magnetoresistance below 2 T remains approximately the same. Moreover, in this field range the resistance is nearly temperature independent as can be seen in Fig. 5.34. Thus, we propose the normal metallic state to exist at low fields, at least down to 100 mK. This then also explains the low starting field of the α-oscillations, Fig. 5.32. As we shall see below, further evidence for the existence of the normal metallic state at low fields is given in the studies of the angle dependent magnetoresistance (section 5.3.4) as well as in the studies of competing phases at low fields, section(5.5).

The presence of the re-entrant CDW state at higher fields is directly reflected in its

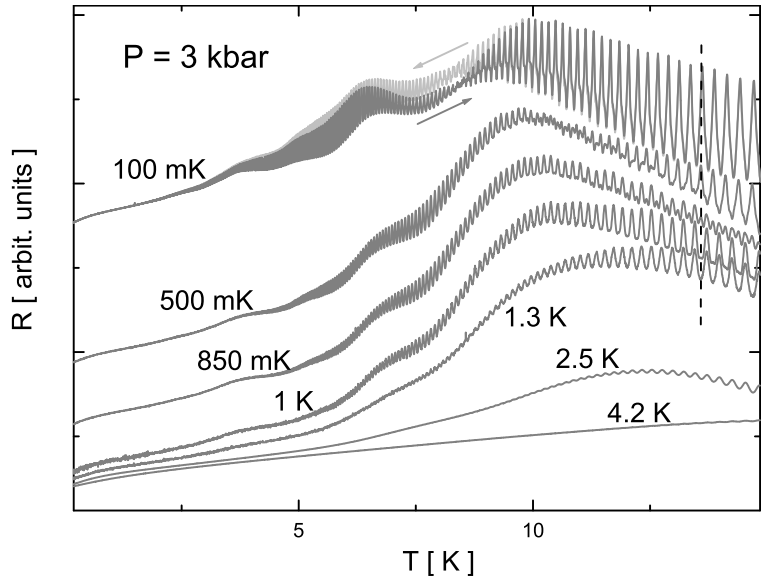

Figure 5.33: Isothermal magnetoresistance recorded at increasing field at different temperatures and P = 3 kbar. The curves are offset from each other. At the lowest temperature the down sweep is additionally shown in light grey. The dashed line visualizes the phase inversion of the fast SdH oscillations occurring at low temperatures.

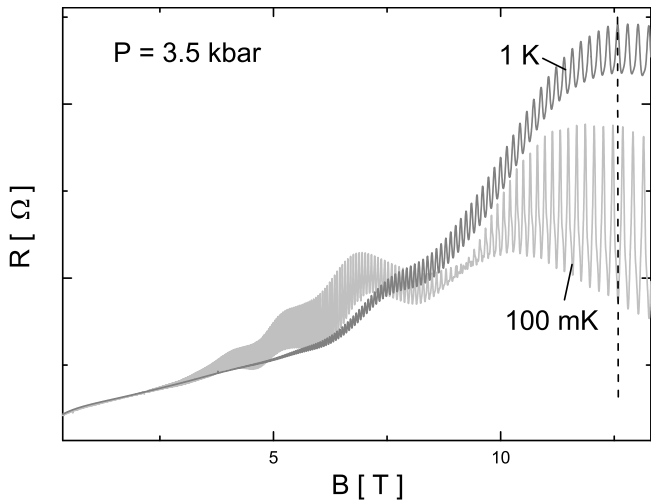

Figure 5.34: Isothermal magnetoresistance recorded at two different temperatures and P = 3.5 kbar. The dashed line again illustrates the phase inversion. Note the temperature independent resistance at low fields, suggesting the NM state to be present.

distinct properties. First, in the field range of 10-15 T the additional SdH frequencies λ and ν remain. An example of the FFT spectrum at 3.5 kbar is given in Fig. 5.35. Second, there is a broad hysteresis observed on up- and down- sweeps at $B \gtrsim 3$ T. This is shown for the lowest temperature in Fig. 5.33. Third, there is a strong decrease of the background magnetoresistance observed on lowering the temperature (Fig. 5.34). This is again combined with a phase inversion of the fast oscillations as marked in Fig. 5.33 and Fig. 5.34 for 3 and 3.5 kbar, respectively, by vertical dashed lines. Such a behaviour is typical for the CDW state as was presented in section 5.2 at ambient pressure.

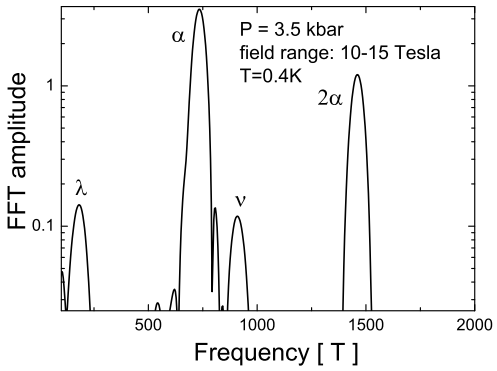

Figure 5.35: The additional frequencies within the CDW state are clearly resolved at $P = 3.5$ kbar.

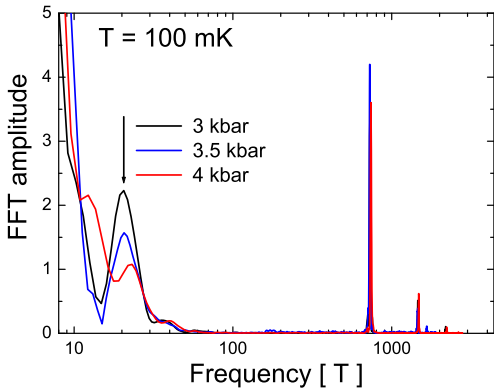

Figure 5.36: FFT spectrum of the whole measured field range; 2-15 T. The slow oscillations are reflected by an additional peak at ≈ 20 T

Altogether, the re-entrance to the CDW state in magnetic field is clearly seen in the magnetoresistance data and the observed behaviour fits very well to the proposed model by Zanchi et al. [14], Fig. 5.12.

Still the question remains why these slow oscillations appear within the re-entrant CDW state. At first glance one can imagine that they emerge due to small pockets on the reconstructed Fermi surface. This would give a SdH signal of a very low frequency in $1/B$. Indeed, a FFT transformation of the whole field range within the re-entrant CDW state shows a peak at about 20 T. The spectra of the oscillations given in Fig. 5.31 are shown in Fig. 5.36. Since these peaks are deduced from only very few oscillation periods it is hard to judge about their exact positions. Moreover, since the background resistance in the re-entrant state is not known and was evaluated by a low order polynomial fit, an artificial shift of the peak positions (of the order of tesla) in the FFT spectrum might arise. We therefore cannot judge about a pressure

dependence of the low frequency. Nevertheless, a periodicity of these oscillations in $1/B$ is clearly reflected.

Actually, within the re-entrant CDW state Zanchi et al. [14] have predicted successive field-induced transitions between CDW subphases with different nesting vectors to occur. The origin of these subphases is indeed due to the partial ungapping of the Q1D carriers, which then form small pockets on the initial Q1D part of the Fermi surface [22,125,126,127]. To optimize the free energy of the system the nesting vector then starts to shift due to the Landau quantization of the small pockets [128]. At low temperatures this leads to quantized jumps of the nesting vector that determines first order transitions between the CDW subphases [129]. These transitions are similar to already well known field-induced SDW transitions [22,128,5,2] which have been, and still are, a subject of intense interest in the field of organic conductors. Before proceeding further with the experimental data we will first give an introduction to these phenomena.

5.3.2 Model of Field-Induced CDW Transitions

The qualitative consideration is first carried out for the well understood field-induced SDW transitions (FISDW). For a detailed theoretical treatment the reader is referred to the textbook of Ishiguro, Yamaji and Saito [2] on organic superconductors and references therein. After that, the model is extended for CDW systems and consequences of the additional Pauli effect of magnetic field will be discussed. Lebed working in close collaboration with our group and inspired by the results presented above confirmed this simple consideration in an exact theoretical investigation [129].

We consider the k_y-dependence of the band energy for an electron dispersion defined in section 5.1.1:

$$\epsilon_{\mathbf{k}} = \hbar v_F(\mid k_x \mid -k_F) - 2t_y \cos(k_y \mathrm{a}_y) - 2t'_y \cos(2k_y \mathrm{a}_y). \tag{5.6}$$

The conducting chains are running along the x-direction and a_y is the interchain lattice constant. In Fig. 5.37 we sketch the energy of the upper and lower bands for $t'_y > t'^*_y$. The picture implies that the density wave exists in magnetic field. The effective gap is suppressed and a semi-metallic spectrum is observed. The reconstructed Fermi surface thus contains small pockets of electron and hole-like carriers. In magnetic field these pockets are Landau quantized (dotted lines in Fig. 5.37). If then the chemical potential μ happens to lie in-between the quantized

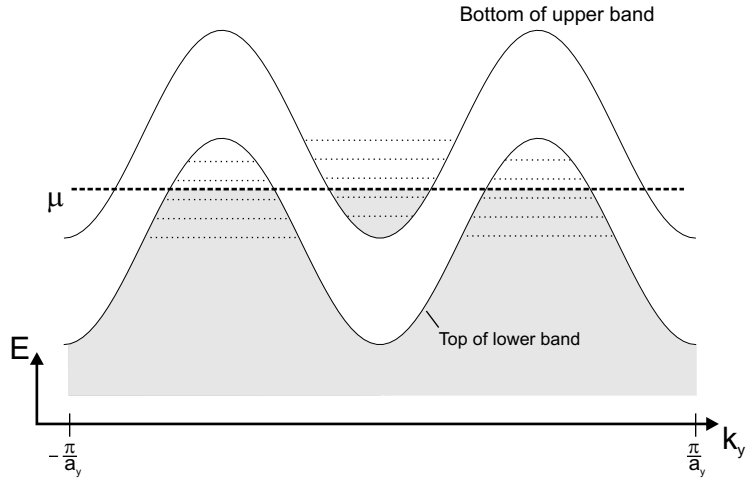

Figure 5.37: Upper and lower energy bands for $t'_y > t'^*_y$. The density wave only exists at high enough magnetic fields. The spectrum then becomes semi-metallic and Landau quantized (dotted lines).

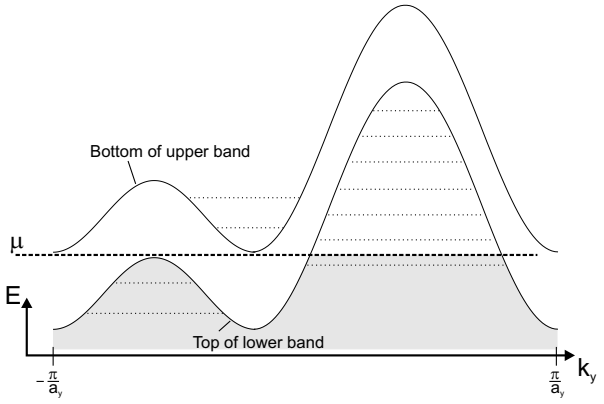

Figure 5.38: By shifting the nesting vector in k_y direction, the system completely gaps one type (here: electron-like) of carriers.

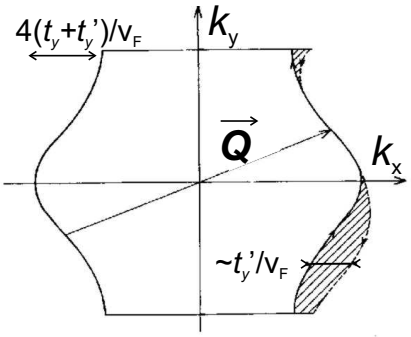

Figure 5.39: Only a part of the Fermi surface becomes nested, from [126].

levels the carriers become again effectively gapped and the system gains energy [22, 128, 5]. However, with increasing the magnetic field the Landau levels move and start crossing the Fermi level. In order to prevent this the system has now the possibility to adjust the pocket size of both carrier types by shifting the k_x component of the nesting vector, Q_x. Thus, with increasing the magnetic field the nesting vector steadily moves, so that the chemical potential is always kept in the middle of the gap between the Landau levels, until at a certain field an abrupt change of the nesting vector occurs, placing the chemical potential between the following pair of Landau levels. This determines the successive field-induced transitions between SDW subphases. An exact theoretical treatment [130] shows that it is most favorable not only to change Q_x but also Q_y . This is also easily understood by considering a sketch of the electron bands where the nesting vector is shifted in k_y-direction, shown in Fig. 5.38: By doing this, it is possible to again completely gap one type of the carriers while the other remains quantized in field. Which carriers (hole or electron like) disappear depends on the sign of the q_y-shift. The resulting pockets on Fermi surface are visualized in Fig. 5.39. Altogether the most important consequence of the exact theoretical consideration is a quantization condition for the Q_x component of the nesting vector that can be expressed by [22, 125, 126, 131, 132]:

$$Q_x = Q_{x,0} + q_x = 2k_F + N \cdot \frac{2ea_yB_z}{\hbar} \tag{5.7}$$

with N being an integer number, $Q_{x,0} = 2k_F$ being the nesting vector of a perfectly nested system ($t'_y = 0$) and B_z the magnetic field component perpendicular to the layers. The possible quantized values are sketched in Fig. 5.40.

Due to the above scenario several peculiarities occur in SDW systems in the pressure range where the zero-field transition temperature is already completely suppressed:

- The re-entrant SDW state in magnetic field always contains several subphases with different nesting vectors (at a given field only one subphase exists).
- The transitions between the subphases scale approximately in $1/B$.
- At low enough temperatures, first order transitions emerge [22, 125, 130, 126] due to the jumps of the nesting vector. The temperature at which they start, strongly depends on the coupling constant of the density wave [132, 133], i.e. the transition temperature of the SDW state at the given field.

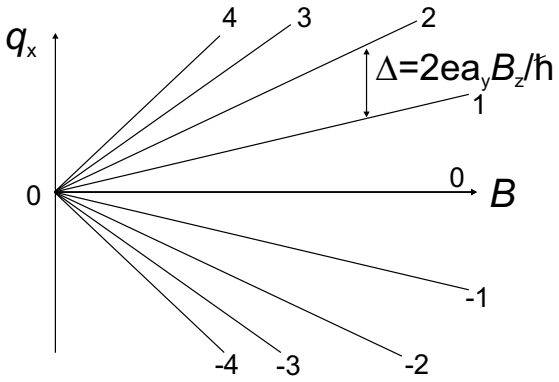

Figure 5.40: The q_x-shift of the nesting vector becomes quantized at low temperatures

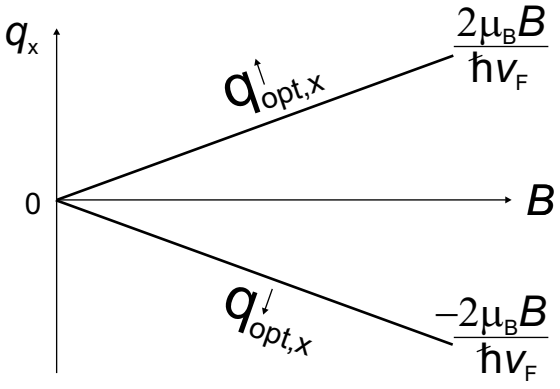

Figure 5.41: The perfect nesting vector differs in magnetic field for the two spin-subbands. Here, the relative shifts for both spin directions with respect to the zero-field nesting vector are shown.

- Due to the fact that the FISDW subphases only contain completely filled Landau levels, there exists a quantized Hall effect with the Hall resistivity given by:

$$\rho_{xy} = \frac{h}{2Ne^2}, \tag{5.8}$$

with N being an integer number, corresponding to the highest filled Landau level. Remarkably, this quantized Hall effect occurs in a bulk material.

Indeed, all these consequences have been experimentally verified in the organic SDW compound $(TMTSF)_2PF_6$. In Fig. 5.42 the results of Kornilov et al. [134] and Kang et al. [33, 5] are depicted, showing field sweeps of the magnetoresistance, phase diagrams with FISDW transitions at two different pressures and the quantized Hall resistance. The hysteretic behaviour found in the up and down sweeps of magnetic field reveals the first order transitions at low temperatures. Note that the FISDW transition fields are slightly temperature dependent.

Switching now to the CDW system we adopt the qualitative description given above and additionally take into account the Pauli effect of magnetic field. The important difference is that for a CDW system the perfect nesting vector differs for the subbands with opposite spin directions. For each subband the quantization condition given by Eq. (5.7) holds, only that the Fermi wave vector k_F becomes field dependent.

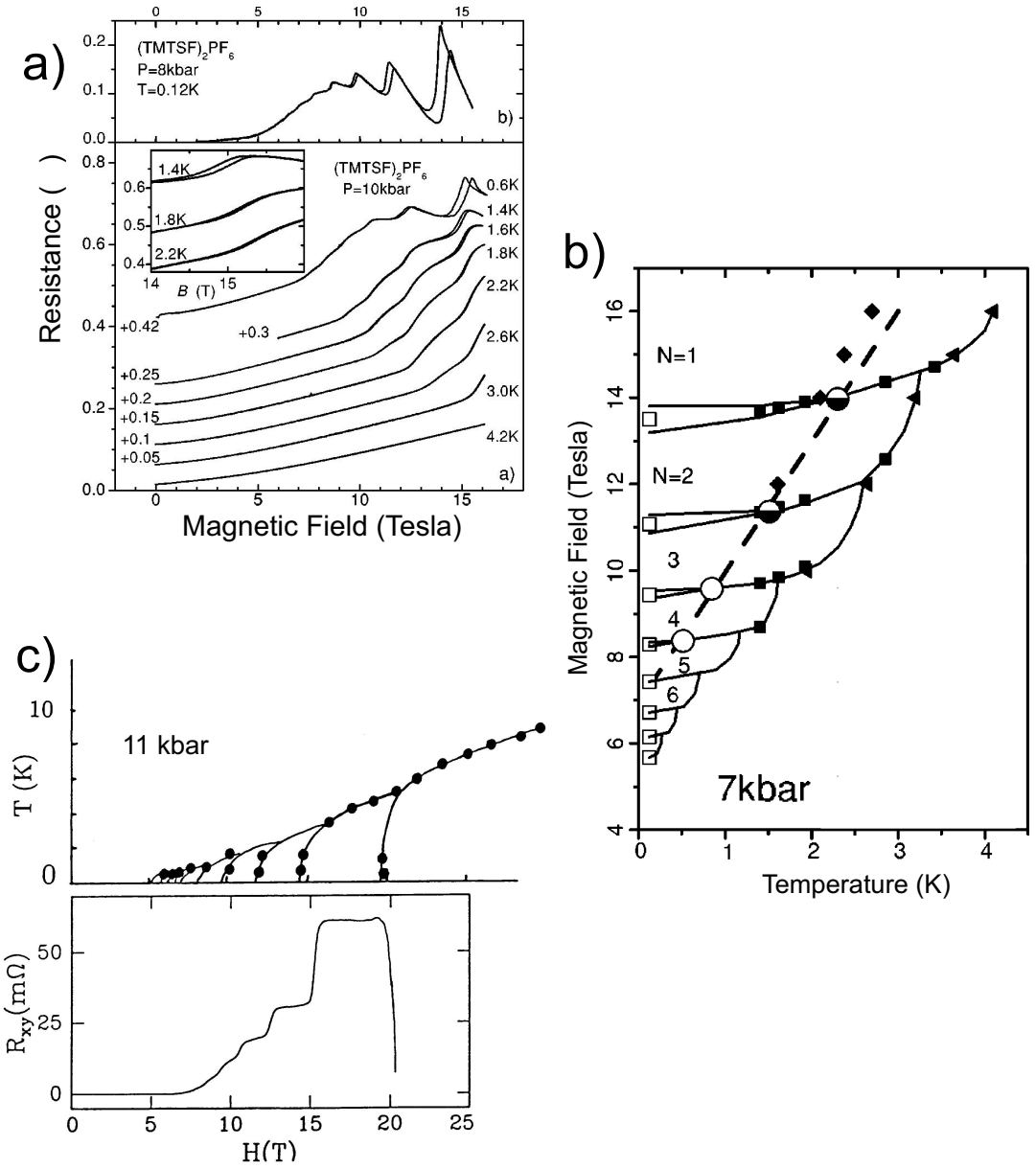

Figure 5.42: Data observed in the FISDW pressure regime of $(TMTSF)_2PF_6$: a) Field sweeps of the magnetoresistance at different T. A pronounced hysteresis at low temperatures determines the first order FISDW transitions, from [134]. b) Phase diagram determined by Kornilov et al. [134]. The split lines below the dashed curve mark the hysteretic region of the first order transitions. c) Quantized Hall resistance and phase lines at higher pressure determined by Kang et al. [135, 5]

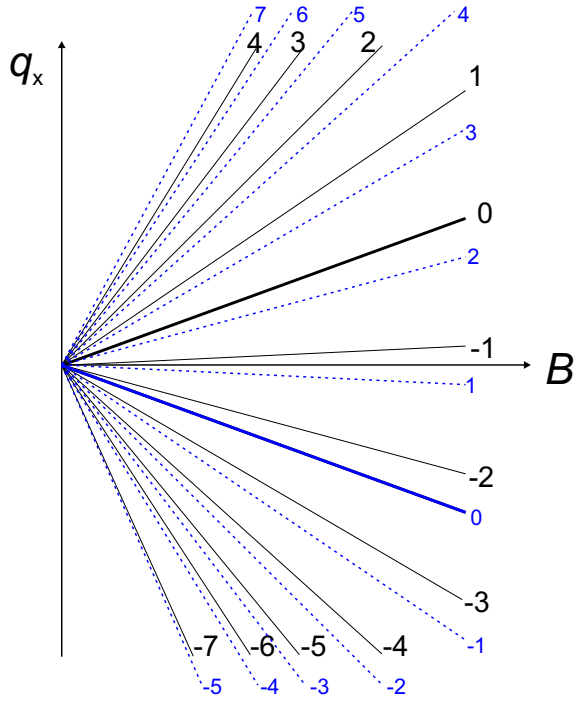

Figure 5.43: The resulting quantization spectrum for the nesting vector after superposing the Pauli effect (Fig. 5.41) and the orbital quantization (Fig. 5.40).

With a dispersion relation linearized in k_x at the Fermi level the shift of the perfect nesting vector in k_x-direction with respect to the zero-field vector is then given by:

$$Q_{x,\text{Pauli}} - Q_{x,0} \equiv q_{x,\text{Pauli}} = \pm\frac{2\mu_B B}{\hbar v_F}, \tag{5.9}$$

the sign on the right side depends on the spin direction, Fig. 5.41. The complete quantization spectrum of possible q_x-shifts is then written as

$$q_{x,\text{full}} = q_{x,\text{Pauli}} + q_{x,\text{quant}} = \pm\frac{2\mu_B B}{\hbar v_F} \pm N \cdot \frac{e2\mathrm{a}_y B_z}{\hbar}. \tag{5.10}$$

This equation is visualized in Fig. 5.43. With increasing field, Q_x should take successively lower N-values. Which quantized level in what field range the nesting vector takes, we cannot judge at the present moment, since a detailed theoretical investigation on this point is still missing.

Note, that the Pauli splitting is an isotropic effect while the quantization only depends on the perpendicular field component. This means that, with tilting the field towards the conducting plane, the quantized values move closer to each other

but the distance between the states with $N = 0$ for both subbands remain the same. At certain angles one therefore expects the quantized spin up levels to coincide with the spin down ones. At these so-called "commensurate" angles the density wave is predicted to become stabilized at higher temperatures [129].

5.3.3 Field-Induced CDW at Different Pressures

Up to now, we have verified that above 2.5 kbar the CDW is re-established in magnetic field, while it is very likely completely suppressed at zero field. The observed slow oscillations thus exactly appear in the pressure, field and temperature region in which the re-entrant CDW state, and with it the FICDW transitions, are expected. Within the re-entrant CDW state, the nesting vector is supposed to slowly oscillate with field at higher temperatures, while at low temperatures it jumps from one quantized level to the other [129]. Below several arguments will be pointed out why the observed slow oscillations cannot be attributed to the conventional SdH effect, but rather to this new quantum phenomenon:

1. Indeed, at 3 kbar and 100 mK, Fig. 5.44, a clear structure is observed in the

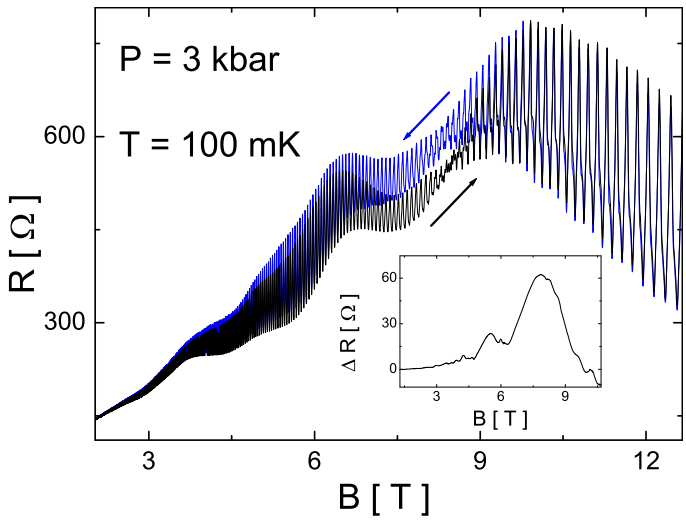

Figure 5.44: Up (black) and down (blue) field sweeps of the magnetoresistance at $P = 3$ kbar and $T = 100$ mK. The hysteresis, observed by subtracting one curve from the other, is given in the inset. A clear structure matching the oscillatory features can be seen.

hysteresis in the up and down field sweeps that correlates with the slow oscillations. To determine the hysteresis, the fast oscillations were filtered out from these curves. As can be seen in the inset of Fig. 5.44 the hysteresis exhibits clear maxima at approximately the field positions where the background magnetoresistance has a maximum curvature with respect to magnetic field. This observation we regard as the first sign for the expected first order transitions between the subphases. Unfortunately, our cooling system did not allow us to go to even lower temperature on ramping to such high magnetic fields, so that this is the only clear hysteretic structure observed in our measurement at the perpendicular field direction. Unlike the sharp hysteretic transitions seen at the FISDW transitions, Fig. 5.42, the peaks in our compound are very broad. Obviously, the first order transitions start to appear at much lower temperature (with respect to the re-entrant CDW transition temperature at a given field) in comparison to the FISDW case. This, however, should be expected, since in FICDW the quantized values of the nesting vector for different spin directions at perpendicular magnetic field likely do not match each other. This will directly lead to a lower coupling constant and, hence,to a lower transition temperature of the re-entrant CDW as well as a lower starting temperature of the first order transitions [129].

2. Another peculiarity of the slow oscillations is shown in Fig. 5.45. On lowering the temperature it is obvious that the phase of the oscillations is temperature dependent. To illustrate this, dashed lines are placed into Fig. 5.45 approximately following the maximum curvature of the slow oscillations. This anomalous behaviour is certainly not expected for normal quantum oscillations and to the moment we attribute this finding to the new quantum phenomenon of FICDW transitions.

   In analogy to the FISDW, we now determine B-T phase diagrams for the present FICDW case. To extract transition points between different CDW subphases from the background magnetoresistance the fast oscillations have been filtered out as shown in Fig. 5.45. As a transition field we choose the points of maximum curvature in the field sweeps, since (i) they coincide very well with the observed peaks in the hysteresis (Fig. 5.44) and (ii) are reasonable if one expects a change of the nesting vector to improve the nesting conditions, and with it to enhance the magnetoresistance. We therefore assume the real transition fields to behave in a similar manner as the extracted points. Fig. 5.46 shows the observed phase diagrams in the re-entrant CDW

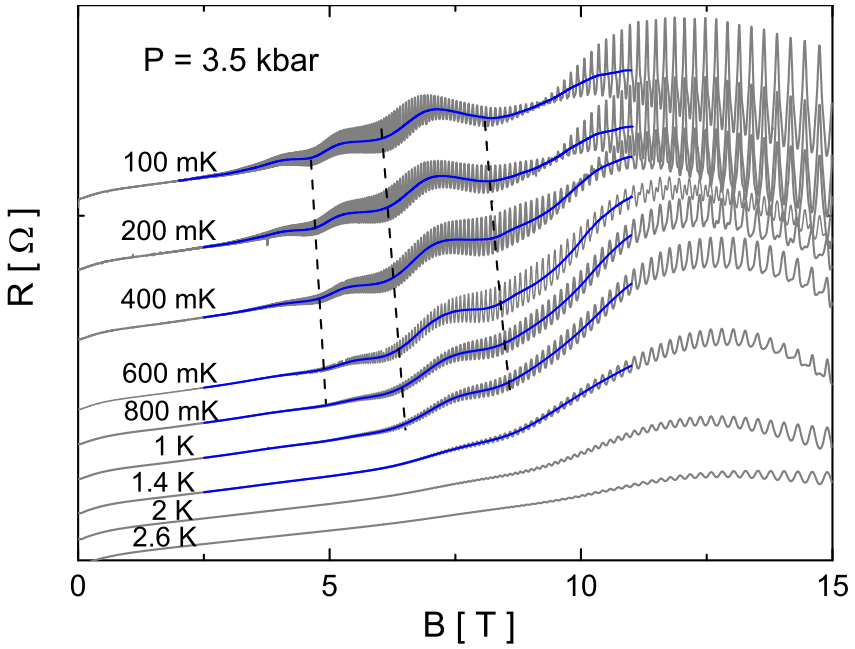

Figure 5.45: Field dependence of the magnetoresistance at various different temperatures and 3.5 kbar. The curves are offset from each other. The blue lines determine the background resitance, obtained by filtering out the (fast) SdH oscillations. As visualized by the dotted lines, the extremal points of the slow oscillations change their field positions with temperature.

state for all pressures studied. The dashed lines are guides for the eye and simulate the expected phase lines by comparison with the phase diagrams shown in Fig. 5.12 and Fig. 5.11. Obviously, there is a tendency of the transition points to move to higher fields on increasing the temperature. Whether this should really be the case in FICDW we do not know at present, since no exact theoretical investigations have been done yet. The observed phase diagrams, however, appear to be very similar to those of FISDW compounds, compare with Fig. 5.42, where a temperature dependence of the transition points has been experimentally verified [134]. The only difference in FICDW is the eventual suppression of the transition temperature at high fields due to the Pauli impact on the system. Since the transitions at different fields definitely show different temperature dependencies this also gives a strong argument for the slow oscillations not to be caused by the conventional SdH effect.

3. Another feature very similar to that of the FISDW is illustrated in Fig. 5.47: the extracted phase transitions at 100 mK move to higher fields with enhanc-

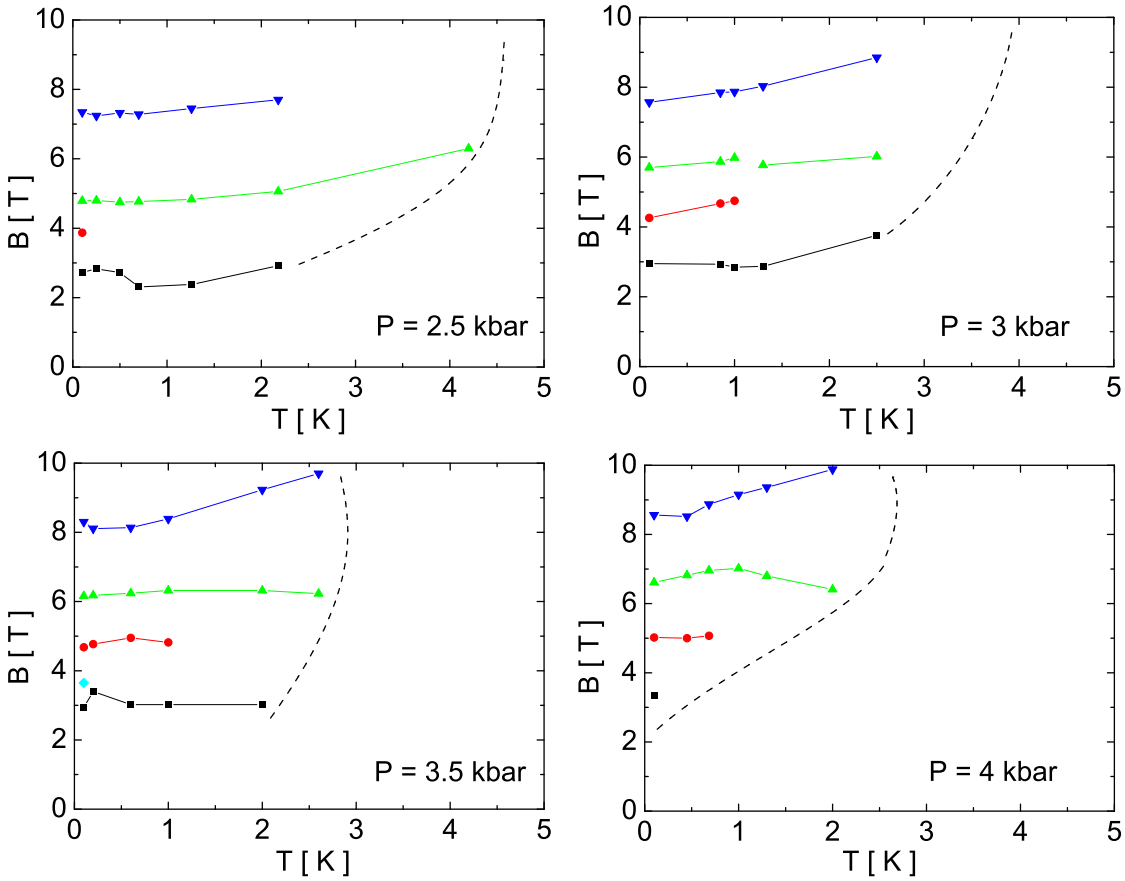

Figure 5.46: FICDW transition points for different pressures. Dashed lines simulate the phase boundaries, the transition points are determined from the maximum curvature of the background resistance

ing the pressure. This can be easily understood, since the quantization of the nesting vector, periodic in inverse field, is determined by the the small pockets developing on the imperfectly nested Fermi surface. These pockets will increase with pressure. It is therefore clear that with pressure, as for the normal quantum oscillation, a higher field will be necessary to reach the same quantum number. Note, however, that the increase of the transition fields with hydrostatic pressure is quite strong, corresponding to an increase of the FS orbit area of about 20%/kbar. For conventional SdH oscillation such a strong increase should be clearly resolved in the FFT spectrum. Since this is not the case here, this gives another argument against the SdH effect being the reason

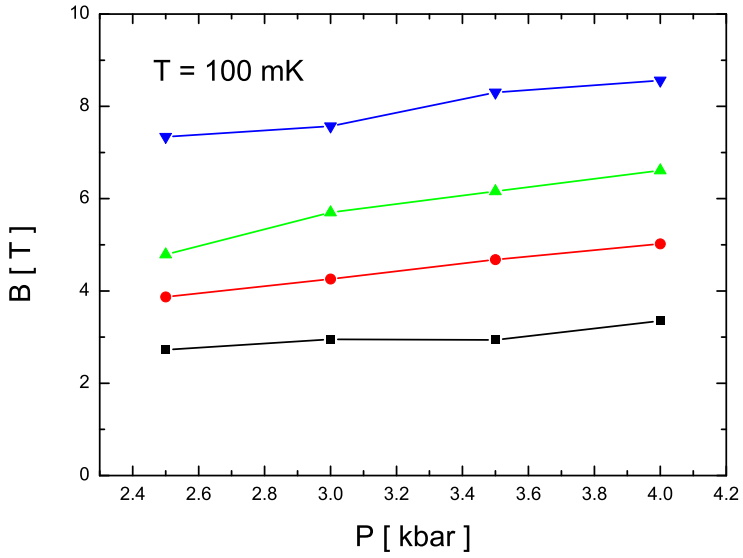

Figure 5.47: With pressure the extracted FICDW transition points at 100 mK move to higher magnetic fields.

for the observed slow oscillations.

One of the most direct signatures of field-induced density wave transitions is the quantization of the Hall resistance. We have performed first measurements, but failed, however, to observe any modulation of the Hall resistance. Besides the fact that we did not go to very low temperatures but only to 1.4 K, the present compound turned out to have several problematic properties. The Hall effect seems to be dominated by the additional Q2D part of the Fermi surface. The quantization of the Q1D contribution will thus be very difficult to extract. Furthermore, the sample geometry is not in favor of Hall measurements: The samples are typically very small quadratic plates (0.5×0.5 mm^2) with the crystal axes running along the diagonals. Nevertheless, at lower temperatures changes in the Hall resistance due to the electrons on the small quantized orbits must be much more pronounced. Therefore, in spite of the above mentioned difficulties measurements at lower temperatures might resolve FICDW effects and remain to be done.

At the end we note that a modulation of the SdH oscillation amplitude of the α-frequency in the FICDW states is observed (see Fig. 5.45). Its nature, however, is unclear at present. No correlation of the modulation with the FICDW transitions has been found so far. Further measurements are needed to draw any reliable

conclusions.

5.3.4 Angle Dependent Magnetoresistance

In view of the results, presented up to now within this section, there are two main reasons for studying the angle dependent magnetoresistance.

The first one emerges due to the present transition from the NM state to the re-entrant CDW state in magnetic field at $P \gtrsim P_0$. This transition might also be reflected in AMRO measurements. At ambient pressure the AMROs in the CDW state are known to strongly differ from the ones in the NM state: while the former are typical of a Q1D electron system the latter show the Q2D behaviour (see section 3.4). Since we have seen that within the re-entrant CDW state the semiclassical magnetoresistance is still remarkably high over a wide field range, one can expect signs of the 1D AMROs to occur.

The second reason concerns the field-induced density wave transitions in magnetic field. As mentioned above the orbital quantization only depends on the magnetic field component perpendicular to the layer, B_z. On the other hand the Pauli effect is known to be isotropic. Hence, on tilting the field there must be certain "commensurate" directions at which the quantized levels of the nesting vector for the spin up and spin down bands match each other (the quantum numbers of the different bands always being different). At such angles one thus expects optimal conditions for the FICDW transitions. Indeed, Lebed predicted that at these commensurate angles both the transition temperature of the re-entrant CDW at a given field and the starting temperature of the first order transitions with field must become enhanced. In addition, a "peak-effect" can be expected in the AMRO at these commensurate angles, since there the CDW is stabilized already at higher temperatures.

For these measurements a small pressure cell was mounted on the newly constructed two axes rotation insert, which allowed the sample to be cooled down to 0.4 K in a ^{3}He cooling system. For continuous rotation at a reasonable speed, necessary for AMRO measurements, the lowest possible temperature was 0.7 K. The definition of the angles θ and φ of the sample position with respect to the field is depicted in Fig. 5.48.

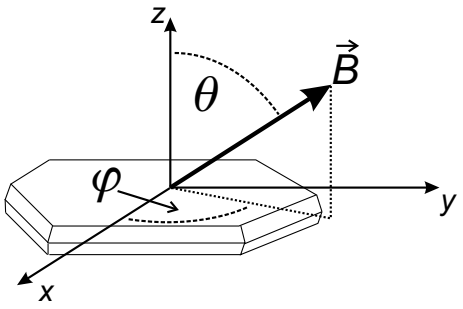

Figure 5.48: Definition of the angles determining the field direction with respect to the sample.

In order to give further evidence for the stabilization of the re-entrant CDW in magnetic field, AMRO experiments at $P = 3.8$ kbar have been performed. Two sets of AMROs, scaled in $\tan(\theta)$, at several constant fields and two different temperatures are shown in Fig. 5.49. From these curves several important properties can be extracted. At low fields, the AMROs are clearly of Q2D type, a further evidence that the NM state is present here. To directly show this, polynomial fits of second order have been subtracted from the 3 T curve at 0.8 K and the 5.5 T curve at 1.5 K, which is shown in Fig. 5.50. A periodicity of the maxima is clearly seen. On enhancing the field, see 10.5 T in Fig. 5.51, a pronounced increase of the semiclassical resistance is found at low angles. Further, in the same curve the position of the first maximum is found to be shifted. This definitely contradicts the Q2D model but would be in line with the Q1D AMROs of the CDW state. At higher angles the maxima then again fit very well with those at lower fields. This suggests that there is also a transition from the CDW to the NM state at these field values on tilting the sample. This can be expected, since the the transition to the re-entrant CDW state only depends on the perpendicular field-component.

At higher fields there is strong magnetic breakdown and it again becomes hard to distinguish between different states. At low angles the maxima do, however, not coincide with those at low fields as can be seen from Fig. 5.49. We therefore conclude that the CDW exists above a threshold field and within a certain angular range.

The proposed additional peaks at the commensurate angles could not be observed. This may be due to the fact that the peaks from the AMROs for the given inplane angle φ are lying very close to the commensurate field directions. However, we note that on changing the angle φ the expected FICDW AMRO peaks may become resolvable.

Now we turn to the FICDW transitions at different directions of magnetic field. In Fig. 5.52 we show magnetic field sweeps at different angles in the angular range $\theta = 50° - 60°$ at 2.8 kbar, scaled in $\cos(\theta)$. The curves are offset for clarity. The black curves are taken on sweeping the field up, grey curves on sweeping down. Obviously,

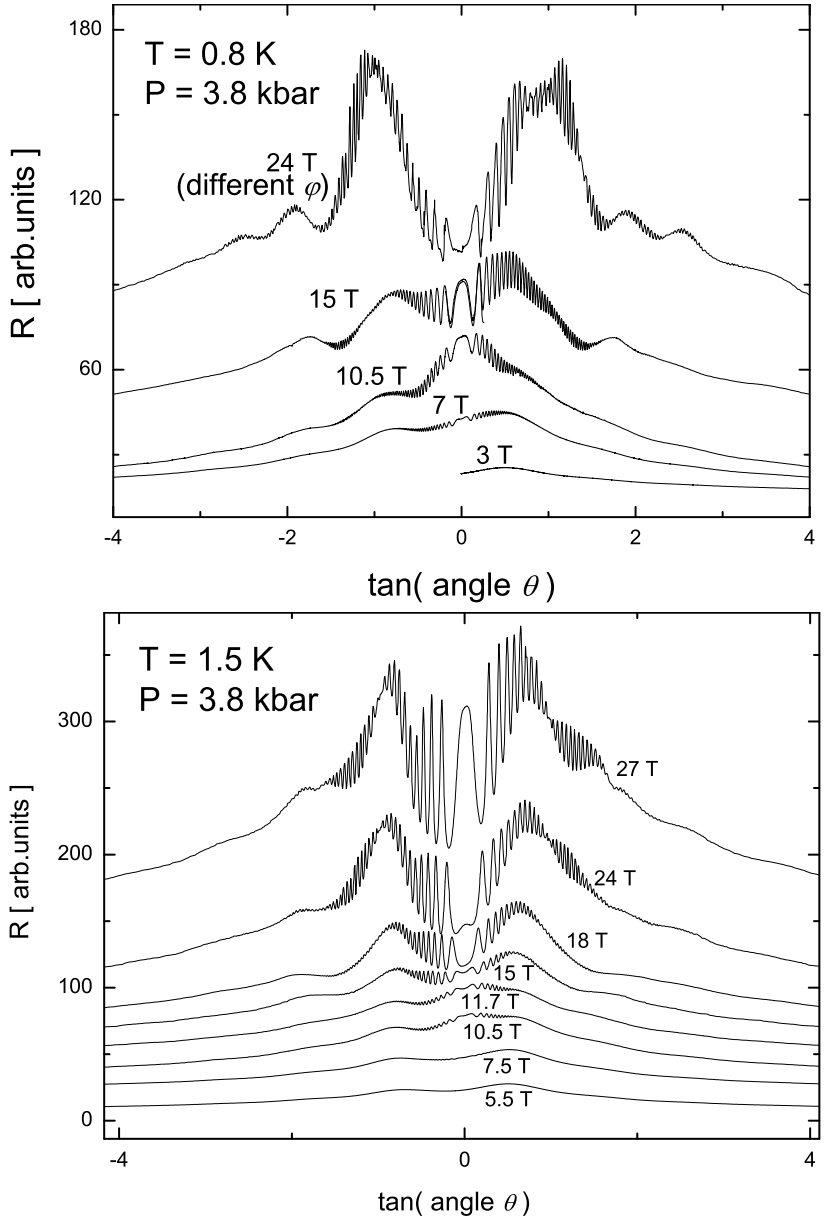

Figure 5.49: AMROs at various const. fields and two different temperatures scaled in tan(θ). For clarity the curves are offset from each other.

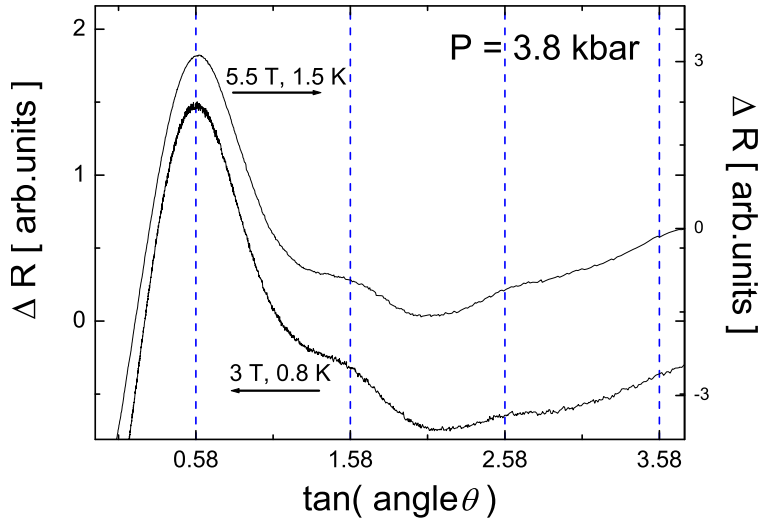

Figure 5.50: Low field AMROs at two different temperatures, where the background has been subtracted. The maxima show a periodicity in tan(θ), marked by dashed lines.

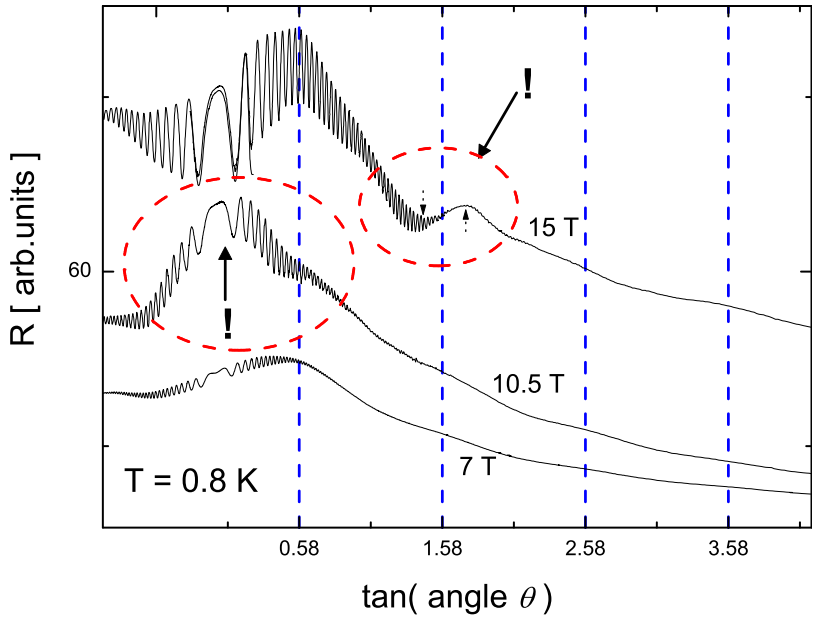

Figure 5.51: Selected curves from Fig. 5.49 in the enlarged scale. Vertical dashed lines show the expected maxima positions of the AMROs in the NM state, periodic in tan(θ). The dashed ellipses mark distinct deviations from the conventional 2D AMRO behaviour (see text).

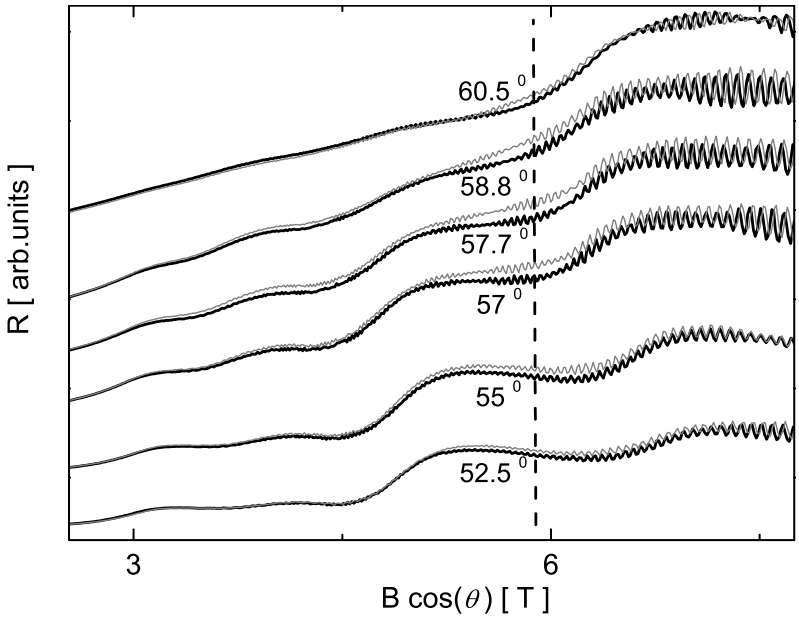

Figure 5.52: Field sweeps at different tilt angles of magnetic field, scaled in $\cos(\theta)$, at 0.4 K and 2.8 kbar. The curves at different angles are offset for clarity. Black curves show up-sweeps of the magnetic field, grey curves down-sweeps. The dashed line marks the position of the FICDW transition for which the observed hysteresis appears to be strongest.

the slow oscillations do scale in $\cos(\theta)$. The imperfect nesting in the re-entrant CDW state therefore must have induced a cylindrical Fermi surface with a very small basal orbit. It also shows that the transfer integral across the layers, i.e. the interlayer band-width, must indeed be negligibly small. As in the case of the perpendicular field direction a hysteresis between both sweep directions is observed. Within this angular range it appears to become strongest at the field-induced transition marked by the dashed line. Further, it can be seen that around 57.7° the magnitude of this hysteresis has a maximum, Fig. 5.53. Note that the temperature here, $T = 0.45$ K, is much higher than for the data in Fig. 5.44; at perpendicular field direction no structure in the hysteresis, corresponding to the different FICDW transitions, has been resolved.

Additionally, the slow oscillations are found to possess "spin zeros" at certain field directions. In Fig. 5.54 the scaled field sweeps for different angles, covering a wide angular range, are shown. The dashed lines approximately mark the fields, where the oscillation amplitude is maximal. As can be seen, the phase of the oscillations inverts several times on tilting the field.

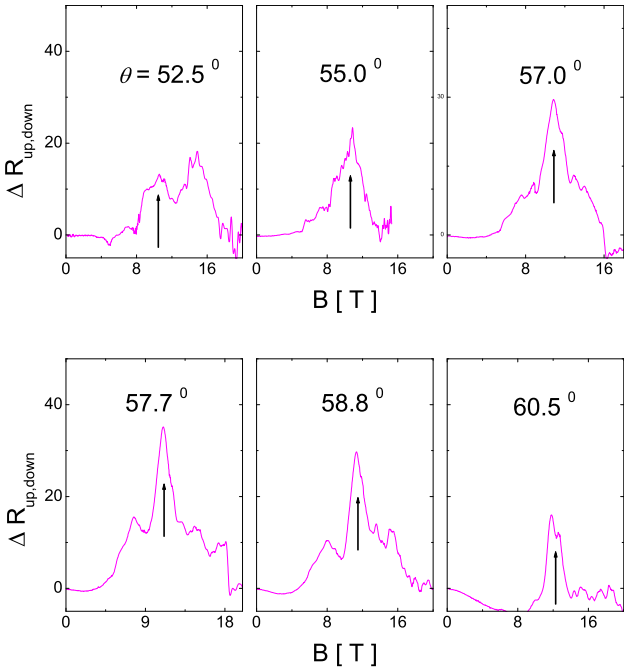

Figure 5.53: Hysteresis obtained from a subtraction of the up- from the down-sweeps of Fig. 5.52 at different field directions. The arrow points to the maximum in the hysteresis at the FICDW transition that is marked in Fig. 5.52 by the dashed line.

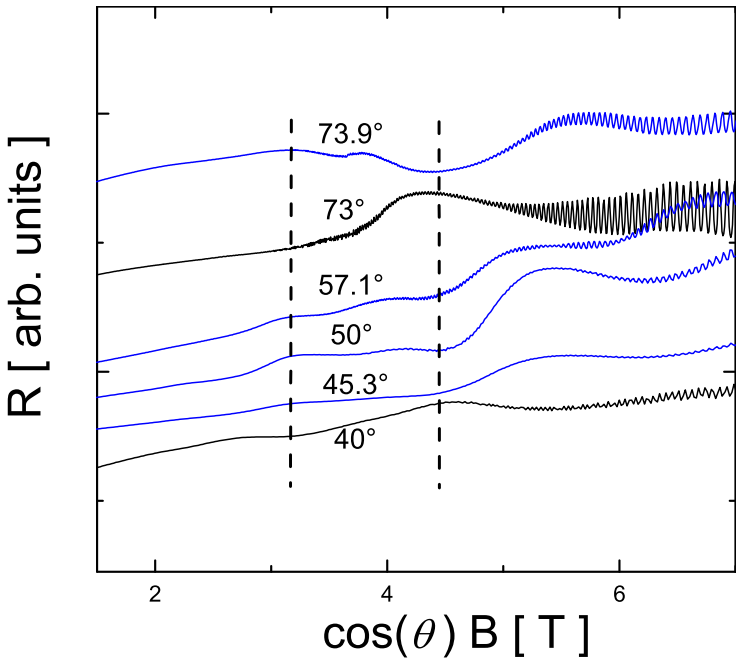

Figure 5.54: Field sweeps as in Fig. 5.52 within a bigger angular range. To illustrate the presence of spin zeros, dashed lines are approximately placed at the extrema of the slow oscillations. On increasing the angle the oscillations show several times a change of the amplitude sign.

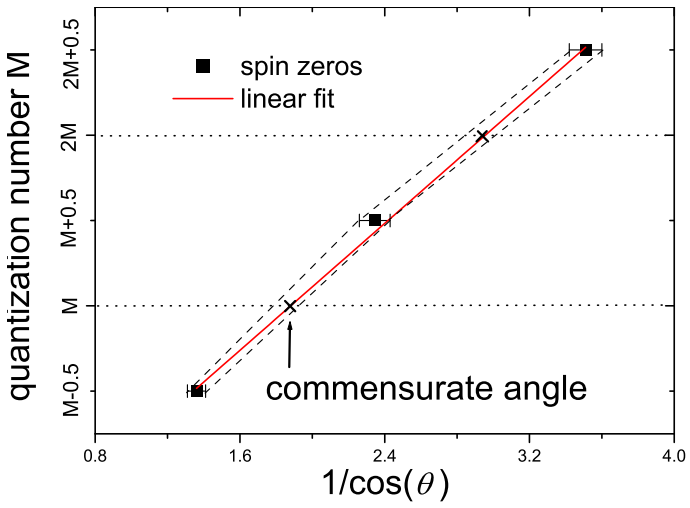

Figure 5.55: Observed angular ranges of the spin zeros scaled according to Eq. (5.11). The expected linear behaviour allows an evaluation of the commensurate field directions with Eq. (5.12).

A "spin zero" occurs, if the quantum oscillation corresponding to the carriers with spin up direction is exactly in anti-phase with the one of the spin down carriers. From the model above (sec. 5.3.2) one can expect that a similar effect takes place for the present slow oscillations at those angles for which the quantized values of the nesting vector for different spin-subbands lie exactly in between each other. These angles are easily derived to be determined by:

$$\cos(\theta) = \frac{1}{\mathrm{M} + 0.5}\left[\frac{2\mu_B}{v_F e a_y}\right]\ ;\ \mathrm{M{=}integer\ number.} \tag{5.11}$$

If these angles are known, there is then the possibility to directly evaluate the commensurate field directions (i.e. the directions, where the quantized levels for both spin directions match each other), which must be given by [129]:

$$\cos(\theta) = \frac{1}{\mathrm{M}}\left[\frac{2\mu_B}{v_F e a_y}\right]. \tag{5.12}$$

In our experiment many field sweeps were performed at different angles. Since the angular step was chosen rather small, the first three ranges, in which the sign reversal of the slow oscillation occurs, are found to be restricted to:

$\theta_{S1} = 40° - 45°$, $\theta_{S2} = 63.7° - 65.7°$, $\theta_{S3} = 73° - 73.9°$.

These angular ranges are in good agreement with the assumed $1/\cos(\theta)$ scaling,

Eq. (5.11), see Fig. 5.55. The corresponding Fermi velocity amounts to $\approx 1.2 \cdot 10^7$ cm/sec, that is about twice the value determined at ambient pressure by Kovalev et al. [136]: $0.65 \cdot 10^7$ cm/sec .

From Eq. (5.12) and Fig. 5.55 the first commensurate field direction may thus be evaluated to: $\theta_{c1} = 55.60° - 58.97°$; i.e. exactly the angular range where we find a pronounced increase in the hysteresis, Fig. 5.53. This remarkable coincidence between our experimental results and the theoretical proposal to our opinion gives the *the strongest evidence thus far for the existence of FICDW subphases*, ever observed in any kind of metallic system.

5.3.5 Conclusion

In the pressure range $P \gtrsim 2.5$ kbar an evidence is given that the CDW *only exists* under magnetic field due to the orbital effect. Within this re-entrant CDW state a quantum oscillation of very low frequency is observed. This is theoretically expected, since the Q1D carriers within this state are no more completely gapped but possess a semi-metallic dispersion relation with very small closed pockets on the Fermi surface. We have shown that the nesting vector adjusts itself according to the Landau quantization of these pockets on the Fermi surface. This determines the new phenomenon of FICDW transitions. The superposition of the orbital quantization and the Pauli effect for the different spin subbands has been theoretically predicted to lead to a quantization spectrum of possible nesting vectors at low enough temperatures. On changing the magnetic field, first order transitions between CDW subphases with different quantized nesting vectors are then supposed to occur. This was confirmed in our measurements by:

(i) a clear hysteretic structure observed in the magnetoresistance at perpendicular field direction at $P = 3$ kbar and $T = 100$ mK.

(ii) a pronounced increase of the magnitude of the slow oscillations and of the hysteresis at 2.8 kbar and 0.4 K on tilting the field to the commensurate angles, where the quantized values of the nesting vector for different spin-subbands superpose on each other.

5.4 Field-Induced CDW Transitions at High Tilt Angles

5.4.1 Magnetic Torque and Magnetoresistance at Ambient Pressure

So far the ambient pressure B-T phase diagram has been considered under a magnetic field applied approximately perpendicular to the highly conducting **a-c** plane. We now investigate changes occurring at ambient pressure on tilting the field towards the plane. Basically, one can expect orbital effects to become strongly reduced at high tilt angles, since their strength depends solely on the field component perpendicular to the layers. If, for instance, the CDW state at ambient pressure is not perfectly nested, a reduction of the orbital effect will change the B-T phase diagram: The low field CDW state becomes suppressed, and therefore the CDW_x state stabilized, already at lower fields.[5] The observed changes on tilting the sample are, however, known to be far more complex. At high tilt angles the magnetic torque as well as the interlayer magnetoresistance exhibit several anomalies in the isothermal field sweeps at low temperatures.

Fig. 5.56 shows an example of the magnetic torque and interlayer resistance recorded at increasing (solid lines) and decreasing (dashed lines) field sweeps, at $\theta = 81.4°$. The data are consistent with previous reports [12, 79, 73]. Indeed, the feature at about 12 T in Fig. 5.56 (as will be shown below) likely corresponds to the kink transition, which is considerably shifted from the zero-angle value, $B_k(\theta = 0) \approx 24$ T. Additionally, at this tilt angle several structures emerge in the field sweeps of both measured quantities above B_k. These anomalies come along with a pronounced hysteresis in the up- and down- field sweeps that suggests, as for the kink transition at perpendicular field direction, these structures to emerge due to first order transitions. They appear below 2 K, their magnitude and the strength of the hysteresis increasing rapidly with further cooling. Note, that by no means these features can be related to the quantum oscillations originating from the Q2D band, since the latter are negligibly weak and have a much higher frequency at such a high θ. The dHvA oscillations are actually seen in the torque data at $B > 25$ T, Fig. 5.56a. Moreover, the new field-induced transitions are found not to be periodic

[5] In a former study of the ambient pressure B-T phase diagrams, at $B \parallel$ **a-c** plane and $B \perp$ **a-c** plane, a small orbital impact at the perpendicular field direction has indeed been proposed [12].

in $1/B$.

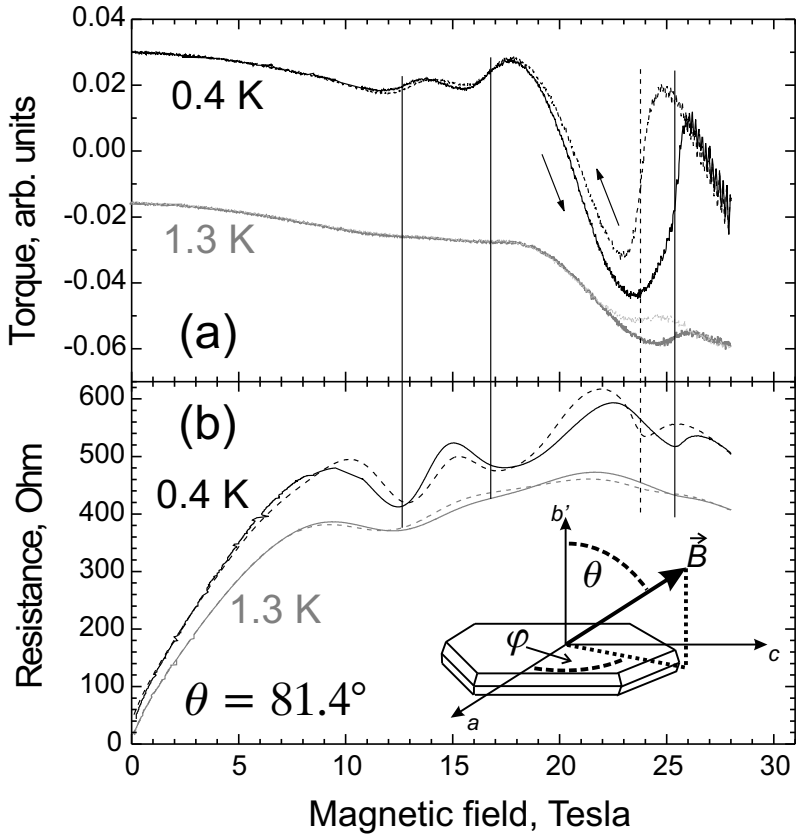

Figure 5.56: Field dependent torque (a) and interlayer magnetoresistance (b) for two different temperatures at $\theta = 81.4°$. Up-sweeps are solid, down-sweeps are dashed lines. The vertical lines demonstrate a correlation between the anomalous torque and resistance features. The inset once again shows the angles determining the field direction.

In order to clarify the origin of these anomalies, we have studied in detail how they develop on changing θ from 40° to 90°. The magnetic torque and the interlayer resistance were always measured simultaneously. In Fig. 5.57 the field-dependent torque recorded at different θ's is shown. In order to enable a direct comparison between the curves, each of them has been divided by $\sin(2\theta)$.[6] The corresponding curves in the resistance are given in Fig. 5.58.

In the following we are going to analyze the torque data in detail. By and large the

[6]If the magnetic field is rotated in the plane perpendicular to the measured torque, the torque intensity can be shown to reveal a $\sin(2\theta)$-behaviour [12].

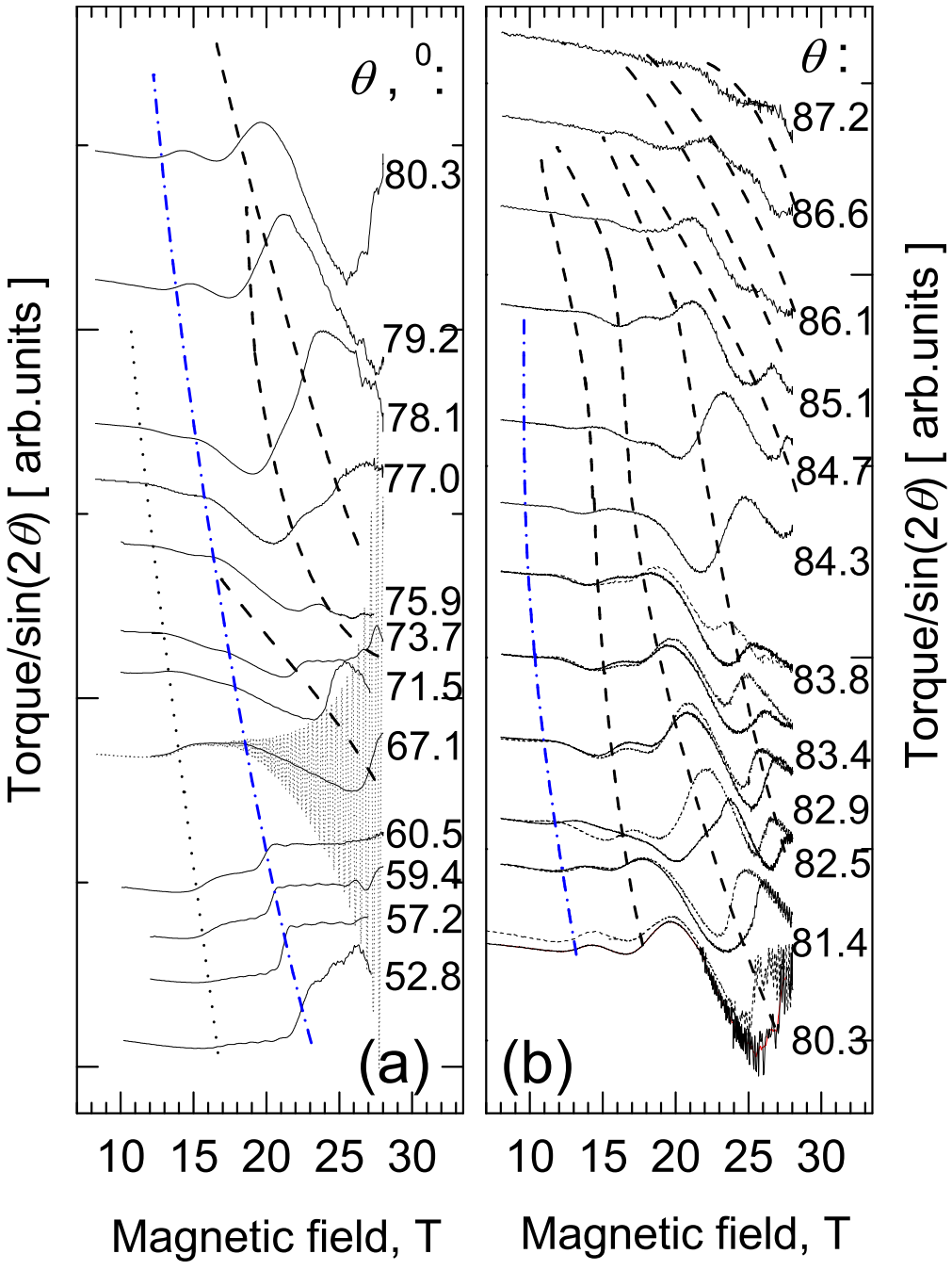

Figure 5.57: Magnetic torque versus field at 0.4 K for various different tilt angles of magnetic field. For an explanation of the different lines see text.

features in the magnetoresistance are found to correlate with those in the magnetic torque (see e.g. Fig. 5.56), although at θ approaching 90° they become more smeared and difficult to interpret in terms of phase transitions. The data represented by solid lines in Fig. 5.57 have been taken at increasing B; additionally, down sweeps are shown in the torque for $81° < \theta < 84°$ (dashed lines) to illustrate the hysteresis. The curves corresponding to $\theta < 81°$ have been obtained by filtering out the dHvA oscillations from the measured signal. An example of the total signal, including the oscillations, at $\theta = 67.1°$ is given by the grey dotted line in Fig. 5.57.

At relatively low angles, one can see a sharp kink transition which takes place at ≈ 22.5 T at 53°. It gradually shifts down on tilting the field and saturates at $\simeq 11$ T as θ approaches 90°, as shown by the blue line. As B_k decreases below 20 T, the transition becomes less pronounced, although it can still be detected up to $\theta \approx 85°$.

Below B_k, a weak additional feature is observed up to 78° (dotted line in Fig. 5.57). While its origin is not clear at present, it may be related to the hysteretic changes of the magnetoresistance [109, 137] and magnetothermopower [138] observed in the same field range earlier.

Starting from 65°, new features emerge at the high-field side, moving to lower fields with further increasing θ. Like the kink transition, they are rather sharp and strongly hysteretic at high fields and gradually fade below 20 T. The structure changes with increasing rate at $\theta \to 90°$. At the same time the features become less pronounced and could not be resolved above 88°. While the observed behavior is strongly suggestive of multiple phase transitions, at the moment it is difficult to determine the exact location of each transition. However, taking into account the character of changes in the magnetization and the hysteretic behavior, it is reasonable, by analogy with B_k, to identify the transition points with local maxima in the derivative $(\partial M/\partial B)_\theta$.

Such points are plotted in Fig. 5.59 in the form of a $B - \theta$ phase diagram. In Fig. 5.60 the same data are replotted against $1/\cos(\theta)$ in order to show the region near 90° in more detail. The crosses represent $B_k(\theta)$, the empty circles correspond to the weak feature below B_k, and the solid circles delineate the boundaries between new subphases within the high-field CDW_x state. There is a clear tendency for all the transitions to shift to lower fields with increasing θ.

The increasingly strong angular dependence in the vicinity of $\theta = 90°$ and the absence of the features at the exactly parallel orientation suggest that the orbital effect, determined by the perpendicular component of magnetic field $B_z = B\cos(\theta)$, plays a crucial role. Further, since these multiple transitions happen to appear only

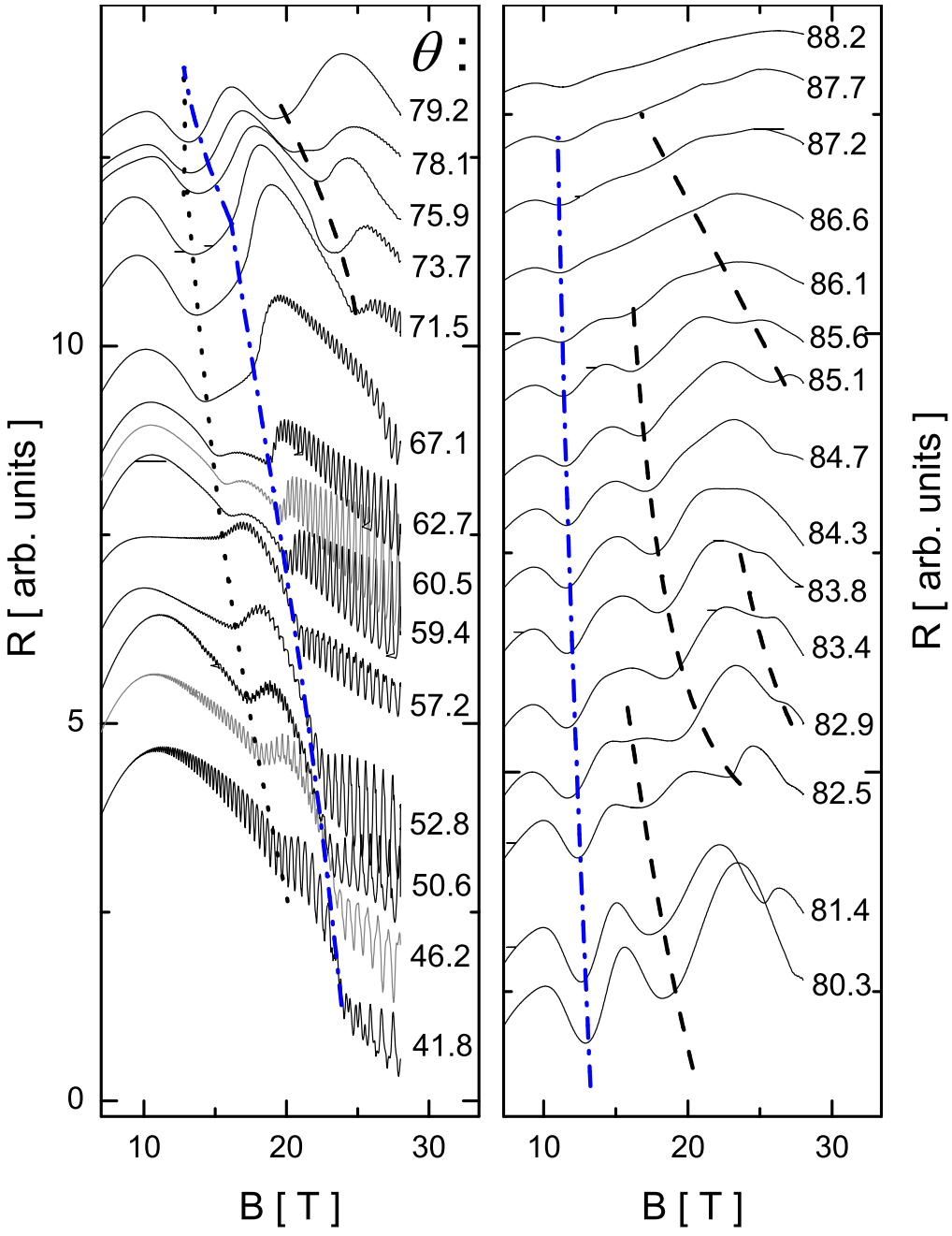

Figure 5.58: Magnetoresistance versus field at 0.4 K for various different tilt angles of magnetic field. As for the torque (Fig. 5.57) dashed and dotted lines indicate the shift of the various transitions observed.

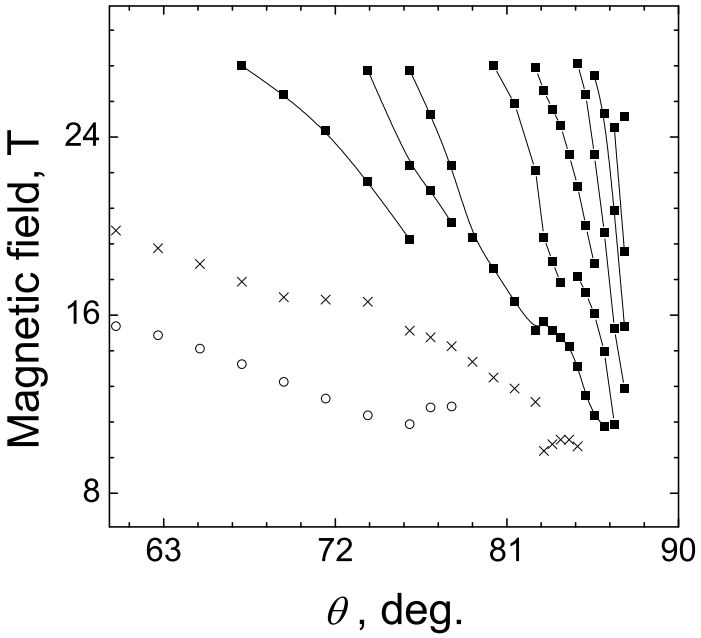

Figure 5.59: Observed phase lines plotted in a $B-\theta$ phase diagram. Crosses mark the position of the kink transition, open circles the anomalous low field feature and solid squares the first order transitions extracted from Fig. 5.57.

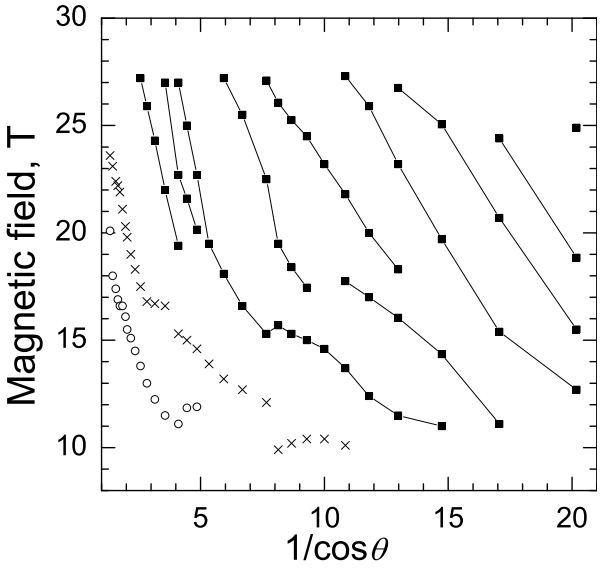

Figure 5.60: The transitions shown in Fig. 5.59 are plotted in $1/\cos(\theta)$-scale to give a better high angle resolution.

above B_k, one can also expect the energy splitting of the spin subbands to be important. Therefore it is very likely that the observed transitions originate from an interplay between the Pauli and orbital effects. This is in line with the observed independence of the anomalous features with respect to the azimuthal angle φ of the rotation plane.

Noteworthy, the presented data are in clear contradiction to the interpretation of Qualls et al. [79], who performed similar measurements. They claimed that starting from a threshold angle the kink transition splits into two transitions, one steadily going down and one steadily moving up in field with further tilting the field direction. Since our results could be reproduced on several samples from different batches remarkably well, we believe that the observations from Qualls et al. [79] are very likely misinterpreted. This is, however, fairly understandable, since in their measurements the angular step of the field sweeps was chosen rather large. In view of our observed phase diagram it is therefore clear that it is very hard to follow the behaviour of the transitions with only a few curves at different angles.

5.4.2 New Quantum Phenomenon

Since the whole scenario appears above B_k we conclude that these first order transitions are restricted to the high field state. We therefore must reconsider the theoretically predicted properties of the CDW$_x$ state. Above B_k the nesting vector shifts in x-direction in order to nest at least one of the spin subbands [14], i.e. the spin-up band. The electrons on this band therefore remain completely gapped. This happens, however, at the cost of an additional unnesting of the spin-down band. The latter, therefore, suffers strongly imperfect nesting, a situation very similar to the one for $t_c' > t_c'^*$, only that the unnesting role is now taken by the Pauli effect of magnetic field instead of hydrostatic pressure. Hence, as for the FICDW case under pressure, the spin down band has closed pockets, which determine a quantization condition of the nesting vector. The nesting vector again adjusts itself in order to place the chemical potential between the Landau levels of these closed pockets.

The whole scenario of the moving Q_x component of the nesting vector is pictured in Fig. 5.61. Above B_k and below $T < T^* \simeq 0.6T_c(0)$ there is the steady k_x-shift of the nesting vector: $Q_x(B) = Q_{x,0} + q_x^{\mathrm{Pauli}}(B)$, where $Q_{x,0}(= 2k_F)$ is the zero-field x-component of the nesting vector. The additional term $q_x^{\mathrm{Pauli}}(B)$ asymptotically approaching the value $2\mu_B B/\hbar v_F$ is schematically shown in Fig. 5.61 by the blue line. At low enough temperatures there must be then an additional quantization

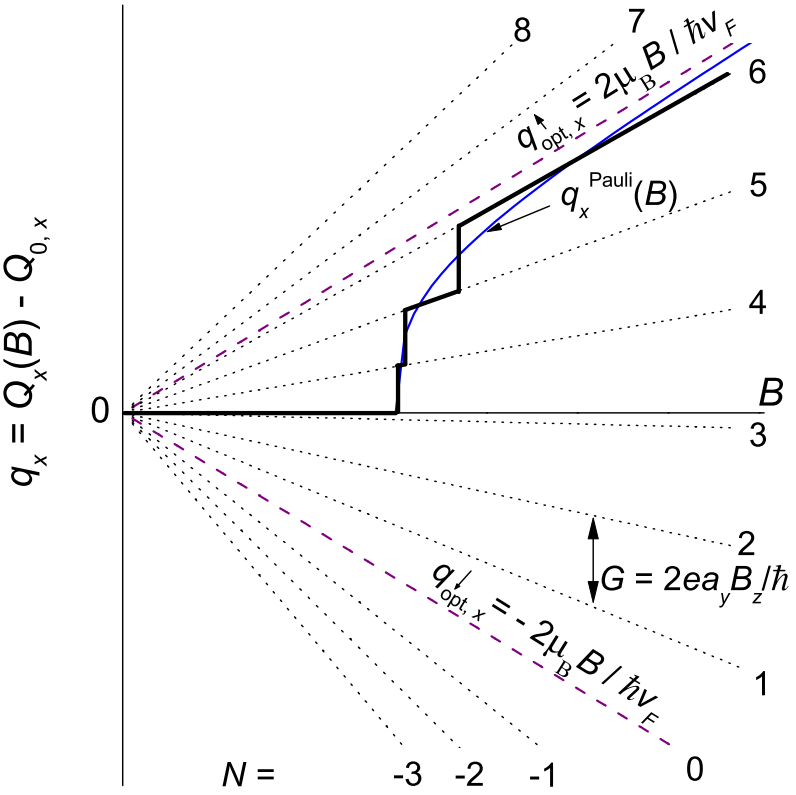

Figure 5.61: Within the CDW$_x$ state the density wave vector shifts in order to nest at least one of the spin subbands (thin blue line). The other spin subband therefore suffers strong imperfect nesting leading to the quantization condition of the nesting vector (dotted lines) counted from its perfect nesting condition (lower dashed line). This causes successive field-induced first order transitions at low temperatures especially at high tilt angles. The quantized jumps of the nesting vector is sketched by the thick solid line.

condition which is only determined by the spin down band. This quantization is thus counted from $Q^{\downarrow}_{\mathrm{opt},x}(B)$ and may be written as:

$$Q^{\mathrm{orbit}}_{x,N} = Q_{0,x} + Q^{\downarrow}_{\mathrm{opt},x}(B) + NG = Q_{0,x} - 2\mu_B B/\hbar v_F + NG; \tag{5.13}$$

$$G = \frac{2ea_y B_z}{\hbar} \tag{5.14}$$

The corresponding values $q^{\mathrm{orbit}}_{x,N} = Q^{\mathrm{orbit}}_{x,N} - Q_{0,x}$ are schematically shown by dotted lines in Fig. 5.61.

As a result, the values of the nesting vector above B_k most favorable for both

the spin-up and spin-down subbands should be determined by intersections of the continuous curve $q_x^{\mathrm{Pauli}}(B)$ with the straight lines $q_{x,N}^{\mathrm{orbit}}$, i.e. by the superposition of the Pauli and quantum orbital effects. At fields close to these intersection points we then expect the nesting vector to remain on the quantized levels. This means that the system tries to keep both, spin up and down, type of carriers completely gapped. Thus, with changing the field we obtain a series of first order transitions between CDW subphases characterized by different quantized values of the nesting vector as schematically shown by thick lines in Fig. 5.61. Remarkably, this model implies an *increase of the quantum number* N with increasing B, in contrast to what is usually observed in known orbital quantization phenomena.

Since the quantization condition is given by one spin subband while the other one remains completely gapped, this also explains the occurrence of the first order transitions at much higher temperatures than in the FICDW case under hydrostatic pressure. In the latter both spin subbands contribute quantized levels. If the nesting vector then takes a certain quantized value it may be favorable for one, but not for the other spin band. The first order FICDW transitions are therefore predicted only to appear at higher temperatures when both sets of quantized levels match each other at certain "commensurate" field directions (Eq. (5.12)).

From Fig. 5.61 it is clear that the proposed multiple transitions can only take place if more than one quantum level intersect the $q_x^{\mathrm{Pauli}}(B)$ curve, i.e. when

$$3G = 6ea_yB_z/\hbar < 4\mu_BB/\hbar v_F. \tag{5.15}$$

This condition is obviously not satisfied at low θ where only one, kink transition is observed. With increasing θ, the separation between the levels, G, proportional to the perpendicular field component B_z decreases whereas the isotropic Pauli effect remains unchanged. Starting from a threshold angle θ^*, the above condition becomes fulfilled and a new transition emerges at a high field, shifting towards B_k at a further increase of θ. In our experiment the first transition above B_k is found at $\theta \approx 65°$.

This allows us to estimate the upper limit for the Fermi velocity in the 1D direction:

$$v_F \lesssim 2\mu_B/(3ea_y \cos 65°) \approx 9 \times 10^6 \ \frac{\mathrm{cm}}{\mathrm{sec}}, \tag{5.16}$$

which is in good agreement with the recently reported value $v_F = 6.5 \times 10^6$ cm/sec [136].

Thus, the proposed model explains not only the occurrence of multiple first-order transitions above B_k, but also the threshold angle above which they start to appear as well as the general tendency of them to shift towards B_k with further tilting the field. Obviously, the sharpness of the transitions between the quantum orbital levels

should strongly depend on temperature and on the strength of the perpendicular field component. This is consistent with the observed damping of the structure with increasing temperature (Fig. 5.56) or at θ very close to 90° (Fig. 5.57).

There are, however, some inconsistencies between the experiment and the model given above. The experimental phase diagram (Fig. 5.59) looks more complicated than it would be expected within the present qualitative model: some phase lines appear to be split, giving rise to additional subphases. This disagreement is, however, not surprising. On the one hand, we neglected the possibility of an additional phase, CDW_y ($q_x = 0; q_y \neq 0$), that may appear on tilting the magnetic field in a certain angular and field range [14]. This has indeed been suggested by Qualls et al. [79], but as already mentioned their determined $B - \theta$ phase diagram is very likely incorrect. On the other hand, the orbital quantization effects may depend on details of the anti-nesting term [139]. The latter is most likely more complex than given by Eq. (5.6), according to band structure calculations [57,140]. This can modify the high-field subphase structure. Further, according to newest theoretical results from Grigoriev, under some circumstances there might exist a possibility of two nesting vectors (one for each spin subband) spatially coexisting within the modulated $\mathrm{CDW}_{x(,y)}$ state. While the physical nature of the field-induced transitions remains the same, quantitative changes would be expected.

There are other open questions, such as the transition-like feature below B_k and the considerable (although at a slower rate) decrease of B_k with increasing θ. Such a strong decrease of the kink transition down to 11 T would imply a very strong contribution from the orbital effect already at ambient pressure that can not be expected from the phase diagram studies in section 5.1.

A development of a quantitative theory will certainly help to understand the entire phase diagram of the present compound and to get a deeper insight into the interplay of the Pauli and orbital effects in CDW systems.

5.4.3 Conclusion

Simultaneous measurements of the magnetic torque and magnetoresistance at different tilt angles of magnetic field at ambient pressure have been performed.

The already known anomalies in the magnetic torque as well as in the magnetoresistance occurring at ambient pressure at fields strongly inclined to the conducting planes turn out to be a new kind of FICDW transitions. In contrast to the ones

under hydrostatic pressure, it is now the Pauli effect of magnetic field which causes a partial ungapping of the carriers on one of the spin-subbands. We propose a simple model [141] in which the nesting vector within the modulated CDW_x state steadily moves in order to gap at least one of the spin-subbands, while the Landau quantization of the partially ungapped band leads to quantized values of the nesting vector. The superposition of both effects then determines the observed multiple phase transitions. Within this model the overall decrease of the transition fields with angle as well as the threshold angle above which the multiple transitions start to appear, can be understood very well.

5.5 Charge-Density Wave versus Superconductivity

5.5.1 Superconductivity under Hydrostatic Pressure

Within the family of organic metals α-(BEDT-TTF)$_2$MHg(SCN)$_4$ the compounds with M = K, Tl, Rb have CDW ground states with slightly different transition temperatures while the compound with M = NH_4 happens to undergo a superconducting (SC) transition at $\approx$ 1 K [62, 63]. The absence of a density wave in the latter salt is to the moment interpreted to be due to a higher interchain coupling of the organic molecules within the layers [142], that strongly worsens the nesting conditions of the open sheets of the FS. Moreover, it has been shown [143] that by tuning the ratio of the lattice constants c/a with the aid of uniaxial strain a density wave can be even (i) induced in the NH_4-compound and (ii) suppressed in the K-compound, a SC state being stabilized at $\approx$ 1 K. From combined uniaxial strain measurements and band structure calculations a major contribution to superconductivity has been proposed to come from the Q1D band [142]. As we have seen in the previous sections a hydrostatic pressure also worsens the nesting conditions in the K-salt, the CDW being completely suppressed in zero field at $P \gtrsim 2.5$ kbar. One therefore might expect a SC state also to appear under hydrostatic pressure. Previous measurements under hydrostatic pressure by Brooks et al. [15] down to 50 mK however failed to observe any sign of superconductivity. It was only at ambient pressure, that the resistance decrease on lowering the temperature has been found to significantly accelerate below 300 mK [144]. This acceleration by that time was proposed to have a superconducting origin, due to its strong dependence on the current level and weak magnetic field.

In order to clarify the presence of superconductivity at ambient pressure as well as under hydrostatic pressure, detailed resistance measurements on three samples of the M=K-compound were done down to the lowest possible temperature. For this purpose, the Cu-Be pressure cell was mounted on a dilution refrigerator allowing the sample to be cooled down to $\approx$ 20 mK. The current applied during the measurement was kept $\leq$ 100 nA. Thus the resulting overheating of the sample during the measurement could be estimated to be $<$ 5 mK at 20 mK.

Surprisingly, we found superconductivity on all samples studied at such low tem-

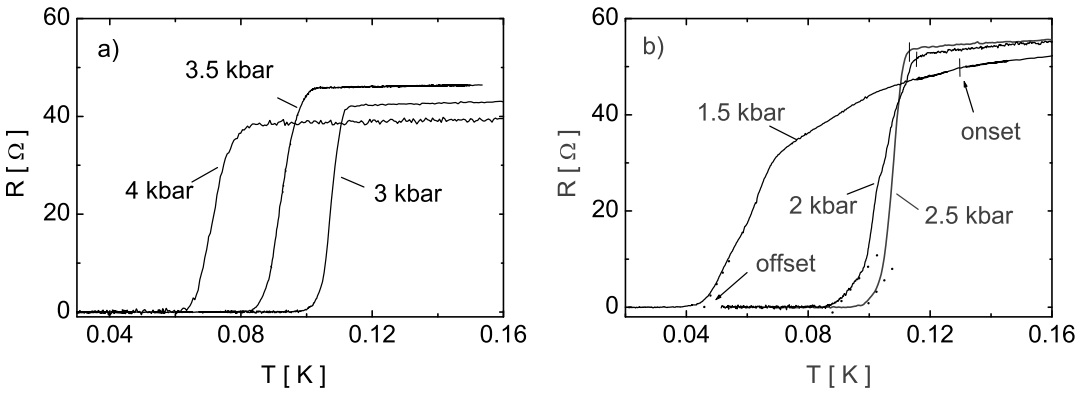

Figure 5.62: Temperature sweeps at different pressures down to the lowest possible temperature. On the left hand side the SC transitions within the NM state are shown. To the right the broadened transitions within the CDW state are plotted. Vertical dashes mark onset temperatures, dotted lines offset temperatures, of the bulk SC transitions.

peratures. Moreover, the superconductivity even turned out to be present in the whole measured pressure range up to 4 kbar [145].

In Fig. 5.62 several temperature sweeps of the interlayer resistance for one sample measured at different pressures are shown. At $P = 3$ kbar the resistance exhibits a normal metallic behaviour on cooling until at 110 mK a sharp SC transition occurs. Within the NM state the SC transition remains sharp and the transition temperature shows a linear pressure dependence of about -30 mK/kbar [145]. This is, like the transition temperature itself, about an order of magnitude lower than in the NH_4-salt [2] at ambient pressure. A linear suppression of superconductivity with hydrostatic pressure is commonly observed in (BEDT-TTF)-salts and is usually attributed to a strong compression of the crystal lattice, in particular in the interlayer direction [2].

The above described behaviour changes on entering the CDW state, i.e. with lowering the pressure to ≤ 2.5 kbar. Remarkably, the superconductivity does not vanish in the CDW region. At 2.5 kbar the bulk transition temperature remains at the value observed at 3 kbar, instead of the expected enhancement. With further decreasing pressure, as can be seen in Fig. 5.62b, the transition starts to broaden, being accompanied by several anomalous step-like structures. This leads to a strong suppression of the temperature T_0 where zero resistance is reached and at ambient pressure no zero-resistance is observed down to 20 mK. The whole behaviour described above was also observed on another sample, measured simultaneously. In comparison to sample #1 the SC transition temperatures, however, appeared to be

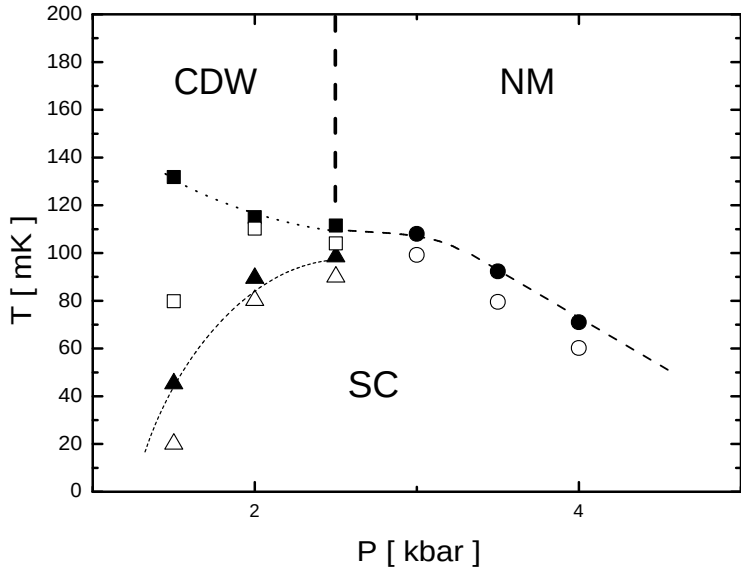

Figure 5.63: Low temperature part of the P-T phase diagram. Filled symbols correspond to sample#1, open ones to sample#2. Circles mark the inflection points of the sharp SC transition within the NM state. Squares (triangles) mark the onset (offset) temperatures of the bulk SC transitions within the CDW state as shown in Fig. 5.62

10 % lower over the whole pressure range.

The transition temperature T_c, extracted from the inflection point of the transition, are presented, as a function of pressure, as filled circles in Fig. 5.63. Due to the broadening of the SC transition within the CDW state, an exact determination of T_c cannot be done below the critical pressure $P_0 \simeq 2.5$ kbar. We therefore determine the on- and offset transition temperatures as shown in Fig. 5.62b. Additionally, the transition points from sample #2 are added to Fig. 5.63. Obviously, the transition temperatures of both samples do not coincide. The sample dependence of the transition temperatures (Fig. 5.63) points to a possible non-pure s-wave nature of the superconducting order parameter, as it has already been suggested for some other BEDT-TTF based superconductors [2]. We expect crystal defects or impurities to have a big effect on T_c because the crystal quality of both samples, extracted from the residual resistance ratios or from the Shubnikov-de Haas oscillations of the Q2D band, appeared to be rather high (the quality of sample #1 being a little better). Within the CDW state of our compound the sample dependence of the transition points is found to become even stronger (see 1.5 kbar points in Fig. 5.63). Thus, the

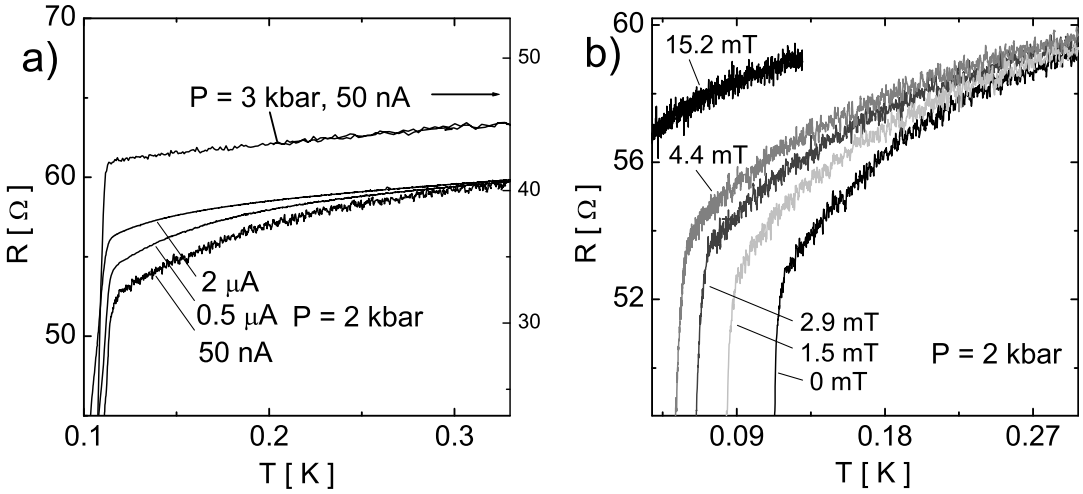

Figure 5.64: Within the CDW state the resistance decrease accelerates already at much higher temperatures than in the NM state ($P = 3$ kbar). This decrease strongly depends on the level of the applied current (a) or magnetic field (b).

additional influence of the CDW on superconductivity is also most likely dependent on impurities or defects.

Besides the broadening of the bulk transition, all temperature sweeps within the density wave state show an unusually strong decrease (negative curvature) of the resistance in a remarkably wide temperature range well above the T_c that would be expected from its linear pressure dependence in the NM state. The starting temperature of this anomalous behaviour was found to be nearly pressure independent within the CDW state. In Fig. 5.64 the temperature region above the, still rather sharp, bulk transition at 2 kbar is shown at different current levels and magnetic fields, applied perpendicular to the conducting layers. As can be seen, the decrease of the resistance strongly depends on the applied current and field, i.e. by increasing the current or field the resistance decrease becomes suppressed. Note that at higher currents the bulk transition temperature only changes slightly. Effects of overheating therefore can be neglected. These observations are strongly in favor of small SC regions already being present at much higher temperature than the expected bulk transition temperatures [144]. Similar behaviours were found throughout the entire CDW pressure range. Only the starting temperature is found to be slightly pressure dependent: 250 mK at 2.5 kbar and 300 mK at 2 kbar and 0 kbar.

On the contrary, in the NM state such an accelerated decrease of the resistance above the bulk SC transition is either absent or at least strongly reduced (see the 3 kbar curve in Fig. 5.64). Thus there exist SC regions within the CDW state with

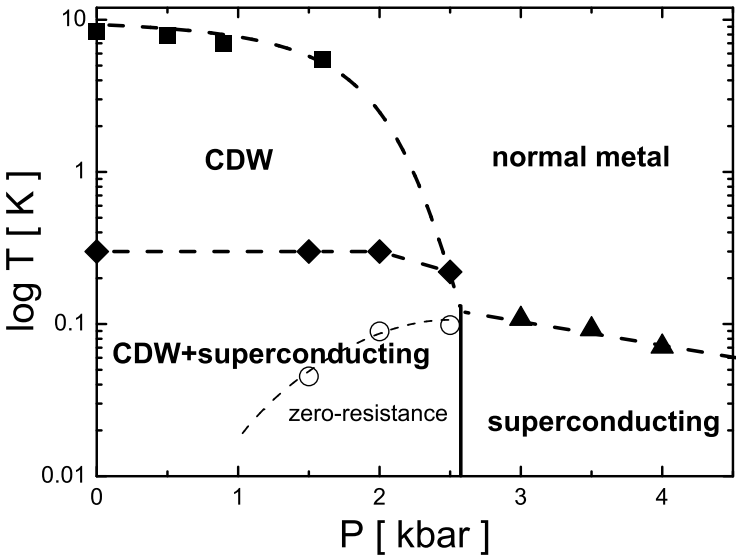

Figure 5.65: Proposed P-T phase diagram.

a T_c that is remarkably higher than the one expected from the NM state. The whole phase diagram including all phases must, therefore, qualitatively look like the one sketched in Fig. 5.65.

In Fig. 5.66 a comparison between the in- and interplane resistance is shown for sample #2 at pressures above and below P_0. To perform measurements of the inplane resistance four contacts were placed on one side of the sample. Note that in order to measure the inplane resistance to a reasonable accuracy the applied current had to be at least 0.5 μA. However, despite this high current it is seen that the SC transition in the plane occurs at a slightly higher temperature in comparison with the interlayer one. The slight difference in the transition temperatures can be understood by the superconductivity first developing within the planes which than become coupled at lower T. Such a scenario has also been proposed in the NH_4-compound [63]. At 1.85 kbar the zero resistance could already be observed within the plane while the interlayer transition was found to be still incomplete. A clear broadening of the inplane transition within the CDW state is, however, also observed. We therefore expect the inplane resistance to behave in a very similar manner as described above for the interplane component. This is in line with the incomplete SC transition in the inplane resistance reported by Ito et al. for ambient pressure [144].

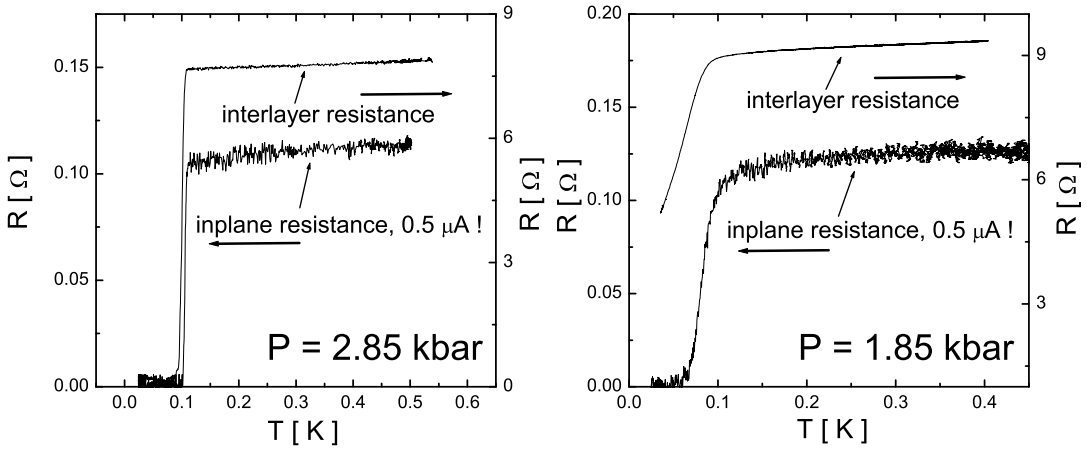

Figure 5.66: Comparison of the in- and interlayer resistance at pressures above (to the left) and below (to the right) the critical value P_0=2.5 kbar.

Since at ambient pressure we have an incomplete broad transition that with increasing pressure becomes remarkably sharp, we exclude the possibility of pressure inhomogeneities within the sample. Then the question arises, why within the CDW state the bulk in- and inter-plane SC transition becomes strongly broadened. Generally one can think of (classical) phase fluctuations, typical of highly anisotropic electron systems with small superfluid density, that leads to a suppression of the bulk superconductivity [146] as has been observed in high T_c superconductors [147]. However, in our system the SC transition temperature is of the order of 100 mK and the corresponding temperature scale of the superconducting "phase stiffness" [146] can be assumed to be at least an order of magnitude higher. In such a case, effects of phase fluctuations on T_c are proposed to be negligible [146]. The incomplete SC transition found by Ito et al. [144] at ambient pressure was by that time interpreted in terms of the proximity of the in-plane sheet resistance to the critical value $h/(4e^2)$ of a superconductor-insulator transition, known to occur in disordered two-dimensional superconductors [148]. Since the isomorphous NH_4-salt does not undergo the CDW transition but instead becomes superconducting, the rather sharp bulk SC transition in that compound was thus explained [144] by the sheet resistance far below $h/(4e^2)$. This interpretation of incomplete superconductivity assumes that within the density wave the sheet resistance becomes enhanced. Thus, one should expect that with the suppression of the CDW under pressure the superconducting T_c becomes enhanced. Obviously the sharp transitions at $P \geq 2.5$ kbar are far below the proposed ambient-pressure T_c, i.e. 300 mK. The incomplete superconductivity within the CDW state therefore can hardly be attributed to the proximity of an insulator transition. Fur-

ther, dT_c/dP in the NM state of the title compound is found to be ≈ 30 mK/kbar, that is nearly an order of magnitude smaller than observed in the NH_4-salt [2]. This might be due to different parts of the Fermi surface contributing to superconductivity in both compounds. Therefore, a direct comparison of the SC properties of the two salts is likely inappropriate. The pressure dependence of T_c in the NM state is indeed better comparable to the one observed in the Q1D TMTSF (or TMTTF) based organic metals, where a superconducting state is found in the FISDW pressure region.

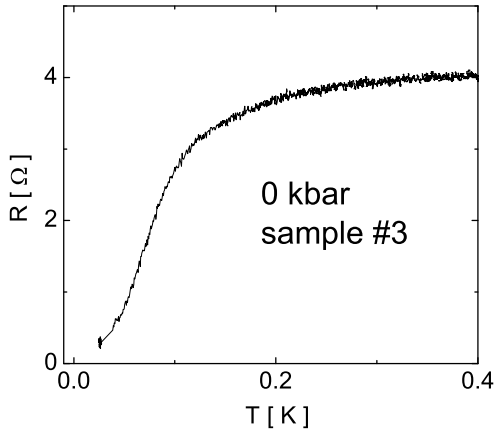

Figure 5.67: One sample nearly reached zero resistance at 25 mK already at ambient pressure.

A clue to the real nature of the strongly broadened bulk transition comes from ambient pressure measurements on a sample from a different batch. This sample almost reached zero-resistance at ambient pressure reflecting the already mentioned sample dependence of the SC transition [145], see Fig. 5.67. This, however, need not mean that the whole sample at lower temperatures is in the SC state. We performed d.c. magnetization measurements on the same sample using the SQUID (superconducting quantum interference device) technique and could not see any Meissner signal down to 6 mK.[7] Therefore the zero resistance is most likely achieved via a percolating network of thin SC paths. A coexistence of superconductivity and density wave in real space we, therefore, do not expect. This is also supported by theoretical predictions that a charge density wave leads to a suppression of superconductivity [149]. We therefore consider an inhomogeneous system of SC filaments embedded in a metallic (actually CDW) matrix to be more likely. The SC coherence thus develops within the filaments until at lower temperatures they couple with each other via the proximity effect. At ambient pressure the filaments are strongly separated, so that such a completely Josephson-coupled system does not exist at $T > 20$ mK. A strong broadening of the bulk SC transition was indeed shown to exist in a two dimensional array of SC islands which are imbedded in a metallic matrix [150, 151]. After the islands become SC the decrease of the resistance is determined by the growth of the normal metallic coherence length on

[7] This measurement was performed in another dilution refrigerator at the WMI, the so-called "Bavarian milli-mill", in collaboration with Dr. E. Schuberth.

lowering the temperature, i.e. the proximity effect. The structures within the transitions observed in the title compound then can be explained by filaments which are not all equidistant causing several ("bulk"-) transitions to occur. Under hydrostatic pressure within the CDW state, we also know that small SC regions or filaments must exist at higher temperature. Since we have no possibility at the moment to study the magnetization under pressure, we cannot directly verify the absence of the Meissner effect. However, as we shall see next, the filamentary nature of the superconductivity under hydrostatic pressure is supported by measurements of the SC transition in magnetic field.

5.5.2 Critical Magnetic Field

In Fig. 5.68 we show magnetic field sweeps, with the field directed perpendicular to the planes, at different temperatures and two pressures above and below the critical value P_0. At zero field the bulk transition temperature at these two pressures can be considered to be approximately the same (Fig. 5.62). At 3 kbar the transitions remain sharp over the whole temperature range while at 2 kbar they become somewhat broadened at lower T. The critical fields B_p determined as shown in Fig. 5.68 are plotted in Fig. 5.70 for 3 different pressures. At $P = 3$ kbar the critical field shows a nearly linear dependence on temperature that can be expected for coupled SC planes in the 3D limit [147]. On entering the CDW state B_p at low temperatures becomes dramatically enhanced, leading to a very strong positive curvature seen in

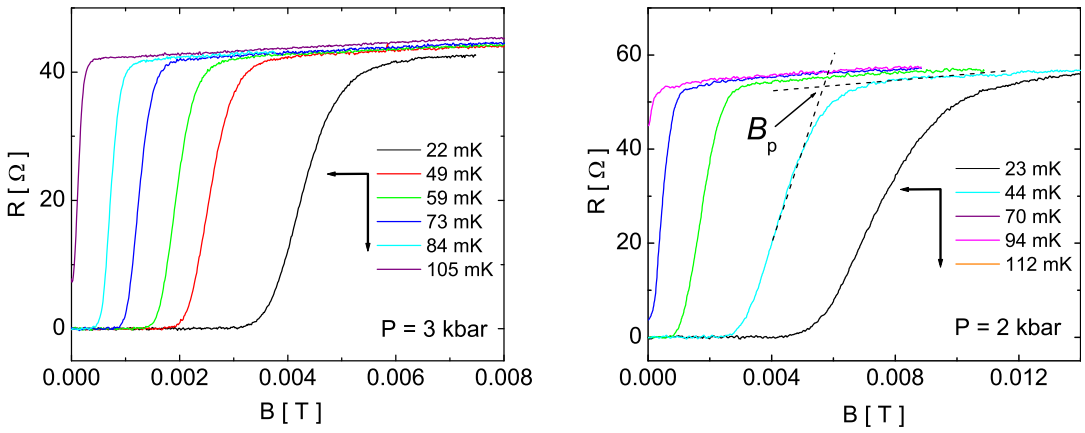

Figure 5.68: Field dependence of the interlayer resistance at various const. temperatures for pressures above and below P_0=2.5 kbar.

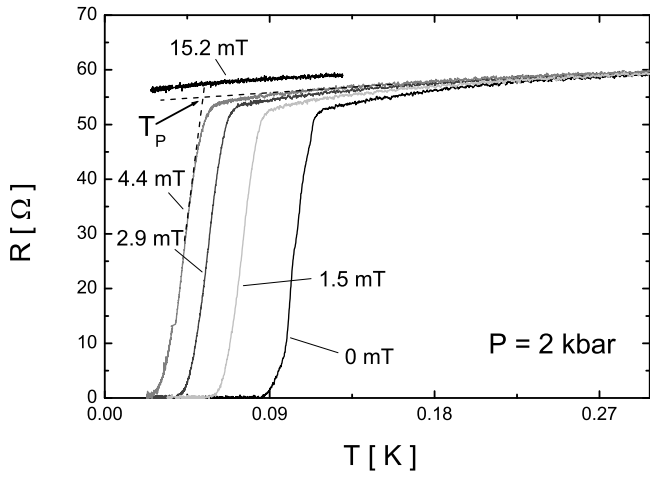

Figure 5.69: Temperature dependent interlayer resistance at different constant magnetic fields and $P = 2$ kbar.

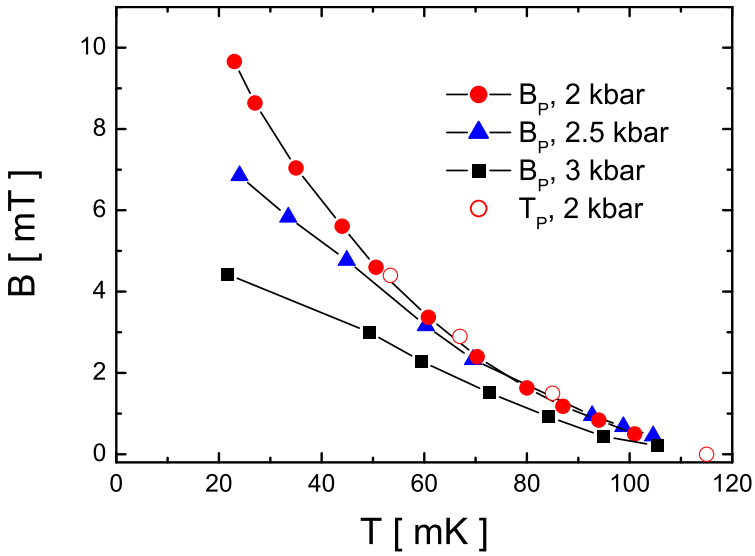

Figure 5.70: Critical fields and temperatures determined at pressures around the critical value P_0=2.5 kbar.

its temperature dependence at 2 kbar. It is important to note that this behaviour does not depend on the criteria of how we determined B_p. The fact that at 2 kbar the bulk transition in the temperature sweep does not broaden with applying a magnetic field, see Fig. 5.69, makes us believe that effects of vortex melting can be neglected. Thus, the bulk transition is still thoroughly determined by the coupling of the filaments. The broadening of the transition in magnetic field sweeps at low temperatures (Fig. 5.68) is fully consistent with the positive curvature of B_p and the field-independent transition width in the temperature sweeps (Fig. 5.69).

An enhanced upper critical field is generally known to exist in a superconductor if its thickness perpendicular to the field becomes less than the coherence length [147]. A dimensional crossover with lowering T in layered superconductors then also leads to a strong positive curvature of the parallel upper critical field. However, we do not consider B_p to be the upper critical field of the SC filaments, since it is determined from a bulk resistive transition. This means that the behaviour of B_p defined above can differ from the real H_{c2} behaviour. Although an exact theoretical description of the resistive transition of a proximity coupled array of SC filaments still has to be worked out, a comparison to existing filamentary systems shows that a strong positive curvature of B_p can be expected.

As an example one can mention polysulfur nitride $(SN)_x$, a compound that consists of bundles of SC filaments. For a magnetic field applied perpendicular to the fiber axis the temperature dependence of the resistive transition was shown to exhibit a positive curvature [152]. Another, and probably more relevant example is the well known CDW compound $NbSe_3$. It has been reported that within the CDW state of $NbSe_3$ a small fraction of the sample becomes SC [153] and it has been proposed to emerge within the boundaries of CDW domain walls, where the CDW order parameter is supposed to become zero. This would then indeed be a system of SC filaments separated by metallic CDW regions as suggested in our model above. At higher pressure the CDW gap becomes smaller and thus the domain wall region, where ungapped Q1D-electrons can exist, is expected to become bigger. Moreover, a strong sample dependence of the SC properties would not be surprising in such a model, since crystal defects or impurities very likely disturb the domain structure. Whether such a domain structure really exists in the title compound we cannot judge from our data, but the similarities of these two CDW compounds with respect to their SC properties suggests the nature of the critical field behaviour to be the same.

Noteworthy, there might exist a narrow pressure region near P_0, in which the

system becomes inhomogeneous, irrespective of any domain structure. Such an inhomogeneous system at the phase boundary was even shown to enhance the SC upper critical field in the spin density wave compound $(TMTSF)_2PF_6$, that would also be expected in view of the above mentioned filamentary superconductors. This might explain why at 2.5 kbar the transition, although still very sharp, occurs at a lower T.

The biggest question at the moment is, why in the CDW state the superconductivity starts to appear at higher temperatures in comparison with that in the NM state. If the superconductivity is indeed spatially restricted to the CDW domain boundaries, one can understand, why the CDW does not completely suppress the SC state in contradiction to what has been theoretically proposed [149]. This will, however, not explain an enhanced SC onset temperature. In principle, in our model above one would still expect the opposite effect, namely that the SC filament has a reduced onset temperature due to the superconducting proximity effect. More investigations on this topic are highly desirable.

5.5.3 Conclusion

The first direct evidence for superconductivity in α-(BEDT-TTF)$_2$KHg(SCN)$_4$ under hydrostatic pressure is presented.

Superconductivity is found within the whole pressure range studied. Distinct differences in the superconducting properties are observed between the CDW and the NM state. The determined phase diagram therefore supports the above proposal of 2.5 kbar being the critical pressure P_0. Within the CDW state the superconducting transitions broaden and additionally show an unusually strong decrease of the resistance with cooling already in a higher temperature range. We associate this finding with small superconducting filaments or regions existing in the CDW state already at higher temperatures than expected from the NM state. This remarkable and unexpected observation remains at present one of the biggest questions. The broadening of the transitions as well as the finding of a pronounced positive curvature of the critical magnetic field we explain by proximity coupled filamentary superconductivity embedded in a CDW matrix. The idea of superconductivity emerging within CDW domain boundaries is suggested.

Chapter 6

Summary

The low-temperature density-wave state existing within the organic metal α-(BEDT-TTF)$_2$KHg(SCN)$_4$ below ≈ 8 K has been investigated by use of high static magnetic fields up to 28 T and hydrostatic pressures up to 4 kbar. At ambient pressure combined interlayer resistance and magnetic torque measurements have been performed, while under pressure solely the resistance was studied.

The results presented in this thesis give further strong evidence for the already proposed CDW nature of the low temperature state. Moreover, under certain experimental conditions new kinds of CDW subphases with different density wave vectors are most probably found to exist within different ranges of pressure and magnetic field.

The main part of this work has been devoted to the response of a CDW system to an applied magnetic field. Since the nesting instability arises from a very anisotropic Q1D electron band an additional, orbital effect of the magnetic field is expected besides the well-known Pauli paramagnetic one. While the former leads to an effective one-dimensionalization of the electron motion, and consequently to a stabilization of the density wave in magnetic field, the latter is known to suppress the CDW.

The starting point of the present investigations was the determination of the magnetic field-temperature (B-T) phase diagram at different pressures with the magnetic field directed perpendicular to the **a-c** planes.

Remarkably, the determined B-T phase diagrams at different pressures are found to be extremely well described by a recent theoretical model of Zanchi et al. on the CDW instability in Q1D electron systems at different nesting conditions. Hydro-

static pressure is thus found to cause a deterioration of the nesting conditions that eventually leads to a complete suppression of the CDW at $P_0 \approx 2.5$ kbar at zero magnetic field. One therefore has a perfect opportunity to determine and also tune the nesting conditions of the present system via the applied pressure.

An important observation is, that on worsening the nesting conditions with pressure the orbital effect becomes strongly enhanced and in a certain pressure and field range exceeds the Pauli effect. This is directly reflected in an increase of the CDW transition temperature with field.

At $P > P_0$ we have even proven that the CDW can only exist in a magnetic field due to the orbital effect. In this pressure region slow oscillations of the semiclassical (background) magnetoresistance are found on sweeping the magnetic field. Several arguments are given that these oscillations cannot be attributed to the SdH effect but rather to the first observation of field-induced transitions between CDW subphases with different nesting vectors. The latter effect can be considered as the CDW-analogue of the well known field-induced spin density wave (FISDW) transitions observed in other organic compounds. They are theoretically expected at $P > P_0$ and basically arise due to the fact that part of the carriers of the quasi-one dimensional electron system reappear as small pockets on the Fermi surface. Such a semi-metallic electron spectrum is caused by strongly imperfect nesting.

A clear structure observed in the hysteresis between the data taken on increasing and decreasing magnetic field is found to correlate with the slow background oscillations. At certain commensurate field directions it already appears at higher temperatures. To our opinion this gives the first solid argument for the existence of first order transitions. The latter are indeed theoretically expected to occur due to sudden jumps of the nesting vector between quantized values of the different CDW subphases.

At fields strongly inclined to the conducting planes we have studied in detail the already known anomalies in the magnetic torque as well as in the magnetoresistance occurring at ambient pressure. These anomalies turn out to be a second kind of field-induced CDW transitions. We propose a model, qualitatively well explaining the data observed. Contrary to the field-induced transitions under hydrostatic pressure, these new ones are now restricted to the modulated CDW_x state existing at magnetic fields above the paramagnetic limit of the low-field CDW_0 state. In the CDW_x state the x-component of the nesting vector steadily increases with field in order to completely gap one of the spin subbands. The carriers on the other sub-

band therefore become partially ungapped, a situation very similar to the strongly imperfect nesting observed at $P > P_0$. Thus, it is now the Pauli effect of magnetic field which causes a partial ungapping of the carriers on one of the spin-subbands. A simple model is derived including the steadily moving nesting vector and a quantization condition arising due to the ungapped carriers. The superposition of both effects then determines the observed multiple phase transitions. Within this model the experimental observations can be qualitatively understood very well.

Besides studying the magnet field effects on the CDW state we have given the first direct evidence for another, superconducting state under hydrostatic pressure. Surprisingly, the superconductivity was found not only to exist in the pressure range, where the CDW is already completely suppressed (at low magnetic fields), but also within the CDW state. While above the critical pressure of 2.5 kbar there are arguments for a bulk superconductivity, below 2.5 kbar there seems to be a coexistence of the CDW and the superconducting states, which are spatially separated. The superconductivity appears to become restricted to small superconducting regions or filaments embedded in the CDW matrix. This would explain the absence of the Meissner effect at ambient pressure, even when the interlayer resistance has already vanished, as well as a strong increase of the critical magnetic field on lowering the pressure below the critical value of 2.5 kbar. To the moment we suggest superconductivity to occur within CDW domain boundaries as has been proposed in another CDW compound. A remarkable finding in the region of the coexisting CDW and superconducting states is the dramatic increase of the superconducting onset temperature, in comparison to that in the NM state. The reason for this unexpected behaviour is at present not understood and needs further investigations.

Appendix

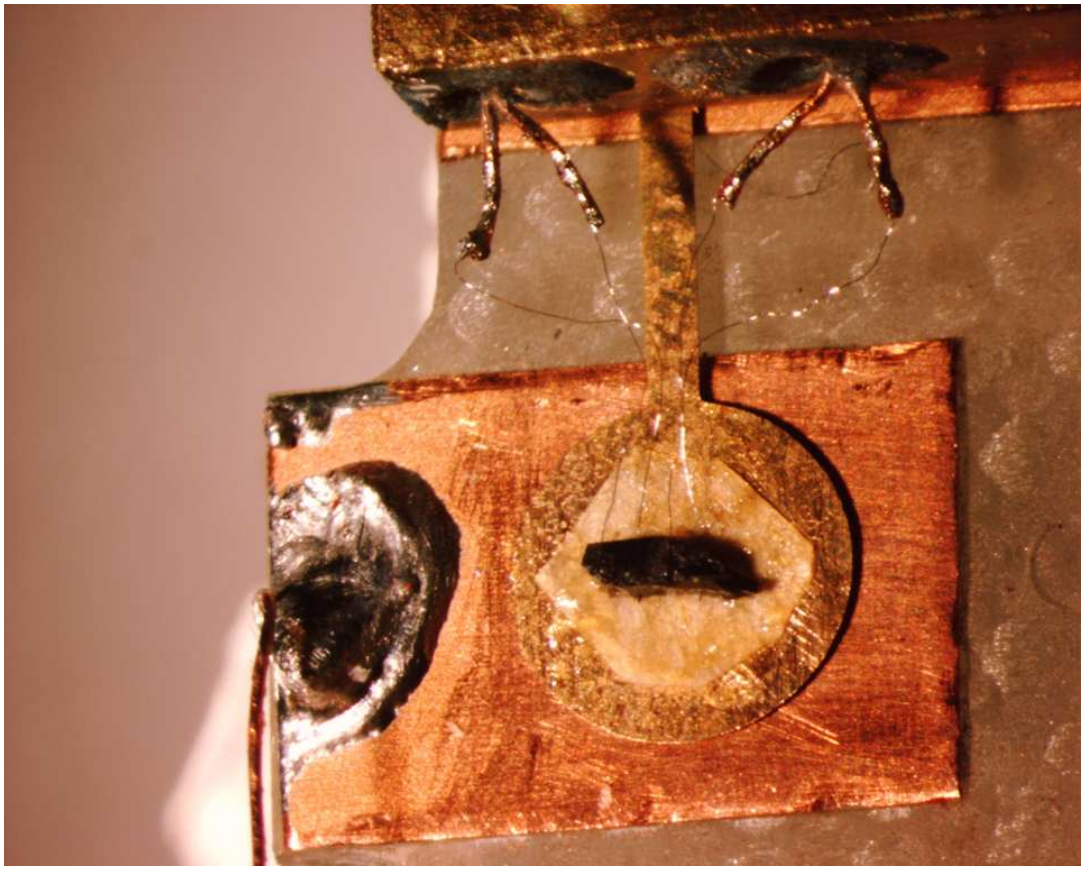

Figure 6.1: Capacitive torquemeter (old setup). The sample resistance is measured simultaneously with the torque.

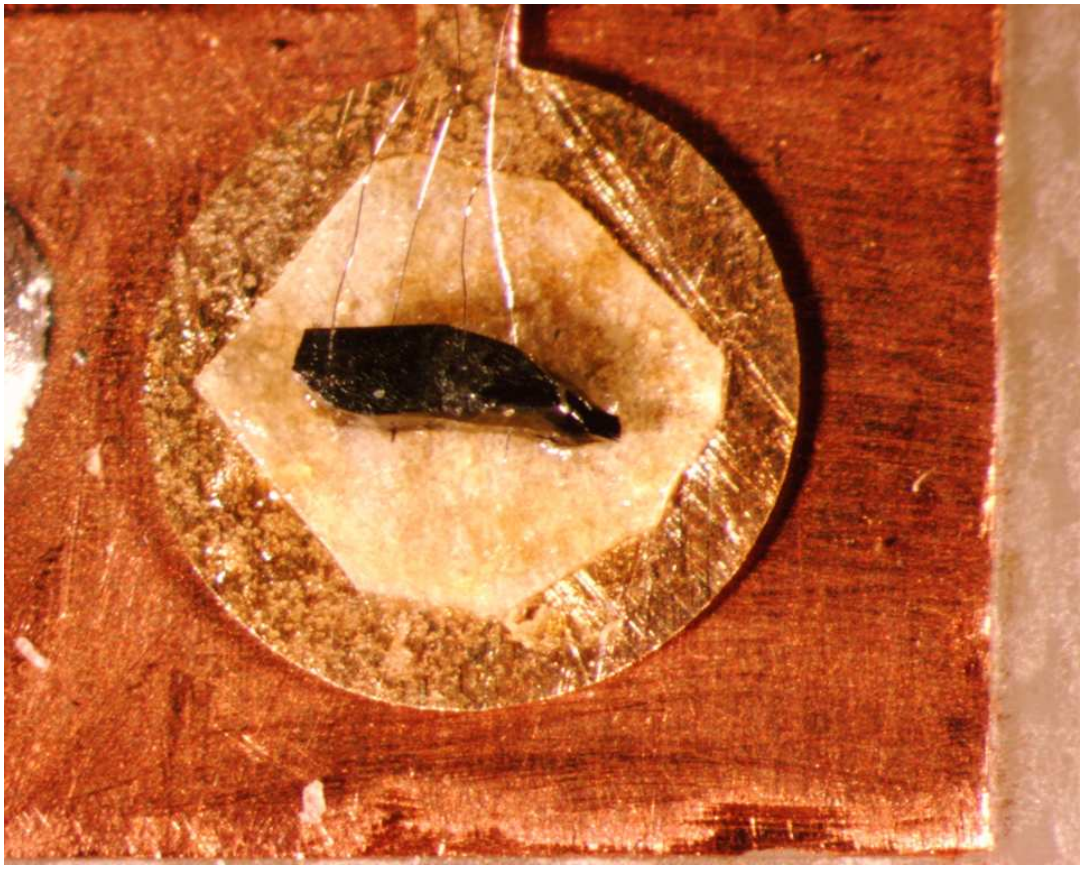

Figure 6.2: Enlarged part of the torquemeter.

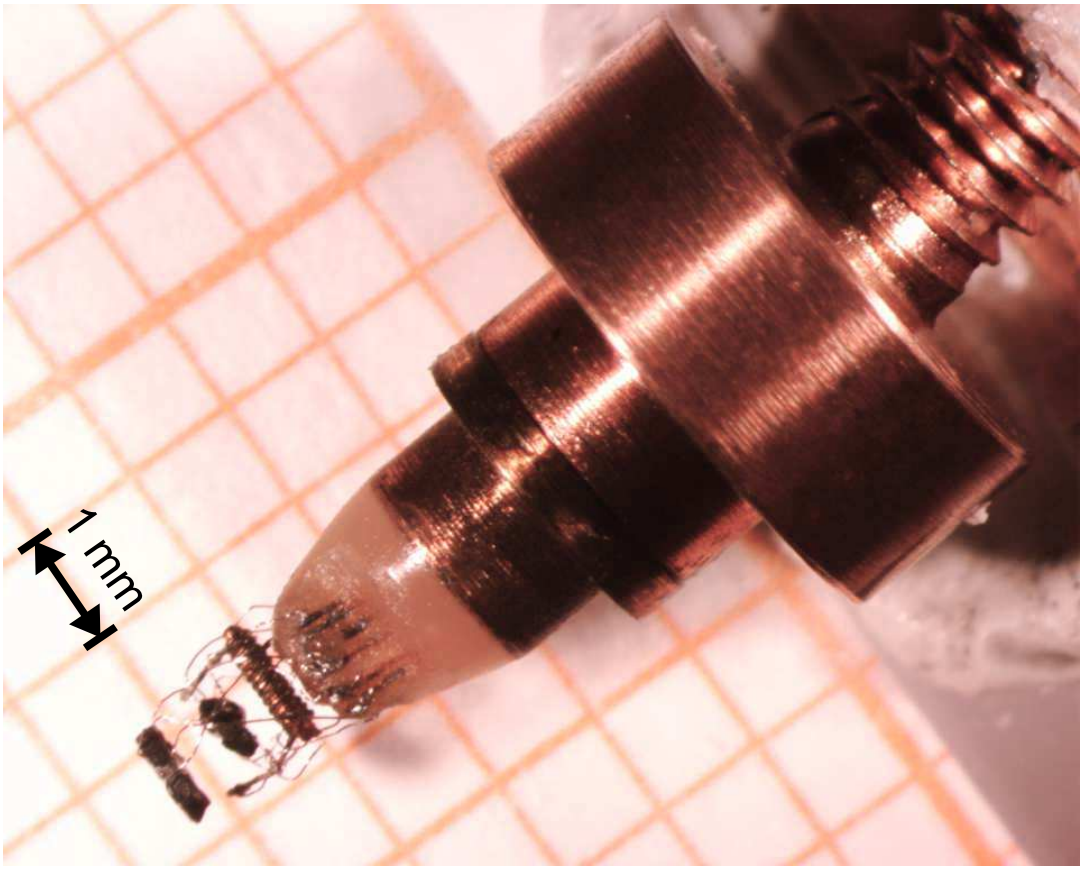

Figure 6.3: Feedthrough used in the small pressure cell.

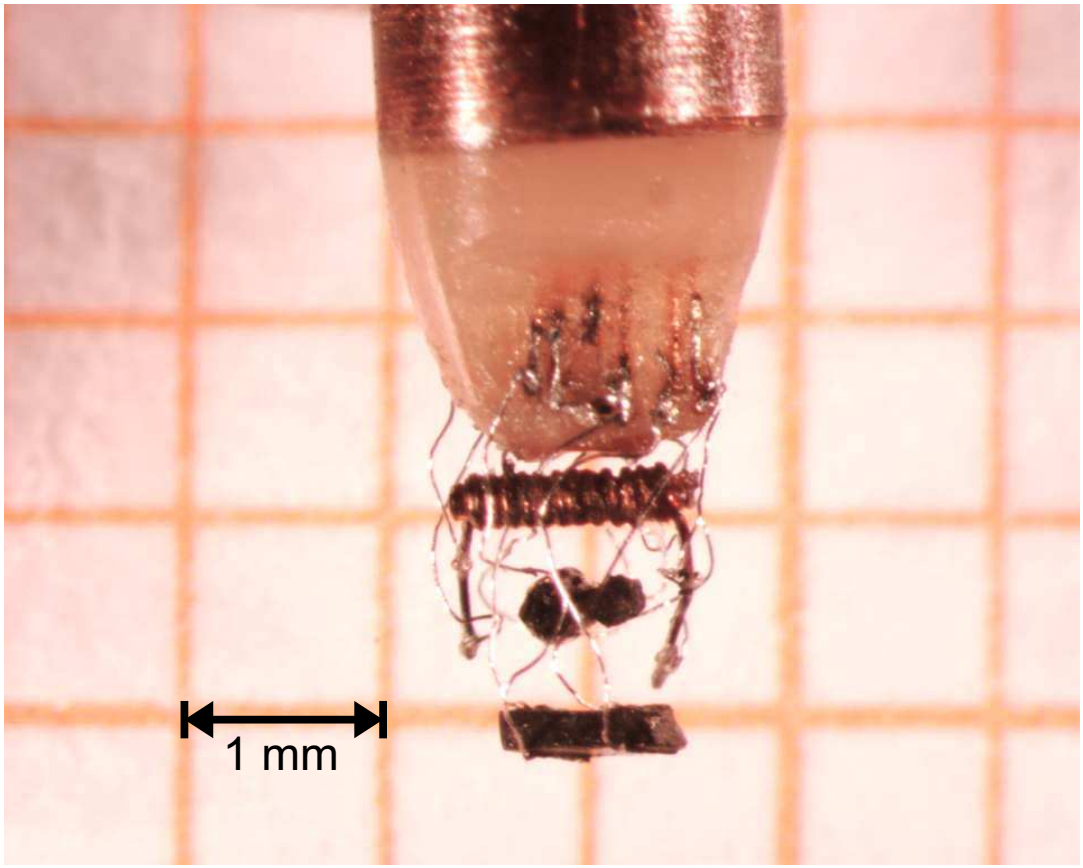

Figure 6.4: Top of the feedthrough. Two samples together with the manganin pressure sensor are mounted.

Figure 6.5: Inner (vacuum) part of the dilution refrigerator. The pressure cell is connected via silver rods to the mixing chamber.

Bibliography

[1] W. A. Little. *Phys. Rev.*, 134:A1416, 1964.

[2] T. Ishiguro, K. Yamaji, and G.Saito. *Organic Superconductors, 2^{nd} edition.* Springer-Verlag Berlin Heidelberg, 1998.

[3] D. Jérome. *Science*, 252:1509, 1991.

[4] D. Jérome. *Solid State Commun.*, 92:89, 1994.

[5] P. M. Chaikin. *J. Phys. I France*, 6:1875, 1996.

[6] S. Uji, H. Shinagawa, T. Terashima, T. Yakabe, Y. Terai, M. Tokumoto, A. Kobayashi, H. Tanaka, and H. Kobayashi. *Nature*, 410:908, 2001.

[7] S. Uji, T. Terashima, C. Terakura, T. Yakabe, Y. Terai, S. Yasuzuka, Y. Ymanaka, M. Tokumoto, A. Kobayashi, F. Sakai, H. Tanaka, H. Kobayashi, L. Balicas, and J. S. Brooks. *J. Phys. Soc. Jpn.*, 72:369, 2003.

[8] J. Wosnitza. *Studies of High-Temperature Superconductivity*, 34:97, 2000. edited by A. Narlikar (Nova Science Publishers, Huntington).

[9] J. Wosnitza. *Fermi Surfaces of Low-Dimensional Organic Metals and Superconductors.* Springer-Verlag Berlin Heidelberg, 1996.

[10] T. Osada, R. Yagi, A. Kawasumi, S. Kagoshima, N. Miura, M. Oshima, and G. Saito. *Phys. Rev. B*, 41:5428(R), 1990.

[11] M. V. Kartsovnik, A. E. Kovalev, and N. D. Kushch. *J. Phys. I France*, 3:1187, 1993.

[12] P. Christ, W. Biberacher, M. V. Kartsovnik, E. Steep, E. Balthes, H. Weiss, and H. Müller. *JETP Lett.*, 71:303, 2000.

[13] R. H. McKenzie. *cond-mat/9706235, unpublished*, 1997.

[14] D. Zanchi, A. Bjelis, and G. Montambaux. *Phys. Rev. B*, 53:1240, 1996.

[15] J. Brooks, K. Chen, S. Klepper, S. Valfells, G. Athas, Y. Tanaka, T. Kinoshita, M. Tokomoto, H. Anzai, and C. Agosta. *Phys. Rev. B*, 52:14457, 1995.

[16] N. Hanasaki, S. Kagoshima, N. Miura, and G. Saito. *J. Phys. Soc. Jap.*, 65:1010, 1996.

[17] J. Lindhard. *K. Dan. Vidensk. Selsk. Mat.-Fys. Medd.*, 28:8, 1954.

[18] J. M. Ziman. *Principles of the Theory of Solids*. Cambridge University Press, 1964.

[19] G. Grüner. *Density Waves in Solids*. Addison Wesley, 1994.

[20] S. Kagoshima, H. Nagasawa, and T. Sambongi. *Physics in One Dimension*. Springer Series in Solid-State Science 72, Springer Verlag Berlin Heidelberg New York Paris Tokyo, 1988.

[21] D. Jérome and H. J. Schulz. *Advances in Physics*, 31(4):299, 1982.

[22] L. P. Gorkov and A. G. Lebed. *J. Phys. (Paris) Lett.*, 45:L433, 1984.

[23] J. Solynom. *Adv. Phys.*, 28:201, 1979.

[24] T. M. Rice. *Physics in One Dimension*. eds. J. Bernasconi and T. Schneider, Springer-Verlag, 1981.

[25] S. Brown and G. Grüner. *Spektrum der Wissenschaft*, page 64, June 1994.

[26] W. Dieterich and P. Fulde. *Z. Physik*, 265:239, 1973.

[27] G. Sarma. *J. Phys. Chem. Solids*, 24:1029, 1963.

[28] A. I. Buzdin and V. V. Tugushev. *JETP*, 58:428, 1983.

[29] A. Bjelis, D. Zanchi, and G. Montambaux. *J. Phys. IV France*, 9:PR10–203, 1999.

[30] G. Montambaux. *Phys. Rev. B*, 38:4788, 1988.

[31] J. F. Kwak, J. E. Schirber, P. M. Chaikin, J. M. Williams, H.-H. Wang, and L. Y. Chiang. *Phys. Rev. Lett.*, 56:972, 1986.

[32] G. M. Danner, P. M. Chaikin, and S. T. Hannahs. *Phys. Rev. B*, 53:2727, 1996.

[33] W. Kang, S. T. Hannahs, and P. M. Chaikin. *Phys. Rev. Lett.*, 70:3091, 1993.

[34] V. M. Yakovenko. *Europhys. Lett.*, 3:1041, 1987.

[35] D. Schoenberg. *Magnetic oscillations in metals*. Cambridge University Press, 1984.

[36] L. Onsager. *Phil. Mag.*, 43:1006, 1952.

[37] W. J. de Haas and P. M. van Alphen. *Proc. Netherlands Roy. Acad. Sci.*, 33:1106, 1930.

[38] R. B. Dingle. *Proc. Roy. Soc.*, 211:517, 1952.

[39] L. W. Shubnikov and W. J. de Haas. *Proc. Netherlands Roy. Acad. Sci.*, 33:p.130 and 163, 1930.

[40] E. N. Adams and T. D. Holstein. *J. Phys. Chem. Solids*, 10:254, 1959.

[41] A. A. Abrikosov. *Fundamentals of the Theory of Metals*. Elsevier Sciense Publishers B.V., 1988.

[42] N. Harisson, R. Bogaerts, P. H. P. Reinders, J. Singleton, S. J. Blundell, and F. Herlach. *Phys. Rev. B*, 54:9977, 1996.

[43] M. A. Itskovsky and T. Maniv. *Phys. Rev. B*, 64:174421, 2001.

[44] M. V. Kartsovnik. *Chem. Rev.*, 104:5737, 2004.

[45] E. I. Blount. *Phys. Rev. Lett.*, 126:1636, 1962.

[46] T. Osada, S. Kagoshima, and N. Miura. *Phys. Rev. B*, 46:1812, 1992.

[47] M. J. Naughton, O. H. Chung, L. Y. Chiang, and J. S. Brooks. *Mater. Res. Soc. Symp. Proc.*, 173:257, 1990.

[48] T. Osada, A. Kawasumi, S. Kagoshima, N. Miura, and G. Saito. *Phys. Rev. Lett.*, 66:1525, 1991.

[49] T. Osada, A. Kawasumi, S. Kagoshima, N. Miura, and G. Saito. *Physica C*, 185-189:2697, 1991.

[50] M. J. Naughton, O. H. Chung, M. Chaparala, X. Bu, and P. Coppens. *Phys. Rev. Lett.*, 67:3712, 1991.

[51] K. Yamaji. *J. Phys. Soc. Jpn.*, 58:1520, 1989.

[52] R. Yagi, Y. Iye, T. Osada, and S. Kagoshima. *J. Phys. Soc. Jpn.*, 59:3069, 1990.

[53] V.G. Peschansky, J.A. Lopes, and T.G. Yao. *J. Phys. I France*, 1:1469, 1991.

[54] M. V. Kartsovnik, V. N. Laukhin, S. I. Pesotskii, I. F. Schegolev, and V. M. Yakovenko. *J. Phys. I France*, 2:89, 1992.

[55] Y. Kurihara. *J. Phys. Soc. Jpn.*, 61:975, 1992.

[56] A. B. Pippard. *Magnetoresistance in Metals.* Cambridge University Press, 1989.

[57] R. Rousseau, M.-L. Doublet, E. Canadell, R. P. Shibaeva, S. S. Khasanov, L. P. Rozenberg, N. D. Kushch, and E. B. Yagubskii. *J. Phys. I France*, 6:1527, 1996.

[58] P. C. W. Leung, T. J. Emge, M. A. Beno, H. H. Wang, J. M. Williams, V. Petricek, and P. Coppens. *J. Am. Chem. Soc.*, 107:6184, 1985.

[59] H. Mori, S. Tanaka, M. Oshima, G. Saito, T. Mori, Y. Murayama, and H. Iinokuchi. *Bull. Chem. Soc. Jpn.*, 63:2183, 1991.

[60] H. Sato, H. Taniguchi, Y. Nakazawa, A. Kawamoto, K. Kato, and K. Kanoda. *Synth. Met.*, 70:915, 1995.

[61] J. Singleton. *Rep. Prog. Phys.*, 63:1111, 2000.

[62] H. H. Wang, K. D. Carson, U. Geiser, W. K. Kwok, M. D. Vashon, J. E. Thompson, N. F. Larsen, G. D. Mccabe, R. S. Hulscher, and J. M. Williams. *Physica C*, 166:57, 1990.

[63] H. Taniguchi, H. Sato, Y. Nakazawa, and K. Kanoda. *Phys. Rev. B*, 53:8879(R), 1996.

[64] A. E. Kovalev, M. V. Kartsovnik, R. P. Shibaeva, L. P. Rozenberg, and I. F. Schegolev. *Solid State Commun.*, 89:575, 1994.

[65] J. S. Boebinger, G. Montambaux, M. L. Kaplan, R. C. Haddon, S. V. Chichester, and L. Y. Chiang. *Phys. Rev. Lett.*, 64:591, 1990.

[66] M. V. Kartsovnik and V. N. Laukhin. *J. Phys. I France*, 6:1753, 1996.

[67] Y. Iye, R. Yagi, N. Hanasaki, S. Kagoshima, H. Mori, H. Fujimoto, and G. Saito. *J. Phys. Soc. Jpn.*, 63:674, 1994.

[68] T. Sasaki and N. Toyota. *Phys. Rev. B*, 49:10120, 1994.

[69] T. Sasaki, H. Sato, and N. Toyota. *Synth. Met.*, 41-43:2211, 1991.

[70] F. L. Pratt, T. Sasaki, and N. Toyota. *Phys. Rev. Lett.*, 74:3892, 1995.

[71] R. Tsuchiya, T. Nakamura, T. Takahashi, T. Sasaki, and N. Toyota. *Synth. Met.*, 70:965, 1995.

[72] T. Miyagawa, A. Kawamoto, and K. Kanoda. *Phys. Rev. B.*, 56:8487(R), 1997.

[73] P. Christ, W. Biberacher, H. Müller, K. Andres, E. Steep, and A. G. M. Jansen. *Synth. Metals*, 70:823, 1996.

[74] P. Christ. *Dissertation an der Fakultät für Physik an der Technischen Univrsität München.* 1998.

[75] A. Kovalev and H. Müller. *Synth.Metals*, 86, 1997.

[76] T. Sasaki, A. Lebed, and T. Fukase. *Phys. Rev. B*, 54:12969, 1996.

[77] M. V. Kartsovnik, W. Biberacher, E. Steep, P. Christ, K. Andres, A. G. M. Jansen, and H. Müller. *Synth. Metals*, 86:1933, 1997.

[78] N. Harrison, L. Balicas, J. S. Brooks, and M. Tokumoto. *Phys. Rev. B*, 62:14212, 2000.

[79] J. S. Qualls, L. Balicas, J. S. Brooks, N. Harrison, L. K. Montgomery, and M. Tokumoto. *Phys. Rev. B*, 62:10008, 2000.

[80] P. Fulde and R. A. Ferrell. *Phys. Rev.*, 135:A550, 1964.

[81] A. I. Larkin and Y. N. Ovchinikov. *Sov. Phys. JETP*, 20:762, 1965.

[82] M. Basletić, B. Korin-Hamzić, M. V. Kartsovnik, and H. Müller. *Synth. Met.*, 120:1021, 2001.

[83] P. Foury-Leylekian, S. Ravy, J. P. Pouget, and Müller. *Synth. Met.*, 137:1271, 2003.

[84] A. House, S. Blundell, M. M. Honold, J. Singleton, J. A. A. J. Perenboom, W. Hayes, M. Kurmoo, and P. Day. *J. Phys. Cond. Mat.*, 8:8829, 1996.

[85] R. H. McKenzie, G. J. Athas, J. S. Brooks, R. G. Clark, A. S. Dzurak, R. Newbury, R. P. Starrett, A. Skougarevsky, M. Tokumoto, N. Kinoshita, T. Kinoshita, and Y. Tanaka. *Phys. Rev. B*, 54:8289(R), 1996.

[86] L. I. Buravov, N. D. Kushch, V. N. Laukhin, A. G. Khomenko, E. B. Yagubskii, M. V. Kartsovnik, A. E. Kovalev, L. P. Rozenberg, R. P. Shibaeva, M. A. Tanatar, V. S. Yefanof, V. V. Dyakin, and V. A. Bondarenko. *J. Phys. I France*, 4:441, 1994.

[87] P. Christ, W. Biberacher, H. Müller, and K. Andres. *Solid State Commun.*, 91:451, 1994.

[88] I. L. Spain and S. Segall. *Cryogenics*, 11:26, 1971.

[89] L. C. Towle. *Appl. Phys. Lett.*, 10:317, 1967.

[90] S. Yamamoto. *Bull. of the N.R.L.M.*, 24:25, 1972.

[91] H. Fujiwara, H. Kadomatsu, K. Thoma, and Rev. Sci. Instrum. *Rev. Sci. Instrum.*, 51:1345, 1980.

[92] D. Andres. Diploma thesis, TU München, 2000.

[93] M. V. Kartsovnik, D. Andres, W. Biberacher, P. Christ, E. Steep, E. Balthes, H. Weiss, H. Müller, and N. D. Kushch. *Synth. Metals*, 120:687, 2001.

[94] A. Schegolev, V. Laukhin, A. Khomenko, M. Kartsovnik, R. Shibaeva, L. Rozenberg, and A. Kovalev. *J. Phys. I France*, 2:2123, 1992.

[95] Y. Hasegawa and H. Fukuyama. *J. Phys. Soc. Jpn.*, 55:3978, 1986.

[96] K. Yamaji. *J. Phys. Soc. Jpn.*, 51:2787, 1982.

[97] N. Biskup, S. Tomic, and D. Jerome. *Phys. Rev. B*, 51:17972, 1995.

[98] N. Biskup, J. A. A. J. Perenboom, J. S. Qualls, and J. S. Brooks. *Solid State Commun.*, 107:503, 1998.

[99] B. Hamzic, G. Creuzet, and C. Lenoir. *J. Phys. F: Met.Phys.*, 17:2267, 1987.

[100] L. Forró, K. Biljaković, J. R. Cooper, and K. Bechgaard. *Phys. Rev. B*, 29:2839, 1984.

[101] R. H. McKenzie, J. S. Qualls, S. Y. Han, and J. S. Brooks. *Phys. Rev. B*, 57:11854, 1998.

[102] R. V. Coleman, M. P. Everson, Hao-An Lu, , A. Johnson, and L. M. Falicov. *Phys. Rev. B*, 41:460, 1990.

[103] D. Andres, M. V. Kartsovnik, W. Biberacher, H. Weiss, E. Balthes, H. Müller, and N. Kushch. *Phys. Rev. B*, 64:161104(R), 2001.

[104] R. W. Stark and C. B. Friedberg. *Phys. Rev. Lett.*, 26:556, 1971.

[105] S. Uji, H. Aoki, J. S. Brooks, A. S. Perel, G. J. Athas, S. J. Klepper, C. C. Agosta, D. A. Howe, M. Tokumoto, N. Kinoshita, Y. Tanaka, and H. Anzai. *Solid State Commun.*, 88:683, 1993.

[106] A. House, C. J. Hawoth, J. M. Caulfield, S. Blundell, M. M. Honold, J. Singleton, W. Hayes, S. M. Hayden, P. Meeson, M. Springford, M. Kurmoo, and P. Day. *J. Phys. Cond. Mat.*, 8:10361, 1996.

[107] N. Harrison, N. Biskup, J. S. Brooks, L. Balicas, and M. Tokumoto. *Phys. Rev. B*, 63:195102, 2001.

[108] G. J. Athas, J. S. Brooks, S. Valfells, S. J. Klepper, M. Tokumoto, N. Kinoshita, T. Kinoshita, and Y. Tanaka. *Phys. Rev. B*, 34:863, 1994.

[109] N. Harrison. *Phys. Rev. Lett.*, 83:1395, 1999.

[110] P. Monceau. *Solid State Commun.*, 24:331, 1977.

[111] C. E. Campos, P. S. Sandhu, J. S. Brooks, and T. Ziman. *Phys. Rev. B*, 53:12725, 1996.

[112] M. M. Honold, N. Harrison, J. Singleton, M.-S. Nam, S. J. Blundell, C. H. Mielke, M.V. Kartsovnik, and N.D. Kushch. *Phys. Rev. B*, 59:10417(R), 1999.

[113] T. Sasaki and N. Toyota. *Phys. Rev. B*, 48:11457(R), 1993.

[114] E. M. Lifshitz and A. M. Kosevich. *J. Phys. Chem. Solids*, 4:1, 1956.

[115] N. Harrison, C. H. Mielke, J. Singleton, J. S. Brooks, and M. Tokumoto. *J. Phys.: Condens. Matter*, 13:L389–L395, 2001.

[116] S. Hill, P.S. Sandhu, J.S. Qualls, J.S. Brooks, M. Tokumoto, N. Kinoshita, T. Kinoshita, and Y. Tanaka. *Phys. Rev. B*, 55:4891(R), 1997.

[117] M. M. Honold, N. Harrison, J. Singleton, H. Yaguchi, C. H. Mielke, D. Rickel, I. Deckers, P. H. P. Reinders, F. Herlach, M. Kurmoo, and P. Day. *J. Phys.: Condens. Matter*, 9:L533, 1997.

[118] N. Harrison. *Phys. Rev. R*, 66:121101(R), 2002.

[119] N. Harrison, J. Singleton, A. Bangura, A. Ardavan, P. A. Goddard, R. D. McDonald, and L. K. Montgomery. *Phys. Rev. B*, 69:165103, 2004.

[120] S. Uji, J.S. Brooks, M. Chaparala, L. Seger, T. Szabo, M. Tokumoto, N. Kinoshita, T. Kinoshita, Y. Tanaka, and H. Anzai. *Solid State Commun.*, 100:825, 1996.

[121] N. Harrison, A. House, I.Deckers, J. Caulfield, J. Singleton, F. Herlach, W. Hayes, M. Kurmoo, and P. Day. *Phys. Rev. B*, 52:5584, 1996.

[122] A. House, W. Lubczynski, S. Blundell, J. Singleton, W. Hayes, M. Kurmoo, and P. Day. *J. Phys. Cond. Mat.*, 8:10377, 1996.

[123] T. Sasaki and T. Fukase. *Phys. Rev. B*, 59:13872, 1999.

[124] S. Kawamata, K. Okuda, I. Kakeyab, K. Kindo, T. Sasaki, and N. Toyotad. *Synth. Metals*, 86:2015, 1997.

[125] K. Yamaji. *J. Phys. Soc. Jpn.*, 53:2189, 1984.

[126] G. Montambaux, M. Heritier, and P. Lederer. *Phys. Rev. Lett.*, 55:2078, 1985.

[127] A. G. Lebed. *Pis'ma Zh. Eksp. Teor. Fiz.*, 43:137, 1986.

[128] K. Yamaji. *J. Phys. Soc. Jpn.*, 56:1841, 1987.

[129] A. G. Lebed. *Pis'ma Zh. Eksp. Teor. Fiz.*, 78:170, 2003.

[130] K. Yamaji. *Synth. Met.*, 13:29, 1986.

[131] A. G. Lebed. *Pis'ma Zh. Eksp. Teor. Fiz.*, 72:205, 2000.

[132] A. G. Lebed. *Phys. Rev. Lett.*, 88:177001, 2002.

[133] K. Sengupta and N. Dupuis. *cond-mat/0302142, unpublished*, 2003.

[134] A. V. Kornilov, V. M. Pudalov, Y. Kitaoka, K. Ishida, T. Mito, J. S. Brooks, J. S. Qualls, J. A. A. J. Perenboom, N. Tateiwa, and T. C. Kobayashi. *Phys. Rev. B*, 65:060404(R), 2002.

[135] W. Kang. *Thesis, Princeton University.* 1993.

[136] A. E. Kovalev, S. Hill, and J. S. Qualls. *Phys. Rev. B*, 66:134513, 2002.

[137] C. Proust, A. Audouard, A. Kovalev, D. Vignolles, M. Kartsovnik, L. Brossard, and N. Kushch. *Phys. Rev. B*, 62:2388, 2000.

[138] E. S. Choi, J. S. Brooks, and J. S. Qualls. *Phys. Rev. B*, 65:205119, 2002.

[139] D. Zanchi and G. Montambaux. *Phys. Rev. Lett.*, 77:366, 1996.

[140] M. Gusmão and T. Ziman. *Phys. Rev. B*, 54:16663, 1996.

[141] D. Andres, M. Kartsovnik, P. D. Grigoriev, W. Biberacher, and H. Müller. *Phys. Rev. B*, 68:201101(R), 2003.

[142] R. Kondo, S. Kagoshima, and M. Maesato. *Phys. Rev. B*, 67:134519, 2003.

[143] M. Maesato, Y. Kaga, R. Kondo, and S. Kagoshima. *Phys. Rev. B.*, 64:155104, 2001.

[144] H. Ito, M. V. Kartsovnik, H. Ishimoto, K. Kono, H. Mori, N. D. Kushch, G. Saito, T. Ishiguro, and S. Tanaka. *Synth. Met.*, 70:899, 1995.

[145] D. Andres, M. V. Kartsovnik, W. Biberacher, K. Neumaier, and H. Müller. *J. Phys. IV France*, 12:PR9–87, 2002.

[146] V. J. Emery and S. A. Kivelson. *Nature*, 374:434, 1995.

[147] M. Tinkham. *Introduction to Superconductivity.* McGraw-Hill International editions, 1996.

[148] M. Fisher. *Phys. Rev. Lett.*, 65:923, 1990.

[149] A. M. Gabovich, A. I. Voitenko, and M. Ausloos. *Phys. Rep.*, 367:583, 2002.

[150] D. J. Resnick, J. C. Garland, J. T. Boyd, S. Shoemaker, and R. S. Newrock. *Phys. Rev. Lett.*, 47:1542, 1981.

[151] D. W. Abraham, C. J. Lobb, M. Tinkham, and T. M. Klapwijk. *Phys. Rev. B*, 26:5268, 1982.

[152] L. J. Azevedo, W. G. Clark, G. Deutscher, R. L. Greene, G. B. Street, and L. J. Suter. *Solid State Commun.*, 19:197, 1976.

[153] A. Briggs, P. Monceau, M. Nunez-Regueiro, M. Ribault, and J. Richard. *J. Phys.*, 42:1453, 1981.

Publication List

D. Andres, M. V. Kartsovnik, W. Biberacher, H. Weiss, E. Balthes, H. Müller, and N. Kushch.
Phys. Rev. B, **64**:161104(R), 2001.

D. Andres, M. Kartsovnik, P. D. Grigoriev, W. Biberacher, and H. Müller.
Phys. Rev. B, **68**:201101(R), 2003.

D. Andres, M. V. Kartsovnik, W. Biberacher, K. Neumaier, and H. Müller.
J. Phys. IV France, **12**:PR9–87, 2002.

D. Andres, M. V. Kartsovnik, W. Biberacher, T. Togonidze, H. Weiss, E. Balthes, and N. Kushch.
Synth. Met., **120**:841, 2001.

M. V. Kartsovnik, D. Andres, W. Biberacher, P. Christ, E. Steep, E. Balthes, H. Weiss, H. Müller, and N. D. Kushch.
Synth. Met., **120**:687, 2001.

M. V. Kartsovnik, D. Andres, W. Biberacher, P. D. Grigoriev, E. A. Schuberth, and H. Müller.
J. Phys. IV France, **114**:191, 2004.

M. V. Kartsovnik, D. Andres, P. D. Grigoriev, W. Biberacher, and H. Müller.
Physica B: Condensed Matter, **346-347**:368, 2004.

A.E. Kovalev, M.V. Kartsovnik, D. Andres, A.G.M. Jansen, and N.D. Kushch.
Synth. Met., **133-134**:131, 2003.

P. Christ, W. Biberacher, D. Andres, M. V. Kartsovnik, E. Balthes, H. Weiss, and H. Müller.
Synth. Met., **12**0:1019, 2001.

W. Biberacher, P. Christ, M. V. Kartsovnik, D. Andres, and H. Müller.
J. Phys. IV France, **114**:291, 2004.

Acknowledgements

Of course, this work could not have been done without the help of many people to whom I would like to express my gratitude. In particular, I would like to thank...

- our organic metal team,
  - Mark Kartsovnik, my academic advisor, for teaching me all the experimental and physical know-how, without exception taking his time for answering and discussing my questions and always motivating me for new interesting tasks.
  - Werner Biberacher, for all his contribution to this work, and especially for his expertize in the magnetic torque experiments.
- Prof. Rudolf Gross, for accepting me as a PhD student.
- Pavel Grigoriev, a young theorist, always full of energy, for his theoretical ideas and for the fruitful discussions.
- Karl Neumaier, for the experimental support on the dilution refrigerator and for teaching me some experimental low temperature physics.
- Harald Müller and Natasha Kushch, for the synthesis of many high quality samples.
- the WMI workshop, in particular Helmut Thies, for doing an outstanding job on fabricating the new designed 2-axes rotator.
- the staff at the high field lab in Grenoble, for their experimental support.
- Joachim Geismann, for the technical expert advice on the Helium-pressure station.
- Sergei Pesotskii, for his experimental contribution.
- Erwin Schuberth, for the joint SQUID measurement in the "milli-mill".
- Wolfgang Schmitt, for the photographic equipment.
- all the people at the WMI, for their readiness to help and for creating a nice working atmosphere.
- my family